UNIVERSIDADE ESTADUAL DE CAMPINAS

Faculdade de Engenharia Química

DIOGO SILVA SANCHES JORQUEIRA

DEVELOPMENT OF NIOBIUM OXIDE BASED CATALYSTS: DIRECT CONVERSION OF XYLOSE TO FURFURYL ALCOHOL

DESENVOLVIMENTO DE CATALISADORES A BASE DE ÓXIDO DE NIÓBIO: CONVERSÃO DIRETA DE XILOSE A ÁLCOOL FURFURÍLICO

CAMPINAS

2022

DIOGO SILVA SANCHES JORQUEIRA

DEVELOPMENT OF NIOBIUM OXIDE BASED CATALYSTS: DIRECT CONVERSION OF XYLOSE TO FURFURYL ALCOHOL

DESENVOLVIMENTO DE CATALISADORES A BASE DE ÓXIDO DE NIÓBIO: CONVERSÃO DIRETA DE XILOSE A ÁLCOOL FURFURÍLICO

Tese apresentada à Faculdade de Engenharia Química da Universidade Estadual de Campinas como parte dos requisitos para a obtenção do título de Doutor em Engenharia Química.

Thesis submitted in partial fulfillment of the requirements for the award of the degree of Doctor in Chemical Engineering of the University of Campinas.

Advisor: Prof. Dr. Raphael Soeiro Suppino

Co-Advisor: Dr. Léa Vilcocq

ESTE TRABALHO CORRESPONDE À VERSÃO FINAL DA TESE DEFENDIDA PELO ALUNO DIOGO SILVA SANCHES JORQUEIRA, ORIENTADO PELO PROF. DR. RAPHAEL SOEIRO SUPPINO.

CAMPINAS

2022

Ficha catalográfica
Universidade Estadual de Campinas
Biblioteca da Área de Engenharia e Arquitetura
Rose Meire da Silva - CRB 8/5974

J769d

Jorqueira, Diogo Silva Sanches, 1992-
Development of niobium oxide based catalysts: direct conversion of xylose to furfuryl alcohol / Diogo Silva Sanches Jorqueira. – Campinas, SP : [s.n.], 2022.

Orientador: Raphael Soeiro Suppino.
Coorientador: Léa Vilcocq.
Tese (doutorado) – Universidade Estadual de Campinas, Faculdade de Engenharia Química.

1. Xilose. 2. Hidrogenação. 3. Óxido de nióbio. 4. Furfural. 5. Catalisadores. I. Suppino, Raphael Soeiro, 1984-. II. Vilcocq, Léa. III. Universidade Estadual de Campinas. Faculdade de Engenharia Química. IV. Título.

Informações para Biblioteca Digital

Título em outro idioma: Desenvolvimento de catalisadores a base de óxido de nióbio: conversão direta de xilose a álcool furfurílico
Palavras-chave em inglês:
Xylose
Hydrogenation
Niobium oxide
Furfural
Catalysts
Área de concentração: Engenharia Química
Titulação: Doutor em Engenharia Química
Banca examinadora:
Raphael Soeiro Suppino [Orientador]
Gustavo Doubek
Cristiane Barbieri Rodella
Angela Sanches Rocha
Franck Rataboul
Data de defesa: 13-06-2022
Programa de Pós-Graduação: Engenharia Química

Identificação e informações acadêmicas do(a) aluno(a)
- ORCID do autor: https://orcid.org/0000-0001-5724-3095
- Currículo Lattes do autor: http://lattes.cnpq.br/3428795779800472

Folha de Aprovação da Defesa de Tese de Doutorado defendida por **DIOGO SILVA SANCHES JORQUEIRA** e aprovada em 13 de junho de 2022 pela Comissão Examinadora constituída pelos doutores:

Prof. Dr. Raphael Soeiro Suppino - Presidente e Orientador
FEQ/UNICAMP

Prof. Dr. Gustavo Doubek
FEQ/UNICAMP

Dra. Cristiane Barbieri Rodella
Centro Nacional de Pesquisa em Energia e Materiais

Profa. Dra. Angela Sanches Rocha
Universidade do Estado do Rio de Janeiro
(Videoconferência)

Dr. Franck Rataboul
Université Lyon
(Videoconferência)

ATA da defesa com as respectivas assinaturas dos membros encontra-se no SIGA/Sistema de Fluxo de Dissertação / Tese e na Secretaria do Programa da Unidade.

Abstract

One of the most promising molecules in biomass valorization is the xylose (XYL), a five carbon sugar, that once dehydrated in acid media, can produce furfural (FUR). In turn, FUR is an aldehyde that may produce furfuryl alcohol (FA) by hydrogenation. It is known that the presence of Lewis and Brønsted acid sites may transform XYL to FUR, and the presence of a metal phase can reduce FUR to FA. Among many researched materials, the hydrated niobium oxide ($Nb_2O_5 \cdot nH_2O$) may provide both sites, due to its acidity. Besides, it is possible to modify Nb_2O_5 structure with an acid treatment to provide new groups. Then, it is feasible to produce a catalyst supported on different niobium oxides to try the one-pot production of FA from XYL and to test the influence of the acid treatment. On this work, Co, Ni and Ru were supported using incipient wetness impregnation on two types of niobium oxides calcined at 400 °C for 4 h: calcined Nb_2O_5 - NB400 or Nb_2O_5 treated with H_3PO_4 at 1 mol/L - NBAc400. For the base metals, the nominal amount was 10 wt.% (CoNB10, CoNBAc10, NiNB10 and NiNBAc10) whereas for the noble metal the content was 5 wt.% (RuNB05 and RuNBAc05). Our solids were characterized by N_2 adsorption, SEM/EDX, XRD, H_2-TPR, XPS and NH_3-TPD. The catalysts supported on NB400 showed diminution of its area, up to 60% in case of RuNB05. After the activation on hydrogen at 400 °C and 2 h, the TPR and XPS showed that the Co active phase was a majority of oxides, Ni samples were a mixture of oxides and reduced metal and the Ru solid was reduced. Furthermore, the acidity distribution of the sites was modified due to the acid treatment, with the increase of medium sites. After 6 h of reaction on water at 160°C and 50 bar of H_2 pressure, the CoNB10 solid presented 14% of FA yield, while the treated catalyst CoNBAc10 had 8%. The same trend was reported on Ni and Ru solids - 16% and 17% of FA yield on NiNB10 and RuNB05, whereas 2% and 0% on NiNBAc10 and RuNBAc05. However, Ni and Ru solid showed superior yields for xylitol (XOL) and tehtrahydrofurfuryl alcohol (THFA). The RuNB05 solid had 39% and 20% of XOL and THFA yields, as the content of metal sites was higher than Ni and Co solids. Besides, after one cycle of reaction, the treated catalysts showed P and metal leaching up to 30%. Therefore, the acid treatment did not improve neither the selectivity for hydrogenation products nor the stability of metal phases on the catalysts.

Keywords: Xylose, Furfuryl Alcohol, Niobium Oxide, Supported Catalysts.

Resumo

Uma das moléculas mais promissoras em valorização de biomassa é a xilose (XYL), que desidratada em meio ácido, produz furfural (FUR). Já o FUR é um aldeído que hidrogenado produz o álcool furfurílico (FA). Sabe-se que a presença de sítios ácidos de Lewis e de Brønsted converte XYL em FUR, e a presença de sítios metálicos consegue reduzir FUR ao FA. Dentre os materiais pesquisados, a nióbia ($Nb_2O_5 \cdot nH_2O$) pode suprir ambos os sítios ácidos. Além disto, é possível modificá-la com um tratamento ácido, produzindo assim novos grupos. Portanto, é possível produzir um catalisador suportado em diferentes óxidos de nióbio para tentar produzir o FA através da XYL em um único reator, e também testar a influência do tratamento ácido. Neste trabalho, Co, Ni e Ru foram suportados por impregnação incipiente em dois tipos de óxidos de nióbio calcinados e 400 °C durente 4 h: nióbia calcinada - (NB400) ou Nb_2O_5 tratado com H_3PO_4 em 1 mol/L - NBAc400. Para os metais básicos, o teor nominal de fase ativa foi 10% (CoNB10, CoNBAc10, NiNB10 e NiNBAc10) enquanto que para o metal nobre o valor foi 5% (RuNB05 e RuNBAc05). Nossos sólidos foram caracterizados por adsorção de N_2, MEV/EDS, DRX, H_2-TPR, XPS e NH_3-TPD. Os catalisadores suportados em NB400 apresentaram diminuição de área, em até 65%, no caso do RuNB05. Após ativação em fluxo de H_2 a 400 °C por 2 h, as análises de TPR e XPS mostraram que a fase ativa de Co era maioria de óxidos, as amostras de Ni eram misturas de óxido com metal reduzido e o sólido de Ru estava reduzido. Ademais, a distribuição de acidez nos sítios foi modificada com o tratamento ácido, com o aumento de sítios médios. Após 6 h de reação em meio aquoso a 160 °C e 50 bar de H_2, o sólido CoNB10 teve 14% de rendimento ao FA, em comparação com 8% no CoNBAc10. A mesma tendência aconteceu com Ni e Ru - 16% e 17% de rendimento ao FA no NiNB10 e RuNB05, ao passo que em NiNBAc10 e RuNBAc05 os valores foram 2% e 0%. No entanto, Ni e Ru mostraram rendimentos superiores para xilitol (XOL) e álcool tetrahidrofurfurílico (THFA). O catalisador RuNB05 obteve 39% e 20% de rendimentos a XOL e THFA, uma vez que a participação de sítios metálicos foi maior do que Ni e Co. Adicionalmente, após um ciclo de reação, os catalisadores tratados mostraram lixiviação de fósforo e fase metálica com teores de até 50%. Logo, o tratamento ácido efetuado não melhorou a seletividade a produtos de hidrogenação nem a estabilidade dos metais.

Palavras-chave: Xilose, Álcool Furfurílico, Óxido de Nióbio, Catalisadores Suportados.

Acknowledgements

First, I would like to thank God for the gift of my life and for the accomplishment of this work. Besides, I really appreciate the help of other persons from the beginning as a undergraduate student, at 2011, to the conclusion of my Doctorate degree, at 2022.

- To my mom and my dad, and especially for their love for supporting me on the most difficult moments.
- To my advisor, Prof. Dr. Raphael Suppino and my co-advisor Dr. Léa Vilcocq, for the insights and our discussion of results.
- To Dr. Leticia Franzo de Lima, for providing me all the knowledge of xylose dehydration reactions, and also for the experience on laboratory.
- To MSc. Kathlen Yokoo for the TPD and TPR results.
- To Dr. Fernando Frederico, MSc. Jennifer Tamayo and MSc. Livia Alencar for the HPLC results.
- To Dr. Éder Valdir de Oliveira and to MSc. Mara Medeiros, for the discussions on catalysis.
- To Dr. Silvia Moya for the insights on the catalysts of the project.
- To Lucélia Silva and MSc. Adilson Brandão for the XRD, N_2 adsorption and SEM/EDX results.
- To MSc. Mayra Costa, Gabriel Gusmão de Oliveira, and the other members of LEPCatBior, for the friendship.

I also would like to thank CAPES for the grant during the 4 years of Doctorate. This study was financed by Coordenação de Aperfeiçoamento de Pessoal de Nível Superior - Brasil (CAPES) - Finance Code 001 (file number: 88882.329708/2019-01 - PROEX Program) and it was supported by Fundação de Amparo à Pesquisa do Estado de São Paulo. — FAPESP (process no. 2015/20630-4).

"We favor the sensational and the extremely visible. This affects the way we judge heroes. There is little room in our consciousness for heroes who do not deliver visible results—or those heroes who focus on process rather than results."

Nassim Nicholas Taleb (1960-) - in The Black Swan: The Impact of the Highly Improbable

List of Symbols

Acronyms

LB	-	Lignocellulosic Biomass
C	-	Cellulose
HC	-	Hemicellulose
L	-	Lignin
ARA	-	Arabinose
MAN	-	Mannose
GAL	-	Galactose
XYL	-	Xylose
FUR	-	Furfural
5-HMF	-	5-Hydroxymethyl Furfural
FA	-	Furfuryl Alcohol
THFA	-	Tetrahydrofurfuryl Alcohol
2-MF	-	2-Methylfuran
2-MTHF	-	2–Methyltetrahydrofuran
LA	-	Levulinic Acid
GVL	-	γ-Valerolactone
GBL	-	γ-Butyrolactone
THF	-	Tetrahydrofurfuran
XOL	-	Xylitol
MIBK	-	Methyl Isobutyl Ketone
PBR	-	Packed Bed Reactor
LAS	-	Lewis Acid Sites
BAS	-	Brönsted Acid Sites
CPME	-	Cyclopentyl Methyl Ether
CPO	-	Cyclopentanone
MPV	-	Meerwein–Ponndorf–Verley
CNT	-	Carbon nanotubes
WI	-	Wet Impregnation
IWI	-	Incipient Wetness Impregnation

Acronyms (Continuation)

XRD	-	X-Ray Diffraction
SEM/EDX	-	Scanning Electron Microscopy + Energy-Dispersive X-Ray
H_2-TPR	-	H_2 Temperature Programmed Reduction
NH_3-TPD	-	H_2 Temperature Programmed Desorption
XPS	-	X-Ray Photoelectron Spectroscopy
TEM	-	Transmission Electron Microscopy
PEN	-	Pentose
SMSI	-	Strong Metal–Support Interaction

Nomenclature of the catalysts

NB400	-	$Nb_2O_5 \cdot nH_2O$ calcined at 400 °C
NBAc400	-	$Nb_2O_5 \cdot nH_2O$ treated with H_3PO_4
CoNB10	-	10 wt% Co/Nb_2O_5
CoNBAc10	-	10 wt% Co/Nb_2O_5-H_3PO_4
NiNB10	-	10 wt% Ni/Nb_2O_5
NiNBAc10	-	10 wt% Ni/Nb_2O_5-H_3PO_4
RuNB05	-	5 wt% Ru/Nb_2O_5
RuNBAc05	-	5 wt% Ru/Nb_2O_5-H_3PO_4

Latin Letters

S	-	Selectivity	[-]
X	-	Conversion	[-]
Y	-	Yield	[-]
PEN	-	Pentose	[-]
CB	-	Carbon Balance	[-]

List of Figures

1.1 Scheme of substances over C, HC and L in lignocellulosic biomass. 25
1.2 Substances produced from hydration, hydrogenation and oxidation of furfural. 28
1.3 Number of publications related to furfural since 2016 (only articles). 29
1.4 Acid-catalyzed scheme for furfural production from xylan. 30
1.5 Diagram for Classic Quaker Oats Process. 31
1.6 Process Flow Diagram (PFD) for Furfuryl Alcohol (FA) Production in Gas Phase. 32
1.7 Process Flow Diagram (PFD) for Furfuryl Alcohol (FA) Production in Liquid Phase. 34

3.1 First cyclic mechanism of XYL dehydration (1-OH protonation). 36
3.2 Second cyclic mechanism of XYL dehydration (2-OH protonation). 37
3.3 Acyclic mechanism of XYL dehydration. 37
3.4 Example of mechanism of FUR resinification products. 38
3.5 Example of mechanism of FUR condensation products with XYL intermediates. 39
3.6 Scheme of reactants and humin products obtained during XYL dehydration. 40
3.7 Examples of LAS and BAS in supported metal oxides catalysts. 41
3.8 Production of furfural in liquid phase and byproducts. 45
3.9 Proposed LHHW approach for FA production in liquid phase. 46
3.10 Possible reaction path from FUR to CPO in water. 46
3.11 Adsorption of FUR on varied surfaces. 47
3.12 Mechanism of FUR hydrogenation to FA in Pt-Co/C catalysts in water solution. 48
3.13 Graphic of selected works of XYL to FA production since 2013. 53
3.14 Flowchart for direct conversion of XYL into FA in liquid phase. 53

3.15 Alternatives to produce FA from direct conversion of XYL. 55

3.16 Flowchart of the routes in the direct conversion of XYL to FA in liquid phase. 56

3.17 Acid and metal sites in Pt/ZrO_2-SO_4 catalysts. 59

4.1 Concise flowchart for the preparation and activation of catalysts. 65

5.1 Isotherm for NB400 catalyst. 80

5.2 dVdlog(D) for NB400 catalyst. 80

5.3 Isotherm for CoNB10 catalyst. 80

5.4 dVdlog(D) for CoNB10 catalyst. 80

5.5 Isotherm for NiNB10 catalyst. 81

5.6 dVdlog(D) for NiNB10 catalyst. 81

5.7 Isotherm for RuNB05 catalyst. 81

5.8 dVdlog(D) for RuNB05 catalyst. 81

5.9 Isotherm for NBAc400 catalyst. 82

5.10 dVdlog(D) for NBAc400 catalyst. 82

5.11 Isotherm for CoNBAc10 catalyst. 82

5.12 dVdlog(D) for CoNBAc10 catalyst. 82

5.13 Isotherm for NiNBAc10 catalyst. 83

5.14 dVdlog(D) for NiNBAc10 catalyst. 83

5.15 Isotherm for RuNBAc05 catalyst. 83

5.16 dVdlog(D) for RuNBAc05 catalyst. 83

5.17 XRD patterns for NB400 and NBAc400. 85

5.18 XRD patterns for CoNB10 and CoNBAc10. 86

5.19 XRD patterns for NiNB10 and NiNBAc10. 86

5.20 XRD patterns for RuNB05 and RuNBAc05. 88

5.21 H_2 TPR results - CoNB10 and CoNBAc10. 91

5.22 H_2 TPR results - NiNB10 and NiNBAc10. 91

5.23 H_2 TPR results - RuNB05 and RuNBAc05. 91

5.24 XPS spectrum and fitting for Nb 3d on NB400. 93

5.25 XPS spectrum and fitting for Nb 3d on NBAc400. 93

5.26 XPS spectrum and fitting for P 2p on NBAc400. 93

5.27 XPS spectrum and fitting for Co 2p on CoNB10. 96

5.28 XPS spectrum and fitting for Nb 3d on CoNB10. 96

5.29 XPS spectrum and fitting for Co 2p on CoNBAc10. 96

5.30 XPS spectrum and fitting for Nb 3d on CoNBAc10. 96

5.31 XPS spectrum for P 2p on CoNBAc10. 96

5.32 XPS spectrum and fitting for Ni 2p on NiNB10. 98

5.33 XPS spectrum and fitting for Nb 3d on NiNB10. 98

5.34 XPS spectrum and fitting for Ni 2p on NiNBAc10. 98

5.35 XPS spectrum and fitting for Nb 3d on NiNBAc10. 98

5.36 XPS spectrum for P 2p on NiNBAc10. 98

5.37 XPS spectrum for Ru 3d on RuNB05. 100

5.38 XPS spectrum for Nb 3d on RuNB05. 100

5.39 XPS spectrum for Ru 3d on RuNBAc05. 100

5.40 XPS spectrum for Nb 3d on RuNBAc05. 100

5.41 XPS spectrum for P 2p on RuNBAc05. 100

5.42 TPD results for NB solids. 101

5.43 TPD results for Co solids. 101

5.44 TPD results for Ni solids. 101

5.45 TPD results for Ru solids. 101

5.46 Total acidities (μmolNH_3/g) over TPD studies. 104

5.47 Specific acidities (μmolNH_3/m^2) over TPD studies. 104

5.48 TPD - percentage of weak, medium and strong sites. 104

5.49 PEN conversion, FA, FUR and THFA selectivity - NB400. 105

5.50 Carbon balance - NB400. 105

5.51 Chromatogram at HPLC of the reaction system after 6 h of reaction with NB400 catalyst. 106

5.52 PEN conversion, FA, FUR and THFA selectivity - NBAc400. 107

5.53 Carbon balance - NBAc400. 107

5.54 Chromatogram at HPLC of the reaction system after 6 h of reaction with NBAc400 catalyst. 108

5.55 PEN conversion, FA, FUR and THFA selectivity - CoNB10. 108

5.56 Carbon balance - CoNB10. 108

5.57 Chromatogram at HPLC of the reaction system after 6 h of reaction with CoNB10 catalyst. 110

5.58 PEN conversion, FA, FUR and THFA selectivity - CoNBAc10. 110

5.59 Carbon balance - CoNBAc10. 110

5.60 Chromatogram at HPLC of the reaction system after 6 h of reaction with CoNBAc10 catalyst. 111

5.61 PEN conversion, FA, FUR and THFA selectivity - NiNB10. 112

5.62 Selectivity to XOL, LA, CPO and GVL - NiNB10. 112

5.63 Carbon balance - NiNB10. 112

5.64 Chromatogram at HPLC of the reaction system after 6 h of reaction with NiNB10 catalyst. 114

5.65 PEN conversion, FA, FUR and THFA selectivity - NiNBAc10. 114

5.66 Selectivity to XOL, LA, CPO and GVL - NiNBAc10. 114

5.67 Carbon balance - NiNBAc10. 114

5.68 Chromatogram at HPLC of the reaction system after 6 h of reaction with NiNBAc10 catalyst. 115

5.69 PEN conversion, FA, FUR and THFA selectivity - RuNB05. 116

5.70 Selectivity to XOL, LA, CPO and GVL - RuNB05. 116

5.71 Carbon balance - RuNB05. 116

5.72 Chromatogram at HPLC of the reaction system after 6 h of reaction with RuNB05 catalyst. . . . 117

5.73 PEN conversion, FA, FUR and THFA selectivity - RuNBAc05. . . . 118

5.74 Selectivity to XOL, LA, CPO and GVL - RuNBAc05. . . . 118

5.75 Carbon balance - RuNBAc05. . . . 118

5.76 Chromatogram at HPLC of the reaction system after 6 h of reaction with RuNBAc05 catalyst. . . . 119

5.77 EDX - Metal content before and after the reaction (CoNB10, NiNB10 and RuNB05). . . . 121

5.78 EDX - Metal and P contents before and after the reaction (CoNBAc10, NiNBAc10 and RuNBAc05). . . . 121

7.1 SEM analysis for CoNB10 catalyst. . . . 156

7.2 SEM analysis for NiNB10 catalyst. . . . 156

7.3 SEM analysis for RuNB05 catalyst. . . . 156

7.4 SEM analysis for CoNBAc10 catalyst. . . . 156

7.5 SEM analysis for NiNBAc10 catalyst. . . . 156

7.6 SEM analysis for RuNBAc05 catalyst. . . . 156

7.7 SEM - NB400 after reaction. . . . 157

7.8 SEM - NBAc400 after reaction. . . . 157

7.9 SEM - CoNB10 after reaction. . . . 157

7.10 SEM - CoNBAc10 after reaction. . . . 157

7.11 SEM - NiNB10 after reaction. . . . 157

7.12 SEM - NiNBAc10 after reaction. . . . 157

7.13 SEM - RuNB05 after reaction. . . . 158

7.14 SEM - RuNBAc05 after reaction. . . . 158

7.15 HPLC pattern analysis - XYL. . . . 158

7.16 HPLC pattern analysis - XOL. . . . 158

7.17 HPLC pattern analysis - FA. . . . 159

7.18 HPLC pattern analysis - THFA. 159

7.19 HPLC pattern analysis - LA. 159

7.20 HPLC pattern analysis - GVL. 160

7.21 HPLC pattern analysis - CPO. 160

7.22 HPLC pattern analysis - FUR. 160

List of Tables

1.1 Cellulose (C), hemicellulose (HC) and lignin (L) contents in materials. . . . 24

1.2 Proportion of monomeric units of hemicellulose in different materials containing lignocellulosic biomass. 26

1.3 Applications of FUR and its derivatives. 27

3.1 Activation energies for acid dehydration of XYL (Lewis Acid = $CrCl_3$ and Brönsted Acid = HCl). 40

3.2 Summary of selected works in XYL dehydration reaction and main results. 44

3.3 Activation energies over different bimetallic catalysts in FUR reduction to FA. 50

3.4 Selected works in batch liquid phase FUR reduction to FA. 52

3.5 Combined XYL dehydration and FUR reduction in liquid phase (Amberlyst-15 and Ru/C at 165 °C and 25 bar H_2 pressure) 57

3.6 Combined XYL dehydration and FUR hydrogenation in water-isopropanol liquid phase (1 wt% Pt/ZrO_2-SO_4 at 130 °C and 30 bar H_2 pressure). . . . 59

3.7 Effect of acidity over Cu/SBA-15-SO_3H catalysts in direct FA production from XYL. 60

3.8 Effect of pore sizes over Cu/SBA-15-SO_3H catalysts in direct FA production from XYL. 60

3.9 Effect of H-donor over Co-N-C catalysts in direct FA production from XYL. 61

3.10 Direct conversion of xylose to FA and 2-MF in continuous reactor at different temperatures (5 wt% xylose, 20 wt% water and 75 wt% γ-butyrolacone). 62

4.1 Nomenclature of the solids in the research. 65

4.2 Experimental for calcination of NB into NB400 and NBAc400 supports. . . 66

4.3 Mean experimental values of incipient volumes - NB400 and NBAc400 supports. 67

4.4 Precursors and metal contents selected for IWI methodology. 68

4.5 Parameters for the *ex situ* activation of metallic catalysts (Co, Ni and Ru). 68

4.6 Physical-chemical and acid properties characterizations. 69

4.7 Equipment specifications and parameters in XRD analysis. 70

4.8 Information during the experiments of N_2 adsorption using BET model. . . 71

4.9 Information during the experiments of SEM/EDX. 71

4.10 Equipment specifications and parameters in H_2-TPR experiments - CoNB10, CoNBAc10, NiNB10, NiNBAc10, RuNB05 and RuNBAc05 solids. 72

4.11 Equipment parameters in XPS experiments. 73

4.12 Equipment specifications and parameters in TPD experiments. 74

4.13 Experimental conditions for reactions in Parr converter. 75

4.14 Experimental conditions for analyses at HPLC. 76

4.15 Retention times for studied compounds on HPLC analyses. 77

5.1 Surface area, pore diameter and pore volume in N_2 adsorption. 78

5.2 Textural properties of Co, Ni and Ru supported on Nb_2O_5 support. 80

5.3 Elemental analysis for CoNB10, NiNB10 and RuNB05 after activation on H_2 flow. 83

5.4 Elemental analysis for CoNBAc10, NiNBAc10 and RuNBAc05 after activation on H_2 flow. 84

5.5 Crystalline domain size calculated by XRD patterns. 88

5.6 TPR uptakes and temperature events. 89

5.7 Resume of XPS spectra - NB400 and NBAc400. 94

5.8 Resume of XPS spectra - CoNB10 and CoNBAc10. 95

5.9 Resume of XPS spectra - NiNB10 and NiNBAc10. 97

5.10 Resume of XPS spectra - RuNB05 and RuNBAc05, ... 99

5.11 Total acidity and strength of supports and catalysts studied. 103

5.12 Summary of catalyst performance - PEN conversions (%), selectivities (%) and carbon balance (%) after 360 min. 120

5.13 Summary of catalyst performance - yields to products(%) after 360 min. . 120

5.14 Comparison of RuNB05 to researches on direct FA production from XYL. . 121

Contents

Abstract **4**

Resumo **5**

List of Symbols

List of Figures

List of Tables

1 Introduction **23**

1.1 Overview of Lignocellulosic Biomass 23

1.2 Overview of Furfural Production 29

1.3 Overview of Furfuryl Alcohol Production 32

1.3.1 FA Production in Gas Phase (Classic Process) 32

1.3.2 FA Production in Liquid Phase (Alternative Process) 33

2 Objectives **35**

2.1 General Objective 35

2.2 Specific Objective 35

3 Literature Review **36**

3.1 Furfural Synthesis 36

3.1.1 General Mechanisms (Cyclic and Acyclic) 36

3.1.2 Production of Humins and Role of Acid Sites 37

3.1.3 Types of Heterogeneous Catalysts - Metal Oxides 41

3.1.4 Concluding Remarks for Xylose Dehydration 43

3.2 Furfuryl Alcohol (FA) Production in Liquid Phase 44

3.2.1 Products obtained during FUR hydrogenation 44

3.2.2 General Mechanisms (Classic Approach – External H_2 gas) 45
3.2.3 Solvent - Water 46
3.2.4 Nature of Metals 47
3.2.4.1 Palladium (Pd) and Platinum (Pt) 47
3.2.4.2 Nickel (Ni) 48
3.2.4.3 Cobalt (Co) 49
3.2.4.4 Ruthenium (Ru) 50
3.2.5 Concluding Remarks for Furfural Hydrogenation 51
3.3 Direct Production of FA from XYL in Liquid Phase 52
3.3.1 First Remarks from Literature Articles and Patents 52
3.3.2 Researches in Direct FA Production Since 2016 57
3.3.3 Concluding Remarks for FA Production in Liquid Phase from Xylose 63

4 Methodology **64**

4.1 Selected Supports and Catalysts 64
4.1.1 Calcination of the Supports 66
4.1.2 Acid Treatment 66
4.1.3 Incipient Wetness Impregnation (IWI) 67
4.1.4 Catalyst activation under H_2 flow - Co, Ni and Ru 68
4.2 Catalyst Characterization 69
4.2.1 X-Ray Diffraction (XRD) 69
4.2.2 N_2 Adsorption at 77 K 70
4.2.3 SEM/EDX 71
4.2.4 H_2 - TPR 72
4.2.5 X-Ray Photoelectron Spectroscopy (XPS) 72
4.2.6 NH_3-TPD 73
4.3 Batch Reactions 74
4.4 Identification of the Products 75

5 Results and Discussions **78**

5.1 Characterizations 78

5.1.1 N_2 Adsorption at 77 K - Textural Properties 78

5.1.2 SEM/EDX - Chemical Compositions 83

5.1.3 XRD - Presence of Crystalline Phases 84

5.1.4 H_2 - TPR - Study About the Formation of Active Phases 89

5.1.5 XPS - Oxidation of species 92

5.1.6 NH_3 - TPD - Total Acidity 101

5.2 Reactions Results 104

5.2.1 Catalytic Performance 105

5.2.2 Leaching - Metal Catalysts 121

5.3 Concluding Remarks - Characterizations/Results and Discussions 122

6 Conclusions and Suggestions for Future Works **125**

6.1 Conclusions 125

6.2 Suggestions for Future Works 127

References **128**

7 Appendix **156**

Chapter 1

Introduction

In this section, the role of studies of conversion of biomass is explained. First, the furfural importance as a promising platform molecule is cited. Moreover, some conventional process for production of furfural and furfuryl alcohol are mentioned. In the end, a final remark on the research motivation is described.

1.1 Overview of Lignocellulosic Biomass

According to most of the recent outlooks of energy, our planet will face the greatest challenge in its history. Up to 2040, the primary energy demand may rise almost 70%, though the CO_2 emissions continue to edge up, increasing by about 10%. However, those emissions from oil must reduce at least 45% in an ideal scenario [(Bajwa *et al.*, 2018) and (BP, 2019)]. Therefore, those trends must be taken into account, and our society may discover other alternatives of energy. In this sense, the renewable sources of energy are considered as alternatives for the traditional energy matrix, composed by petroleum and coal (Gallo and Trapp, 2017).

Among them, the most promising renewable technology for the transformation of reactants into chemicals is the valorization of lignocellulosic biomass (LB), a complex network available in cell wall of plant cells (da Costa *et al.*, 2019). Comparing petroleum and LB, the first contains long chains of saturated and insaturated hydrocarbons (McCain Jr, 2017), while the second is composed by different types of cyclic structures and sugars (Mariscal *et al.*, 2016). Moreover, while the separation of petroleum occurs by distillation, i.e., according to different temperatures (McCain Jr, 2017), the biomass separation requires a pretreatment, due to more resistance in its degradation [(Danon *et al.*, 2014), (Delbecq *et al.*, 2018), (Isikgor and Becer, 2015)]. Besides, regarding to LB, it is composed by three major polysaccharides: cellulose (C), hemicellulose (HC) and lignin (L). The Table 1.1 provides the contents of those sugars in a large range of materials, where C and HC are present at about 70 wt.% of samples.

Table 1.1: Cellulose (C), hemicellulose (HC) and lignin (L) contents in materials.

Material	Cellulose	Hemicellulose	Lignin
Sugarcane bagasse	55	11	25
Corn stover	32-40	17-35	7-18
Wheat straw	50	30	15
Rice straw	36-47	17-35	9-18
Switchgrass	45	30	12-20
Hardwood stems	40-55	24-40	18-25

Source: Adapted from Aguiar *et al.* (2010) and Ussiri and Lal (2014).

All of the polysaccharides units have their repetition units, as provided in Figure 1.1. First, the cellobiose units forms the cellulose, which is more crystalline and resistant to hydrolysis compared to hemicellulose. Second, pentoses and hexoses constitutes HC hemicellulose and third, the lignin, which is usually removed as a residue in processes, is a polymer of varied polyphenol units (Isikgor and Becer, 2015).

Figure 1.1: Scheme of substances over C, HC and L in lignocellulosic biomass.

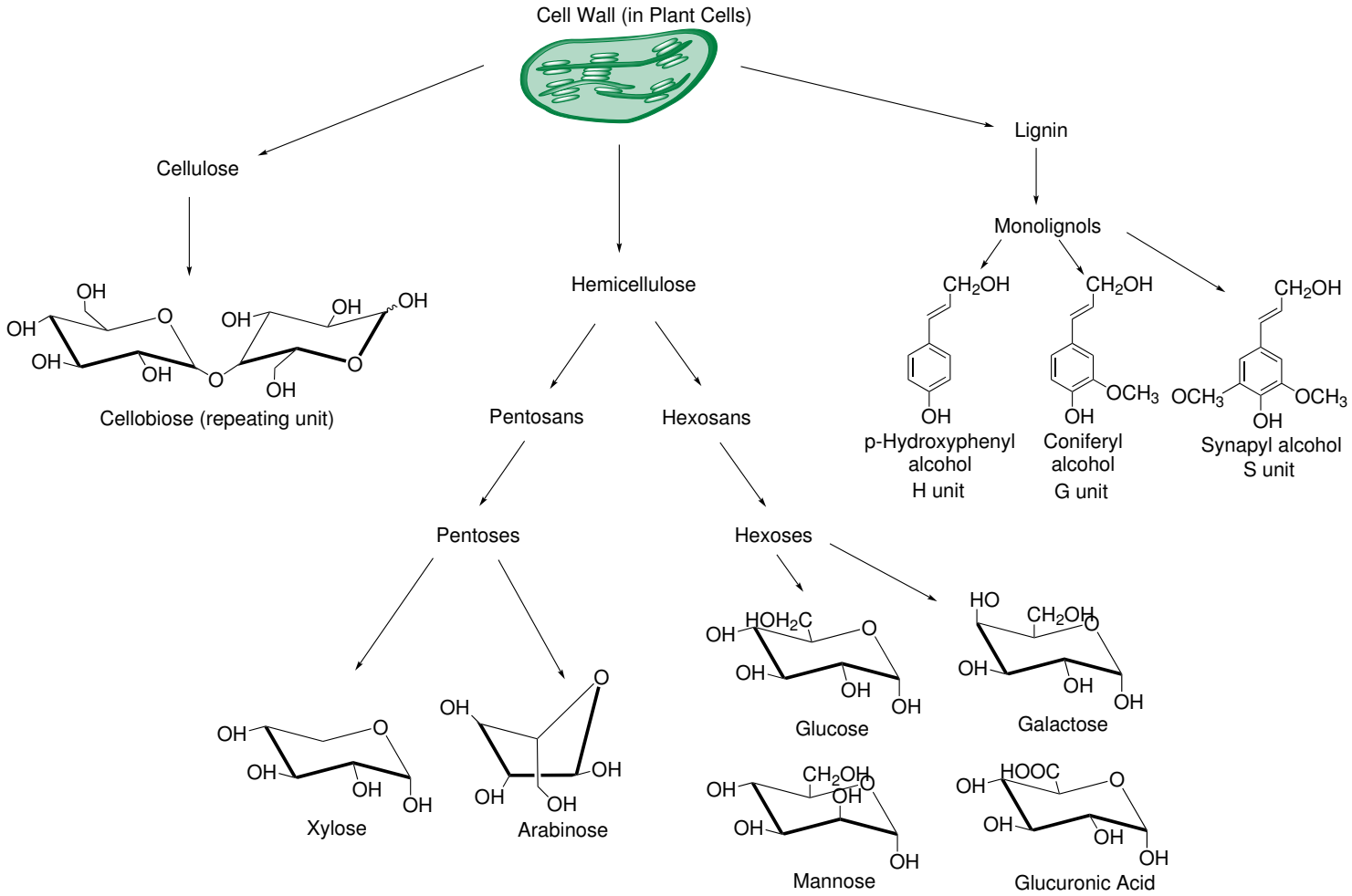

Source: Adapted from Duval and Lawoko (2014), Maki-Arvela *et al.* (2011), Rinaldi *et al.* (2019), Li *et al.* (2013).

As shown in Table 1.1 and Figure 1.1, the hemicellulose accounts for around 17% to 40% of the lignocellulosic biomass content. It is an amorphous and chemically heterogeneous structure composed by carbohydrate heteropolymers like xylan, arabinoxylan and glucomannan [(Mariscal *et al.*, 2016), (Isikgor and Becer, 2015)]. Furthermore, Table 1.2 shows the proportion of hemicellulose monomer units in some sources of LB (Isikgor and Becer, 2015).

Table 1.2: Proportion of monomeric units of hemicellulose in different materials containing lignocellulosic biomass.

Feedstock	Composition			
	XYL (%)	ARA (%)	MAN (%)	GAL (%)
Sugarcane bagasse	20.5-25.6	2.3-6.3	0.5-0.6	1.6
Corn straw	14.8-25.2	2.0-3.6	0.3-0.4	0.8-2.2
Corn cob	28.0-35.3	3.2-5.0	-	1.0-1.2
Rice straw	14.8-23.0	2.7-4.5	1.8	0.4
Wheat straw	19.2-21.0	2.4-3.8	0-0.8	1.7-2.4
Hardwood [a]	14.0-19.1	0.6-1.0	1.0-2.0	1.0-1.9
Softwood [b]	5.3-10.6	2.0-4.2	5.6-13.3	1.9-3.8

a: Species *Eucalyptus globulus*, b: Species *Pinus pinaster*

Source: Adapted from Gírio *et al.* (2010).

In Table 1.2, it was reported that xylose - XYL (the repetition unit of xylan) is one of the most predominant and important monomers among lignocellulosic biomass. Indeed, xylose can be dehydrated to produce furfural (FUR), which is a platform molecule that is very reactive and it can produce over 80 other compounds. The main industrial use of furfural is as an industrial solvent, and 60% of furfural production accounts for production of furfuryl alcohol (FA) (Mariscal *et al.*, 2016). The production of furfural is about 250,000 t/year with China as market leader (90%), followed by South Africa and Dominican Republic (Bhaumik and Dhepe, 2016). Besides, FUR market is expected to grow in a Compound Annual Growth Rate (CAGR) of 11.6%, especially in Asia-Pacific, reaching US$ 1.434 billion revenue by 2022 (Dalvand *et al.*, 2018). The Figure 1.2 below provides a better forecast of some products that may be produced from XYL, and obviously FUR, in LB.

It can be noted in Figure 1.2 the reason which furfural is the most promising molecule from biorefineries, once it may produce a variety of substances with different functional groups (from alcohols to acids). For instance, the hydrogenation of furfural includes the formation of important molecules for chemical industry, *e.g.* furfuryl alcohol (FA), tetrahydrofurfuryl alcohol (THFA) and even 2-methyltetrahydrofuran (2-MTHF). Also, the presence of water in reaction media may provide the conversion of FA into levulinic acid (LA), which may be converted to γ-valerolactone (GVL) in H_2 atmosphere. In another route, H_2 can transform FUR in 2-methylfuran (2-MF), 2-pentanone and pentanol-2. To conclude, the presence of oxygen makes furfural react into furoic acid, furan and tetrahydrofuran (THF). All of those compounds have extensive roles at chemical industry, as stated in Table 1.3.

Table 1.3: Applications of FUR and its derivatives.

Compound	Main application
Furfural (FUR)	Organic solvent
Levulinic Acid (LA)	Solvent, fine chemicals manufacture
GVL	Starting material for adipic acid
Furfuryl Alcohol (FA)	Industry of resins, adhesives and wetting agents
THFA	Green solvent
2-MTHF	Biofuel, solvent
2-MF	Biofuel, solvent
2-Pentanone	Flavoring additive in food industry
Pentanol-2	Solvent
Furoic Acid	Production of furoate esters
Furan	Polymer industry
THF	Adhesives, precursor and PVC cements

Source: Adapted from Mariscal *et al.* (2016), Dalvand *et al.* (2018), Dutta *et al.* (2012), Yan *et al.* (2014), Kohli *et al.* (2019), Fang *et al.* (2017b).

Figure 1.2: Substances produced from hydration, hydrogenation and oxidation of furfural.

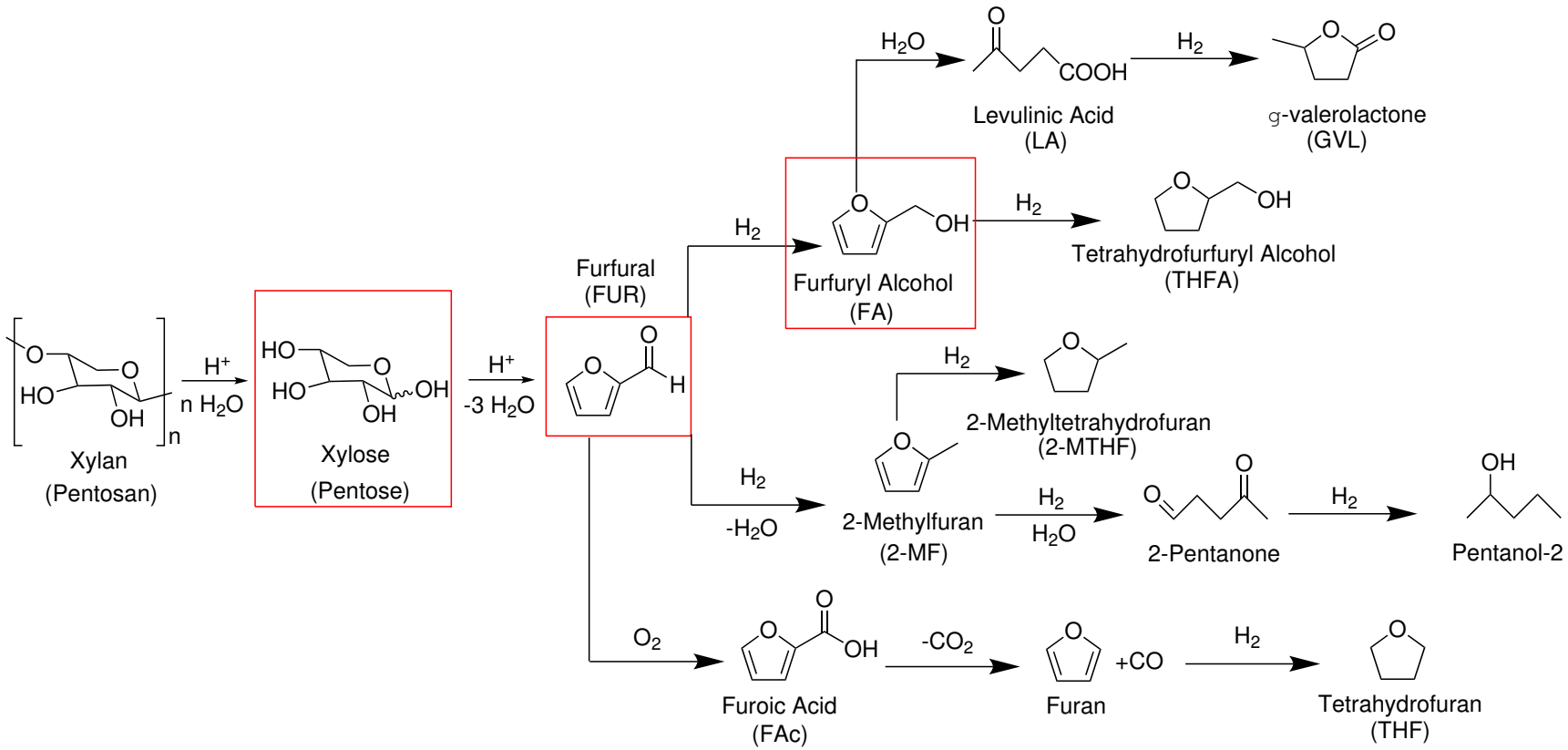

Source: Adapted from Mariscal *et al.* (2016), Wang *et al.* (2019), Dutta *et al.* (2012).

Yet the first researches about furfural production and its derivatives synthesis are not recent, the interests for this topic were increasing year after year, as provided in Figure 1.3. Regarding to furfural, the recent literature aim for more efficient heterogeneous catalysts, that may be able to improve the furfural yield and reduce the content of humins, making the process less aggressive to nature. In addition, the heterogenous catalysis may improve the industrial process for FUR synthesis.

Our literature review is divided into four main parts: solid catalysts for furfural synthesis, heterogeneous catalysts for furfuryl alcohol production, the one-pot conversion of xylose into furfuryl alcohol and properties of niobia-based materials. The sections of synthesis of furfural and furfuryl alcohol provides first the industrial process and then how the heterogeneous catalysis may improve them.

Figure 1.3: Number of publications related to furfural since 2016 (only articles).

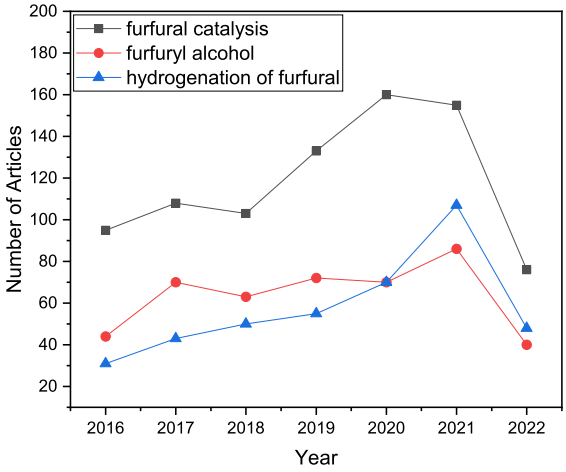

Source: Web of Science – search TI = (furfural and catal*), TI = (furfuryl alcohol), TI = (furfural AND hydrogenation). Date of search: 13/07/2022.

1.2 Overview of Furfural Production

FUR can be obtained through two main routes: the catalytic oxidation of 1,3-dienes derived from fossil-based materials or the acid-catalyzed transformation of sugars present in biomass. This second route is one of the most relevant for establishment of biorefinery concept, with the example of Quaker Oats process developed in 1920s (Brownlee, 1933a).

The classic Quaker Oats process is based in a two steps approach: 1) hydrolysis of lignocellulosic biomass to release pentoses in acidic medium using mineral acids

and 2) cyclodehydration of pentosane units to produce furfural. The hydrolysis of C5 polysaccharides is carried out in H_2SO_4 or H_3PO_4 diluted in water at average temperatures and pressures (160 °C and 10 atm). However, this step releases high amounts of energy and lowers the pH of solution to 1.0, which may increase the corrosion of process equipment. After the formation of xylose from xylan, it is dehydrated to furfural in the acidic medium [(Brownlee, 1933a), (Brownlee, 1933b), (Brownlee, 1938), (Dashtban *et al.*, 2012)]. Also, it is important to remark that the classic process for furfural production requires a batch reactor and it is catalyzed by homogeneous catalysts, which requires more energy for separation (next section). The Figure 1.4 below provides a major scheme for furfural production for pentosans.

Figure 1.4: Acid-catalyzed scheme for furfural production from xylan.

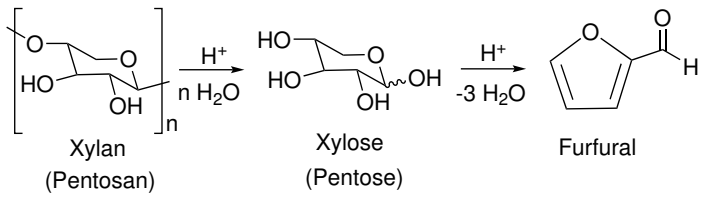

Source: Adapted from Mariscal *et al.* (2016) and Zhou and Zhang (2016).

After the reaction, FUR is produced in the acid solution. Then, the lignin and liquor produced are extracted from the reaction medium and low-pressure steam is mixed to carry out an azeotropic separation. Finally, the furfural is separated by a double system of distillation columns, because there are byproducts produced by the reaction, such as methanol and formic acid [(Brownlee, 1933a), (Brownlee, 1933b), (Brownlee, 1938)]. The Figure 1.5 summarizes all the previous stages in a flowchart for the classic Quaker Oats Process.

The best chemical yield for furfural is only 62% at the optimal conditions of Bronwlee's process, nevertheless there is loss of almost 16% of the total furfural produced (Brownlee, 1938). Indeed, the steam consumption only in distillation system is 16.2 kg of steam per kg of furfural produced. As a matter of fact, we can enumerate several drawbacks for the classic Quaker Oats process [(Brownlee, 1933a), (Brownlee, 1938)], for example:

- High residence time in batch reactor – minimum of 3.3 h.

- The reduced pH produces very acid residues, which need treatment to be neutralized.
- Before going to the mixer, the biomass needs previous preprocessing, and the fines may be blown by the steam.
- Even at 160 °C, the amount of required H_2SO_4 is 6% by weigh of solution.
- The moisture content in biomass determines the conversion of reactor. More moisture means less furfural yield.

Figure 1.5: Diagram for Classic Quaker Oats Process.

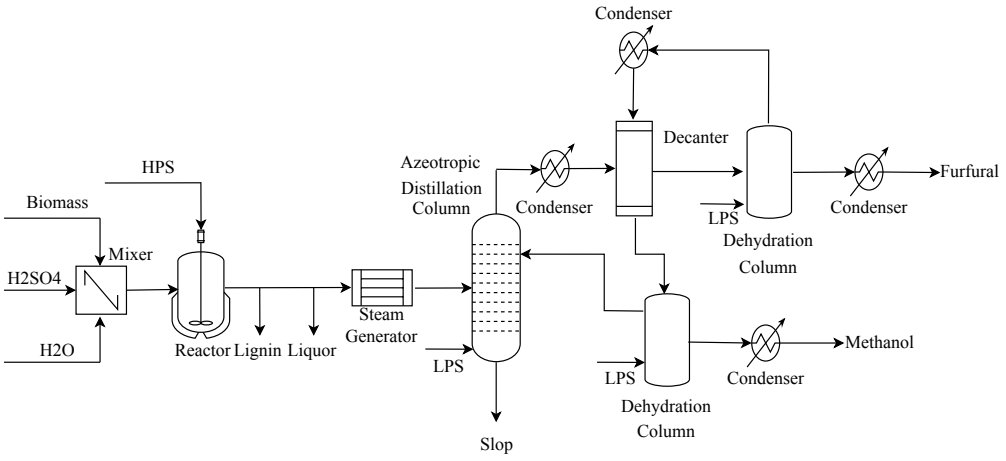

Source: Adapted from Brownlee (1938).

Later on, the Quaker Oats Company tried to develop a continuous reactor for the FUR production, without success. The main challenge for heterogeneous catalysts (*i.e.*, solid acids) in furfural synthesis is to provide yields higher than mineral acid, but also to curb the formation of humins – a condensation product from furfural and biomass. As provided in the next sections, the dehydration of xylose may be carried out in batch or continuous operations and with only water or other cosolvents. The reader may find information about homogeneous dehydration of xylose in more reviews or patents [(Danon *et al.*, 2014), (Dashtban *et al.*, 2012), (Koch and Kindler, 2015), (Burket and Sabesan, 2015), (Marcotullio, 2011), (Wettstein *et al.*, 2012)].

1.3 Overview of Furfuryl Alcohol Production

1.3.1 FA Production in Gas Phase (Classic Process)

The production of FA from FUR involves three main stages: the evaporation of FA, the reaction in a PBR (packed-bed reactor) and the final separation of FA and derivatives (Figure 1.6). In the first stage of process, liquid FUR is fed into an evaporation system. The system is composed of a circulation pump, a heater and a packed column. Once the FUR is maintained at 120 °C, it is fed into the top of the packed column. At the same time, a stream of hydrogen (H_2) flows upwards in the column. Later, the mixture of furfural and H_2 is superheated before it flows into the tubular packed bed reactor, which is at 135 °C. After the reaction section, the gaseous mixture enters a cooling system consisted of a packed column, a pump and a cooler. A purge stream removes the polymer and the resinification products from the system. Also, the FA is separated in a vacuum distillation. In the final part of process, a mixture of water, FUR and 2-MF is also removed from system [(Zeitsch, 2000),(Peters Jr, 1937), (Swadesh, 1956), (Kozinski, 1980)].

Figure 1.6: Process Flow Diagram (PFD) for Furfuryl Alcohol (FA) Production in Gas Phase.

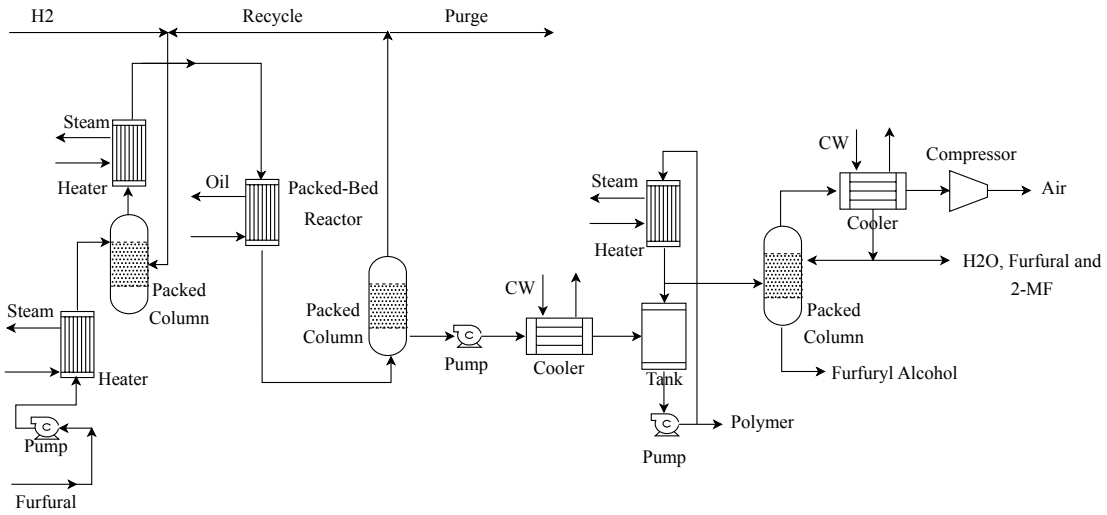

Source: Adapted from Zeitsch (2000) and Swadesh (1956).

Regarding to the reaction section, the bulk catalyst of copper chromite is generally used for FUR reduction ($Cu_2Cr_2O_5$ or $CuCr_2O_4{\cdot}CuO$). In best conditions, the FA yield is 92% and the main byproduct produced is 2-MF [(Zeitsch, 2000), (Swadesh, 1956),

(Frainier and Fineberg, 1981)]. However, we have some opportunities to improve the reaction stage:

- Chromium substances in copper chromite catalysts are very toxic for the environment. Therefore, the discard and regeneration of this type of catalyst is difficult (Liu *et al.*, 2013).

- The converter startup is not simple. First, the temperature is increased slowly rate (3 °C per day) from 120 °C to 152 °C – the operation temperature. This is due to the formation of carbonaceous deposits. Second, the reactor must be heated up to 220 °C in order to clean deposits by oxidation. Finally, the catalyst is reactivated by hydrogenation at 160 °C (Zeitsch, 2000).

- At 200 °C, the cooper chromite catalyst is deactivated. The mechanism of deactivation is the poisoning due to strong adsorption of polymeric species in Cu sites and/or by coke formation. At 300 °C, the selectivity to FA decreased (increasing amounts of 2-MF) and characterizations showed that Cr atoms probably covered Cu active sites (Liu *et al.*, 2013).

On the other hand, even in the first patents, as suggested by Mastagli (1956) and Peters Jr (1937), we observed several studies in hydrogenation of furfural in liquid phases with metal catalysts, such as Ni, Pd or Ru. The conditions of liquid phase were milder, with 20 bar and *ca.* 100 °C.

1.3.2 FA Production in Liquid Phase (Alternative Process)

FA can also be produced in liquid phase using a slurry continuous reactor, as expressed in Figure 1.7. In the first stages of process, cooper chromite in powder is mixed with furfural in a tank. After the mixture, the slurry is pumped to a continuous tubular reactor (about 200 atm and 120 °C), where the compressed H_2 reacts with the slurry. The remaining gas is separated from the slurry using a cyclone, and H_2 is recompressed to the reactor. On the other side, the slurry is pumped to a centrifuge, where it is separated with sedimentation. Finally, the final mixture (consisted of solids, FA and gases) is separated in a low-pressure column (Zeitsch, 2000).

Figure 1.7: Process Flow Diagram (PFD) for Furfuryl Alcohol (FA) Production in Liquid Phase.

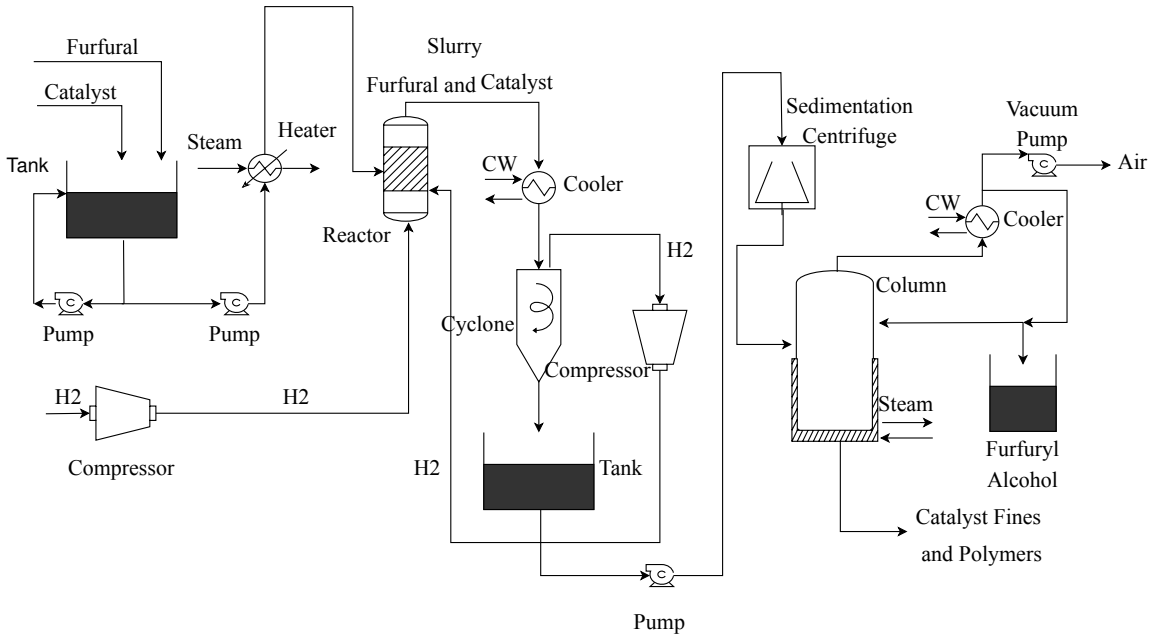

Source: Adapted from Zeitsch (2000) and Swadesh (1956).

Nevertheless, even the continuous process in liquid phases provides serious drawbacks, as given below:

- As the catalyst is used in powder, there are significant costs for the separation of the fines in the end of process. Furthermore, if the catalysts were used in pellets instead, the cost of pumping the reactants into the converter would be decreased.
- The high pressure conditions of reaction in the first designs of process made the operation difficult (Zeitsch, 2000).
- Researchers exposed that slight modifications in process variables may increase the selectivity to THFA instead of FA (Mastagli, 1956).

Those reasons show that researches about catalyst design in furfural hydrogenation (in gas or liquid phase) are still necessary. Moreover, an integrated process (and catalyst) for FA synthesis directly to xylose would be another upgrade in biomass conversion.

Chapter 2

Objectives

The general and specific objectives of this thesis are described below.

2.1 General Objective

- Study of catalysts with non-noble and noble metals (Co, Ni and Ru) supported on niobia and phosphated niobia on direct conversion of XYL to FA.

2.2 Specific Objective

- Investigation of the influence of phosphate treatment to modify niobia acidity on the performance of niobium oxide based catalysts for XYL conversion.
- Production and evaluation of catalysts with metal and acid sites on XYL transformation into varied products (FA, THFA, XOL, LA).
- Comparison of catalytic performance of base (Co, Ni) and noble metal (Ru) supported on different niobia supports for XYL conversion in aqueous medium.

Now, our literature review will be divided into three major parts from 2016 to 2020: the production of furfural, the production of FA in liquid phase and the direct synthesis of xylose to FA.

Chapter 3

Literature Review

3.1 Furfural Synthesis

3.1.1 General Mechanisms (Cyclic and Acyclic)

As referred to the XYL dehydration, two major mechanisms were proposed in literature: the direct route and the indirect route. The first one regards to cyclic XYL, with a source of H^+, *i.e.*, a Brönsted acid [(Rasmussen and Sørensen, 2014), (Nimlos *et al.*, 2006)]. The cyclic mechanism might have two paths: 1) the attack of H^+ in the oxygen atom bonded in carbon 1, also called 1-OH protonation, that includes a xylosyl cation and the cleavage of C5-O linkage (Figure 3.1) or 2) the 2-OH protonation, which provides a shorter path to FUR (Figure 3.2). When both routes were compared quantum mechanics studies provided information that the most probable path in cyclic dehydration of XYL is the attack of carbon 2 (Nimlos *et al.*, 2006). Furthermore, researchers also verified that no hydrogen of the solvent is exchanged in cyclic dehydration in acid media, so the change in acidity comes from Brönsted acids (Eitelman and Horton, 2006).

Figure 3.1: First cyclic mechanism of XYL dehydration (1-OH protonation).

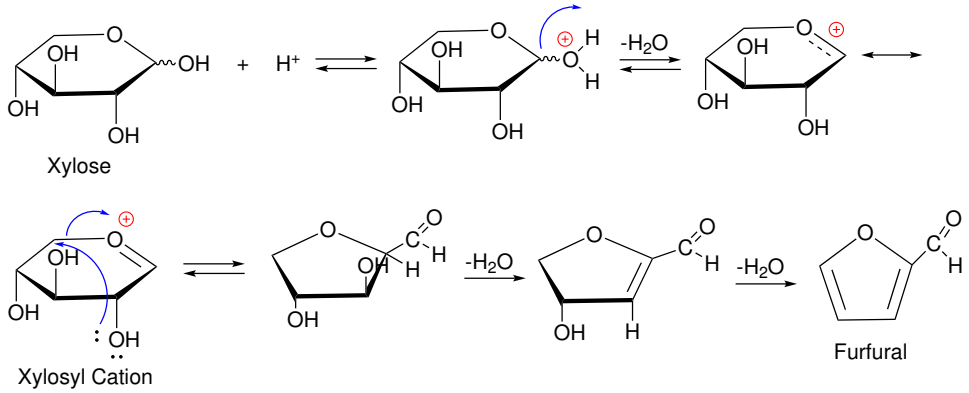

Source: Adapted from Antal Jr *et al.* (1991) and Ahmad *et al.* (1995).

Figure 3.2: Second cyclic mechanism of XYL dehydration (2-OH protonation).

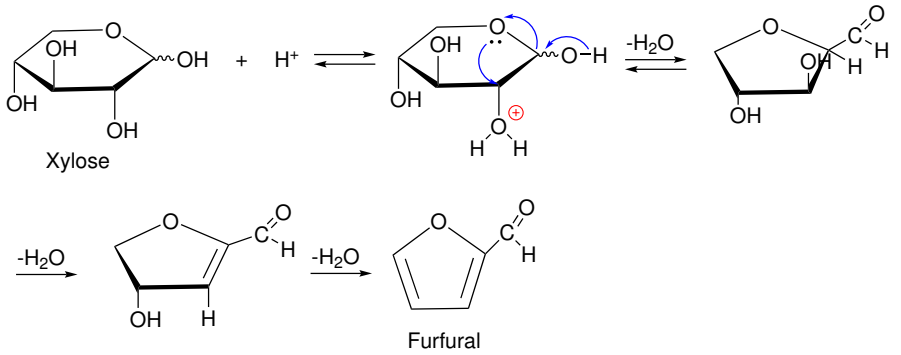

Source: Adapted from Antal Jr *et al.* (1991) and Ahmad *et al.* (1995).

On the contrary, the second path for FUR production is the indirect route, or acyclic mechanism (Figure 3.3). This mechanism begins with XYL transformation to its acyclic form in open chain and subsequent enolization or direct conversion to xylulose, an isomer form XYL, through hydride transfer. In this path, it was also detected the presence of lyxose among byproducts (Enslow and Bell, 2015).

Figure 3.3: Acyclic mechanism of XYL dehydration.

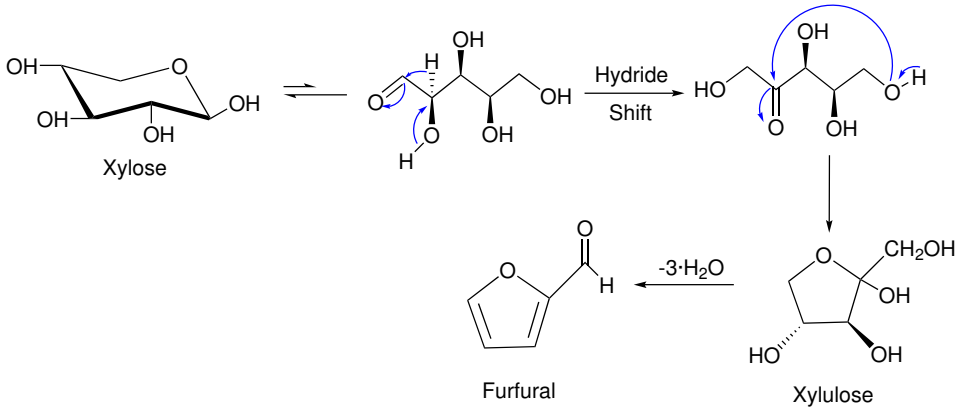

Source: Adapted from Enslow and Bell (2012).

3.1.2 Production of Humins and Role of Acid Sites

During the reactions depicted in Figure 3.1 to Figure 3.3, not only XYL, but also a large spectrum of byproducts are present. For example, the production of isomers from xylose (xylulose and lyxose) are reported in literature [(Antal Jr *et al.*, 1991),(Moura, 2019), (Doiseau, 2014), (Möller and Schröder, 2013), (Zhu *et al.*, 2017b)]. Besides, as FUR is a very reactive molecule, it can undergo to frag-

mentation reactions, leading to products with open chain, such as glyceraldehyde, glycoaldehyde, formic acid, acetol and formaldehyde (Moura, 2019). FUR can react with other FUR molecules, which constitutes the resinification loss reactions [(Mariscal *et al.*, 2016),(Zeitsch, 2000),(Möller and Schröder, 2013)]. As depicted in Figure 3.4, those mechanism occurs on an acid medium. Besides, the resinification reactions may take place even at mild conditions (Mariscal *et al.*, 2016).

Figure 3.4: Example of mechanism of FUR resinification products.

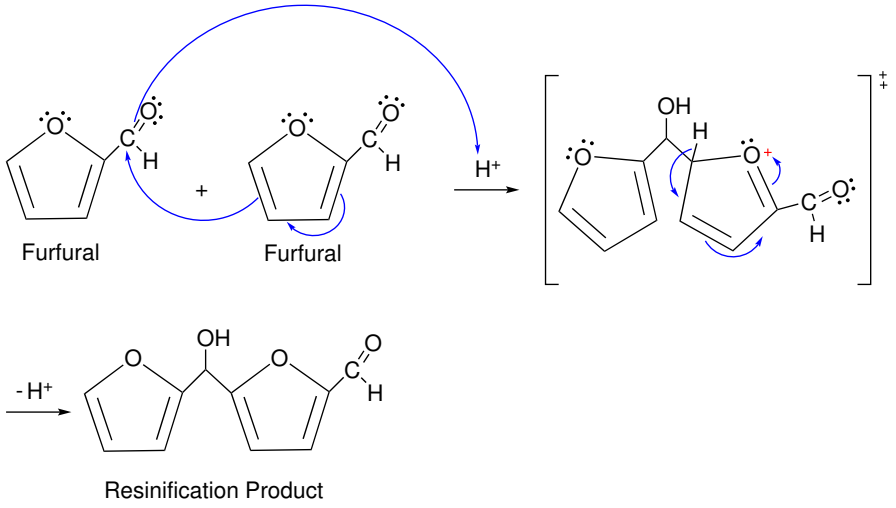

Source: Adapted from Enslow and Bell (2015).

Although the aforementioned byproducts are undesired, probably the most concern about XYL dehydration rely on the formation of humins. At first, humins are dark and insoluble polymeric molecules that attach to the solid catalyst, due to their strong adsorption [(Filiciotto *et al.*, 2018), (Enslow and Bell, 2015), (Dulie *et al.*, 2020)]. Besides, they are produced in condensation reactions, where the FUR molecule reacts with other components (Figure 3.5).

One of the drawbacks in humins production is the blocking of catalytic sites, which makes the furfural yield decreases in heterogenous catalysts. Therefore, due to great possibility of humins formation, the reduction in humins production is a crucial objective when heterogeneous catalysts are designed for XYL dehydration (Dalvand *et al.*, 2018).

Figure 3.5: Example of mechanism of FUR condensation products with XYL intermediates.

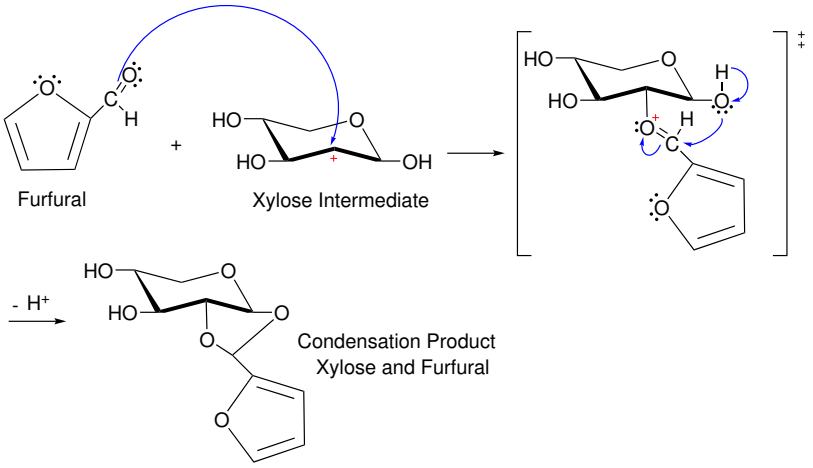

Source: Adapted from Enslow and Bell (2015).

Among the factors which provide humin formation, one may cite: temperature, substrates and concentration of acid species. At higher temperatures, the formation of humins is reduced, though the presence of substrates besides FUR increased their production (*i.e.*, glucose or XYL instead of only FUR) . In other words, the acid concentration provided low dependence on humin production (van Zandvoort *et al.*, 2013).

Both Lewis acid sites (LAS – electrons acceptors) and Brönsted acid sites (BAS – H^+ donors) in solid catalysts play a major role in the XYL dehydration to FUR, according to Choudhary *et al.* (2011) and Choudhary *et al.* (2012). Those works carried out XYL dehydration using Lewis ($CrCl_3$) and Brönsted acids (HCl) (Choudhary *et al.*, 2012). Their results demonstrated that the LAS promoted an isomerization of XYL into xylulose, whereas the BAS converted xylulose to FUR and even XYL to FUR directly. Also, the reported activation energies for both route presented 39% more energy for BAS (Table 3.1).

At Table 3.1, one could realize that a great amount of LAS would be enough for XYL dehydration. However, some experiments showed that strong LAS promoted the formation of degradation products of both XYL and FUR (including humins), [(Weingarten *et al.*, 2011), (Pholjaroen *et al.*, 2013), (Chatterjee *et al.*, 2018)]. Furthermore, even an excess of LAS produced more intermediate products, due to higher adsorption of carbohydrates at those sites [(Weingarten *et al.*, 2011), (Pholjaroen *et al.*, 2013)]. Then, a

higher BAS/LAS ratio is better in order to increase the FUR selectivity though decreasing the activity of the catalyst [(Gupta *et al.*, 2017), (You *et al.*, 2014)]. To summarize all the previous information, the Figure 3.6 provides a summary of most of possible products in XYL dehydration carried out in aqueous media.

Table 3.1: Activation energies for acid dehydration of XYL (Lewis Acid = $CrCl_3$ and Brönsted Acid = HCl).

Type of Acid Site	Route	Apparent Activation Energy (kJ/mol)
Brönsted	Direct	133.8
Lewis	Indirect	64.9
Brönsted	Indirect	96.7

Source: Adapted from Choudhary *et al.* (2012).

Figure 3.6: Scheme of reactants and humin products obtained during XYL dehydration.

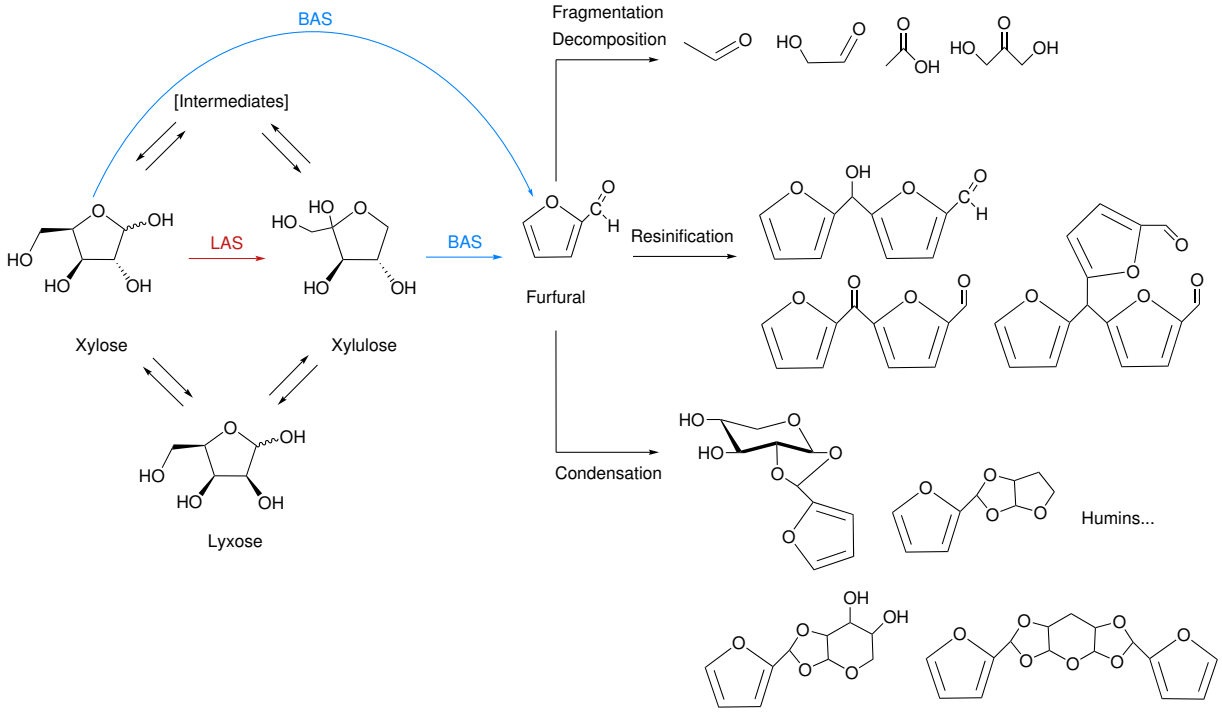

Source: Adapted from Enslow and Bell (2015) and Moreau *et al.* (2004).

3.1.3 Types of Heterogeneous Catalysts - Metal Oxides

According to literature, the amorphous oxides might improve XYL dehydration due to structures the random structures on surface and larger pore sizes compared to micropores in zeolites [(Bhaumik and Dhepe, 2016), (You *et al.*, 2014), (Goldsmith *et al.*, 2017)]. On the other hand, some difficulties arise in control of pore size.

Regarding to the XYL dehydration, oxides are preferred, once their sites might be water-tolerant (García-Sancho *et al.*, 2014). At the same time, though, most of the oxides used as catalysts lacks BAS. Therefore, the use of oxides with BAS or the functionalization of surface groups with BAS would be necessary. Another option is to support two different oxides, which provides potential sites for LAS and BAS, as designed by de Lima *et al.* (2021).

Figure 3.7: Examples of LAS and BAS in supported metal oxides catalysts.

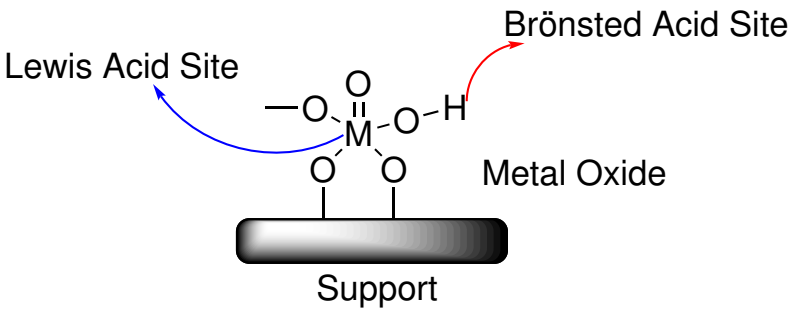

Source: Adapted from Bhaumik and Dhepe (2017).

Since 2016, many studies with SiO_2 catalysts have been reported in FUR production [(Millán *et al.*, 2018), (Bhaumik and Dhepe, 2017), (Campos-Molina *et al.*, 2017), (You *et al.*, 2016)]. Bhaumik and Dhepe (2017) carried out xylan conversion using silica both as support and bulk catalyst. At 170 °C in a water-toluene medium, the SiO_2 support presented only 28% of FUR yield, though WO_3/SiO_2 provided 53% of FUR yield. In characterization analysis, the authors pointed out that the support gave a high metal oxide dispersion, with the formation of very acid species - silicotungstic ones. Besides, it is important to remark that the WO_3/SiO_2 catalyst was active during 8 cycles of reactions. Also, Campos-Molina *et al.* (2017) used silica modified with PSSA nanocomposites. At 180 °C, the SiO_2-PSSA catalyst presented almost 70% of FUR yield in water and CPME medium in the first cycle. However, even with the high acidity, the

yield decreased to about 20% in the next runs, the same value of the support. According to the author, those were evidences of the leaching of the acid groups (Campos-Molina *et al.*, 2017). Then, the leaching is an issue on acid groups.

Other oxide suitable for xylose dehydration has also gained attention from scientists. Niobium pentoxide (Nb_2O_5) has many oxidation states (from +5 to -1), which promotes variety in the structures. Moreover, Nb_2O_5 is composed of NbO_6 octahedra, that are connected by edges and corners. In the case of hydrated niobium oxide, or acid niobia ($Nb_2O_5 \cdot nH_2O$) the acid strength is high (pKa from -5 to -4), and it remains bound to supports, which decreases leaching [(Kreissl *et al.*, 2016), (Kreissl *et al.*, 2017), (Nakajima *et al.*, 2010), (Nakajima *et al.*, 2011)].

The major advantage of acid niobium oxide is the presence of both natural LAS and potential BAS. The pretreatment temperature above 100 °C curb the BAS formation, while LAS remain active up to 500 °C, according to Kim and Lee (2001). We will remark that many recent articles used niobia in their results [(Gupta *et al.*, 2017), (de Carvalho *et al.*, 2019), (Vieira *et al.*, 2020), (Fang *et al.*, 2017a)].

The results of Gupta *et al.* (2017) showed that Nb_2O_5 had resistant and water-tolerant sites. First, in water medium at 120 °C, their Nb_2O_5 catalyst had 93% of XYL conversion and 48% of FUR selectivity. This result was remarkable compared to other tested catalysts, such as HCl, Na^+/Nb_2O_5 and even $Sc(OTf)_3$. Second, when the Nb_2O_5 catalyst was tested in a large range of solvents – toluene, xylene and THF, the first was detected as the best solvent, due to suppression of humins formation and maintenance of activity. The authors concluded that the LAS of niobia and the ability to carry out an extraction with toluene were crucial for FUR production (Gupta *et al.*, 2017).

Gallo and co-workers carried out the conversion of glucose and XYL in Nb_2O_5 catalysts (Vieira *et al.*, 2020). They stated that niobium oxide may act as LAS and BAS catalyst in XYL dehydration, then, no additional mineral acid is required on conversion. The batch reactor containing THF/H_2O at 120 °C mixture provided 95.4% of XYL conversion and 46.8% of FUR selectivity in Nb_2O_5 catalyst. That solid was also tested in continuous reactor, providing high stability and no leaching. The researchers concluded that niobium catalysts had performance compared to mineral acids (Vieira *et al.*, 2020).

3.1.4 Concluding Remarks for Xylose Dehydration

In this section, the general mechanisms, the role of acid sites and the most recent results of xylose dehydration were analyzed. The main points in xylose dehydration reaction are:

- Both Lewis and Brönsted acid sites (LAS and BAS) are used in xylose dehydration. However, a solid catalyst containing only BAS is not enough, because is similar to mineral acids. Furthermore, strong LAS tend to promote the isomerization of xylose to other side products that decrease furfural selectivity. Then, a combined approach of LAS and BAS must be done in design of heterogeneous catalysts.

- In several reactions, the use of a bulk catalyst was more pronounced in xylose dehydration. Therefore, the use of transition oxides metals may represent an opportunity to create industrial catalysts at reduced costs.

- If the reaction is carried out only in water, there is more chance to formation of resinification and condensation reactions. To overcome this, a co-solvent may be mixed with water to extract furfural or to avoid contact with a solid catalyst. Among many tested co-solvents, GVL appears at a good candidate. Even if hydrocarbons, such as toluene, provided better results, it is not advisable to use them, due to the high impact in environment.

To summarize this section, Table 3.2 showed selected works in xylose dehydration reaction since 2016, with conversions of XYL and FUR yields obtained.

Table 3.2: Summary of selected works in XYL dehydration reaction and main results.

Catalyst	Solvent/Co-Solvent	T (°C)	Y_{FUR} (%)	Reference
WO_3/SiO_2	H_2O/TOL	170	53	Bhaumik and Dhepe (2017)
Ion Resin	H_2O/TOL	120	86	Pawar (2020)
MCM-41-SO_3H	H_2O/TOL	155	88	Kaiprommarat *et al.* (2016)
HPAs Preyssler	DMSO	140	72	Pardo Cuervo *et al.* (2020)
ZSM-5	GVL/H_2O	190	70	Bruce *et al.* (2016)
Carbon Solid	GVL	170	79	Zhang *et al.* (2016)
Carbon Solid	GVL	120	50	Laohapornchaiphan *et al.* (2017)
Nb_2O_5	H_2O	180	41	Fang *et al.* (2017a)
ZnCuO	H_2O	150	62	Mishra *et al.* (2019)
SiO_2-Al_2O_3	H_2O	200	29	You *et al.* (2016)
SiO_2-PSSA	H_2O/CPME	180	60	Campos-Molina *et al.* (2017)

3.2 Furfuryl Alcohol (FA) Production in Liquid Phase

3.2.1 Products obtained during FUR hydrogenation

A large number of products can be produced during FUR hydrogenation in liquid phase. As first examples, the hydrogenation of C=C bonds inside FUR ring produce tetrahydrofurfuryl alcohol (THFA). Besides, FA can be dehydrated to 2-MF, in a hydrogenolysis path. A cleavage of C=O bond in FUR, produces furan from FUR decarbonylation. Furthermore, the presence of water promotes the synthesis of levulinic acid (LA), and consequently, γ-valerolactone (GVL) from FA [(Albilali *et al.*, 2018),(Giorgianni *et al.*, 2018), (Chen *et al.*, 2018)].

The Figure 3.8 provided the paths of FUR hydrogenation and ring opening to butanol and 1,5-pentanediol. It is also important to point out that the reactions of condensation and resinification of FUR also take place in liquid phase [(Mariscal *et al.*, 2016), (Chen *et al.*, 2018), (Hronec and Fulajtarová, 2012), (Panagiotopoulou *et al.*, 2014)].

Nonetheless, the source of hydrogen varies according to the approach in FUR

hydrogenation: the external source of H_2 gas (classic approach) or the use of protic solvents to replace gaseous H_2 (catalytic transfer hydrogenation or CTH).

Figure 3.8: Production of furfural in liquid phase and byproducts.

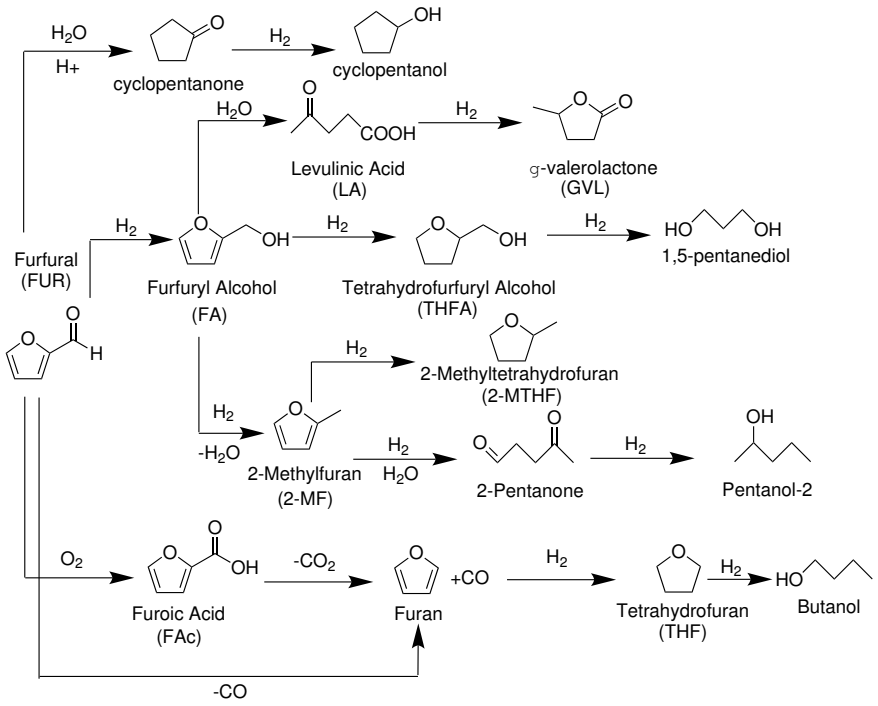

Source: Adapted from Mariscal *et al.* (2016) and Chen *et al.* (2018).

3.2.2 General Mechanisms (Classic Approach – External H_2 gas)

The use of H_2 gas as hydrogen source is used for FA production since the first patents [(Peters Jr, 1937), (Swadesh, 1956), (Adkins and Connor, 1937)]. This increases its solubility in FUR, providing excess of reactant. Generally, the pressures are higher for liquid phase reactions – from 20 to 50 bar, due to resistance of mass transfer. The elevated pressures favor a LHHW mechanism which provides a cleavage of H-H bond and an adsorption of furfural molecule at the metallic sites, promoting then an activation of C=O bond (as described in Figure 3.9.

Regarding to the adsorption of FUR into metallic sites, it is necessary to provide a high selectivity in C=O activation. If not, the ring opening can generate a large spectra of products [(Mariscal *et al.*, 2016), (Chen *et al.*, 2018)].

Figure 3.9: Proposed LHHW approach for FA production in liquid phase.

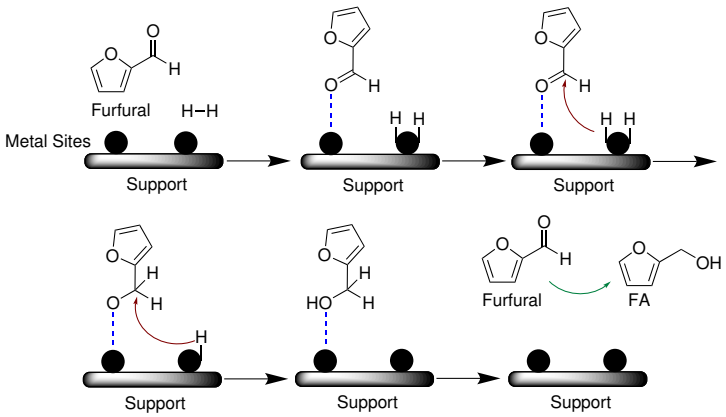

Source: Adapted from Sharma *et al.* (2013) and Chen *et al.* (2016).

3.2.3 Solvent - Water

The water medium provides high activity to furfural hydrogenation, even when compared to most common alcohols and hydrocarbons. However, one of the disadvantages over water medium is the possibility of cyclopentanone (CPO) production, as reported by many articles in literature According to Hronec and Fulajtarová (2012), the presence of an electrophilic intermediate suggests that CPO production takes place over water. Also, the metallic sites promote the conversion of FA to intermediates, cyclopentanol, and then, CPO (Hronec *et al.*, 2012), as stated in in Figure 3.10. Besides, regarding to other products, the BAS in catalysts and water provide the FA conversion to LA and GVL in water, as reported by Ennaert *et al.* (2016).

Figure 3.10: Possible reaction path from FUR to CPO in water.

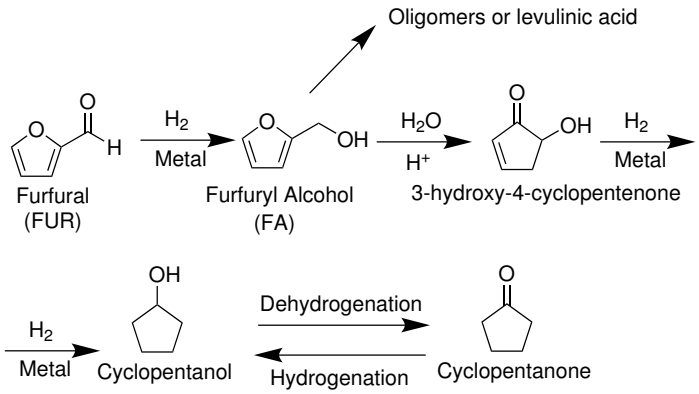

Source: Adapted from Hronec and Fulajtarová (2012)

3.2.4 Nature of Metals

The literature reported about six different metals for FUR hydrogenation: Ni, Pd, Cu, Pt, Co and Ru. Furthermore, before exploring each class of metal, several trends on FUR hydrogenation were summarized.

According to Liu *et al.* (2014), there are different configurations for the FUR adsorption over metallic surfaces: η_1 or η_2. At Cu, Ag and RuO_2 surfaces, the adsorption of FUR usually lies on a η_1-(O)-aldehyde, in an inclined shape of oxygen on C=O bond, as designed on Figure 3.11. Especially on Cu, this adsorption mode is not active to FA production, though it reduces the hydrogenation of furan ring to THFA. On the other hand, Ni, Co, Pd and Pt have strong interaction with the furan ring in FUR, which provided an η_2-(C,O)-aldehyde adsorption mode, over C and O atoms [(Pino *et al.*, 2017), (Liu *et al.*, 2014), (Bhogeswararao and Srinivas, 2015)]. Furthermore, higher temperatures may change the η_2-(C,O) into an η_1-(C)-acyl pattern (Chen *et al.*, 2018).

Figure 3.11: Adsorption of FUR on varied surfaces.

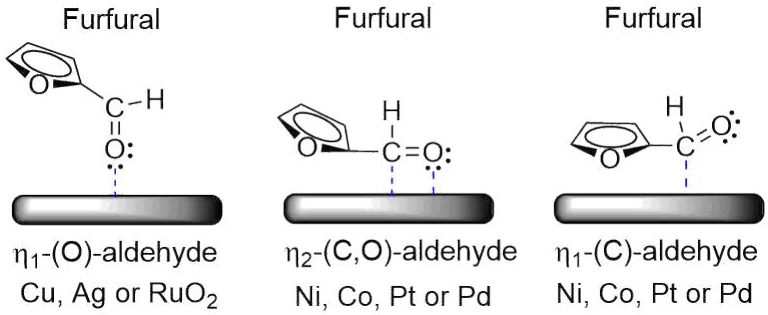

Source: Adapted from Pino *et al.* (2017) and Bhogeswararao and Srinivas (2015).

3.2.4.1 Palladium (Pd) and Platinum (Pt)

Pd and Pt are metals that provide high activity in hydrogenation reactions because of η_2-(C,O) adsorption. This might provide the total hydrogenation of FUR into FA and even the hydrogenolysis to 2-MF. The results of Pino *et al.* (2017) reported the formation of furan and tetrahydrofuran in Pd/SiO_2 catalysts in liquid furfural hydrogenation. At a similar approach, Salnikova *et al.* (2019) noted a high rate of THFA production over 5 wt% Pd/Al_2O_3 catalysts during MPV reduction in isopropanol. Therefore, the main challenge in Pd or Pt catalysts is the control of FUR selective hydrogenation.

One possible solution is the inclusion of a second metal, hence, producing a bimetallic system. The second metal should point to a higher FA selectivity and also improve the dispersion of Pd or Pt on catalytic surface. As an example, O'Driscoll *et al.* (2017) tested several metals in order to improve Pt/SiO_2 conversion: Sn, Mo, Mn, Ba, Fe and Ni. According to theire results, the only promoter that did not present increase in activity was nickel, probably due to the same mode of adsorption.

Another candidate for a second metal may be Co. The bimetallic approach was combines the synergies of Pt and Co promoted higher yields to FA. The Pt-Co/carbon catalyst (3 wt% of each metal) had 100% of FUR conversion and 100% of FA selectivity over water at 35 °C. According to Dohade and Dhepe (2017), the metallic Pt sites favored the dissociation of H_2 molecules, whereas the LAS in Co^{2+} species attracted the carbonyl group in FA, shifting the reaction network to this product, as depicted on Figure 3.12.

Figure 3.12: Mechanism of FUR hydrogenation to FA in Pt-Co/C catalysts in water solution.

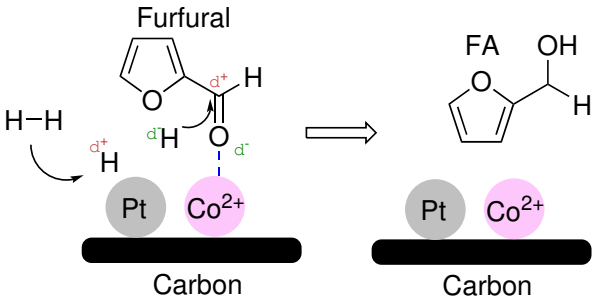

Source: Adapted from Dohade and Dhepe (2017).

3.2.4.2 Nickel (Ni)

The behavior of Ni is similar to Pd and Pt catalysts, once the adsorption of FUR in metallic sites may indicate the cleavage of furanic ring. Besides, most Ni-based catalysts induced THFA production due to non-selective FUR reduction (Chen *et al.*, 2016).

In recent works, Wang *et al.* (2018) observed that monometallic 5 wt% Ni catalysts supported on activated carbon required elevated H_2 pressures for FUR hydrogenation, because the absence of molecular hydrogen did not provide high reaction rates. Besides, when isopropanol was used as solvent (a H-donor), the monometallic Ni catalyst

produced 2-MF instead of FA. This occurred probably due to adsorption modes in the catalyst .

Another study carried out with Ni/CNT catalysts observed that higher Ni loadings not only led to a lower Ni dispersion but also to aggregations of metallic particles on surface. Then, the selectivity to FA decreased, and side products (*e.g.*, acetals and others) were more pronounced (Liu *et al.*, 2016). Besides, Biradar *et al.* (2016) related that Ni catalysts supported on basic supports (MgO) had 50% of conversion and 100% of FA yield in isopropanol. Therefore, the acid sites on supports could damage FUR reduction to formation of furfural dimers. Once again, the interactions between metal and support are crucial for FA selectivity .

3.2.4.3 Cobalt (Co)

The main challenge for the catalysts of Co is their activity for the selective hydrogenation routes. After all, those metals are very suitable for oxidation reactions instead of reduction ones. As an example, Gong *et al.* (2018b) did not detect Co metals in reduced state due to the instability of Co^0 and high degree of oxidation. Even when Co was totally reduced and Co/SiO_2 had 100% of FA yield, Audemar *et al.* (2020) suggested that the loss of activation in Co catalysts in 4th reaction cycle occurred due to poisoning and strong adsorption of carbon. Therefore, leaching is another issue on Co systems.

A successful approach was designed by Gao *et al.* (2016). A bimetallic Co-Ru supported on carbon (35 wt% and 3 wt% respectively) gave high initial rates and also 100% of selectivity to FA over benzyl alcohol as solvent. The researchers reported that the vacancies in the support made Co^{2+} species fix the carbonyl groups on FA. Therefore, the high interaction between FA and surface may promote an easier hydrogenation by the Ru0 atoms. Also, they reported that not only Co^{2+} species interact with the C=O bond, but also non reducible $Ru^{\delta+}$. Then, the electronic effect between Co and Ru decreased the furfural hydrogenation activation energy to its lower value: 58 kJ/mol at 150 °C, as reported in Table 3.3 (Gao *et al.*, 2016).

Nguyen-Huy *et al.* (2019) related the differences on CoO and Co for FUR hydrogenation to FA. Their results demonstrated that the adsorption of FUR is more pronounced on CoO, that provided an easier detachment of OH group and even hydrogenolysis of FA to 2-MF. At 180 °C, there was production of 2-MF on CoO and FA

on Co. Therefore, there is a possibility of higher activity on CoO phases.

Table 3.3: Activation energies over different bimetallic catalysts in FUR reduction to FA.

Catalyst	Apparent Activation Energy (kJ/mol)
Co-Ru/C	32.6
Ni-Ru/C	24.6
Zn-Ru/C	18.3
Mg-Ru/C	17.5

Source: Adapted from Gao *et al.* (2016).

3.2.4.4 Ruthenium (Ru)

The main advantage of Ru is the controlled rate of hydrogenation of α,β unsaturated aldehydes, once it is oxophilic. In water solvents, the literature reports the FA and furan are competitive reactions over Ru metallic particles [(Zhang *et al.*, 2017), (Durndell *et al.*, 2019), (Yang *et al.*, 2016)].

Besides, in water medium, the monometallic Ru catalysts presented loss of conversion and selectivity after several reaction cycles, as pointed out by Ramirez-Barria *et al.* (2018) and Musci *et al.* (2017). According to the literature, the main reason of deactivation in graphene oxide supported Ru catalysts is the possible irreversible chemisorption of FA in Ru metallic sites between successive runs (Ramirez-Barria *et al.*, 2018). Furthermore, concerning to the competition between hydrogenation and decarbonylation in water, Durndell *et al.* (2019) reported that Ru nanoparticles above 17 nm shifted the synthesis into FA, while smaller particles oriented the furan synthesis.

Recently Li *et al.* (2020) reported that LAS in Ru-Fe_3O_4/CNTs (carbon nano tubes) improved the FA selectivity. Compared to the Ru/CNTs, the bimetallic system increased the concentration of LAS and increased the FA yield (45% in Ru vs 81% in Ru-Fe_3O_4 in isopropanol).

There is not a major opinion about active species on FUR reduction to FA: charged $Ru^{\delta+}$ clusters or a mixture of Ru^0 and Ru^{3+} ions. However, the presence of FA resins is a major issue on those catalysts (Chen *et al.*, 2016).

3.2.5 Concluding Remarks for Furfural Hydrogenation

In this section, the general mechanisms, the supports, the metals and the influence of solvents in furfural hydrogenation to FA in liquid phase were analyzed. Furthermore, the most recent results in literature were outlined. Concerning to the metals and supports, we summarize the following topics.

- Pd, Pt and Ni provide high reaction rates for furfural hydrogenation. Furthermore, the adsorption modes of furfural into those metals establish a competition between hydrogenation of aldehyde group and decarbonylation of furfural into furan. One possible approach is the production of bimetallic or alloys catalysts with Co, Ru and others.

- Cu is selective for hydrogenation, but it lacks the amount of activity for high conversions. Also, the sintering and deposit of carbon are usual problems in copper catalysts.

- Ru, Co and Fe usually do not provide the selectivity to FA. Concerning to Co and Fe, besides the deactivation, the instability of reduced particles is another issue.

- Regarding to the acidity of catalysts, BAS are inactive for hydrogenation, but they might provide the necessary stability to the adsorption of furfural and FA, avoiding side reactions. Also, the strong LAS are a problem, especially in MPV reductions, with the formation of ethers and acetals. Besides, the basic sites might increase FA selectivity.

- Even in MPV reductions, the solvent plays an important role. Protic solvents (water, alcohols, etc.) tend to donate H^+ to furfural reduction. Although the most protic solvents increase the furfural conversion, they lack selectivity to FA. Also, the chain size of alcohols is crucial: secondary alcohols tend to be more selective – especially isopropanol. On the other hand, apolar solvents, such as hydrocarbons, curb the activity of the catalyst, due to high ability of furfural extraction.

In order to end this section, we present a resume of some articles since 2016 in FA production in liquid phase in Table 3.4.

Table 3.4: Selected works in batch liquid phase FUR reduction to FA.

Catalyst	Solvent	T (°C)	pH_2(bar)	Y_{FA} (%)	Reference
Basic Aluminas	2-Butanol	150	-	94	López-Asensio *et al.* (2018)
Pt-Sn/SiO_2	Toluene	100	20	64	O'Driscoll *et al.* (2016)
Rh/Ed-KIT-6	Formic Acid/IPA	100	-	97	Neeli *et al.* (2017)
Pt-Co/C	IPA	100	10	99.9	Dohade and Dhepe (2017)
Pd-Ag/C	Ethanol	25	1	94.1	Wu *et al.* (2020)
CuNi/MgAlO	Methanol	100	40	99.9	Wu *et al.* (2017)
Ni/MgO	IPA	170	-	50	Biradar *et al.* (2016)
Ru-Fe_3O_4/CNTs	IPA	180	-	96	Li *et al.* (2020)
Ni/AC-SO_3H	IPA	60	40	99.9	Gong *et al.* (2018a)

- : absence of gaseous H_2 (MPV reduction), IPA: isopropanol and all reactions in batch mode.

3.3 Direct Production of FA from XYL in Liquid Phase

3.3.1 First Remarks from Literature Articles and Patents

According to recent literature publications, it is possible to carry out XYL dehydration followed by FUR reduction in same reaction media – *i.e.*, the direct synthesis of FA to XYL. The first attempt of this type of conversion was detected in 2013 - results of Ordomsky *et al.* (2013a) and Ordomsky *et al.* (2013b).

Once the number of works is not so high compared to XYL dehydration or FUR hydrogenation, we believe that this is a large field in literature to report new results and discussions [(Xu *et al.*, 2020), (Canhaci *et al.*, 2017), (Perez *et al.*, 2017), (Perez and Fraga, 2014), (Cui *et al.*, 2016), (Deng *et al.*, 2020), (He *et al.*, 2017), (Hu *et al.*, 2017), (Ordomsky *et al.*, 2013a), (Ordomsky *et al.*, 2013b), (Paulino *et al.*, 2017), (Perez *et al.*, 2019)]. The detailed distribution of the articles is depicted in Figure 3.13.

Figure 3.13: Graphic of selected works of XYL to FA production since 2013.

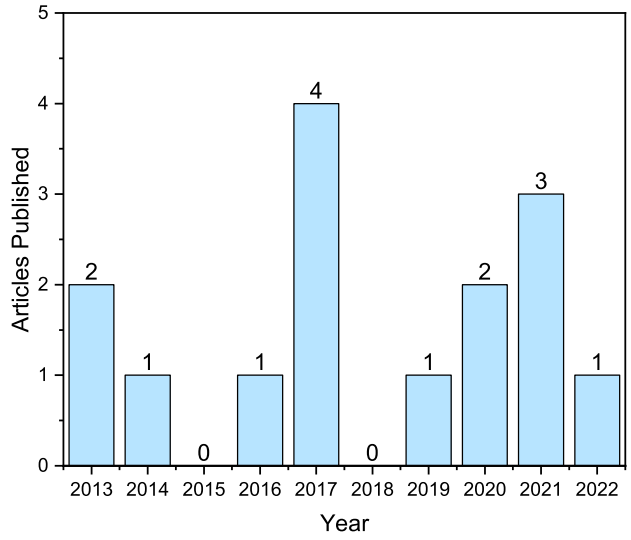

Source: Database Web of Science – search TI = (xylose and furfuryl alcohol) since 2013 to 2020. Date of search: 13/07/2022. Total of articles: 15.

Concerning to the patents, we detected only three registers in different countries: USA, Brazil and Spain [(Dumesic *et al.*, 2013), (Medoff *et al.*, 2018), (Fraga and Perez, 2015)]. This demonstrates the issues and challenges in reaching the conversion of xylose to FA in one process. However, the union of both reactions might save energy in industrial applications. In short, a resume for FA synthesis directly from XYL is provided in Figure 3.14.

Figure 3.14: Flowchart for direct conversion of XYL into FA in liquid phase.

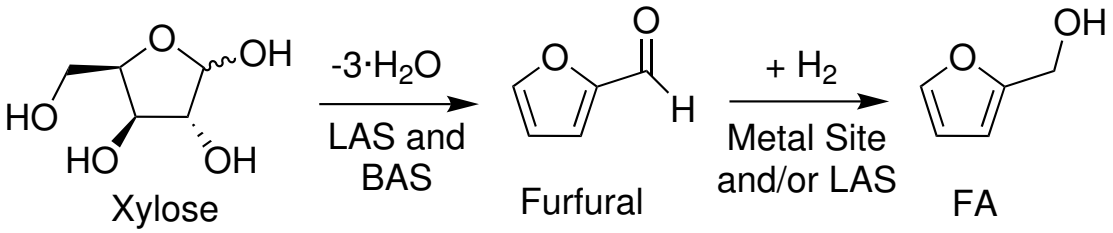

Source: Adapted from Medoff *et al.* (2018).

As our intended production has two sequence of reactions, the literature reports several ways to carry out the FA production from XYL:

1. The usual option is to carry out the dehydration in a biphasic semi-batch reaction, in order to extract FUR. Then, the hydrogenation is performed in continuous reactor

and FA is produced (Dumesic *et al.*, 2013). Some authors report the dehydration even with biological enzymes instead of solid catalysts, as Medoff *et al.* (2018) and He *et al.* (2018).

2. Development of XYL dehydration followed by FUR reduction on a flow reactor, using two different catalysts for each reaction, as reported by Cui *et al.* (2016).

3. In batch reactions, the biphasic system is also an option. In short, the pentose is dehydrated in water and an apolar phase might extract FUR for hydrogenation. In this aspect, only one catalyst can be used or two different ones, as reported by the recent results of Ordomsky *et al.* (2013a) and Ordomsky *et al.* (2013b).

4. The other proposal is the design of a multifunctional catalyst with a homogenous system, as described by recent articles [(Canhaci *et al.*, 2017), (Perez and Fraga, 2014), (Perez *et al.*, 2017), (Paulino *et al.*, 2017), (Perez *et al.*, 2019), (Xu *et al.*, 2020), (Deng *et al.*, 2020)]. In this aspect, there is energy save (due to less solvents) and reduction of costs (with only one catalyst for both operations).

In order to provide more details, a visual scheme of the four previous approaches is provided over Figure 3.15.

Figure 3.15: Alternatives to produce FA from direct conversion of XYL.

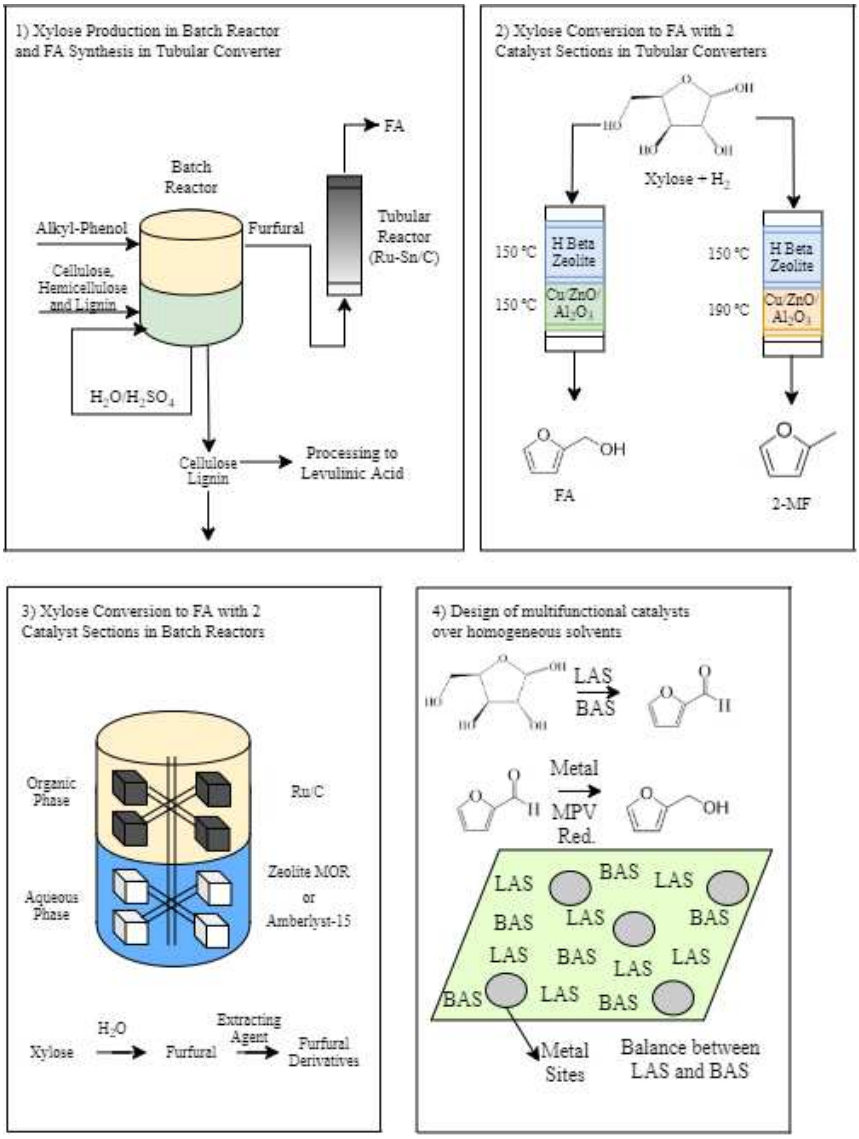

Source: Adapted from [Perez and Fraga (2014), Cui *et al.* (2016), Ordomsky *et al.* (2013a), Ordomsky *et al.* (2013b), Dumesic *et al.* (2013)].

To summarize this topic, the Figure 3.16 replies a complete reaction network for the XYL dehydration and FUR reduction to FA. First, besides the side products from FUR, the XYL molecule can be hydrogenated in metallic sites, producing xylitol (XOL). Second, even though xylitol is an important chemical to food industry, it cannot be converted to FA. And third, there is still the risk of production of condensation products from FUR and isomers of XYL.

Figure 3.16: Flowchart of the routes in the direct conversion of XYL to FA in liquid phase.

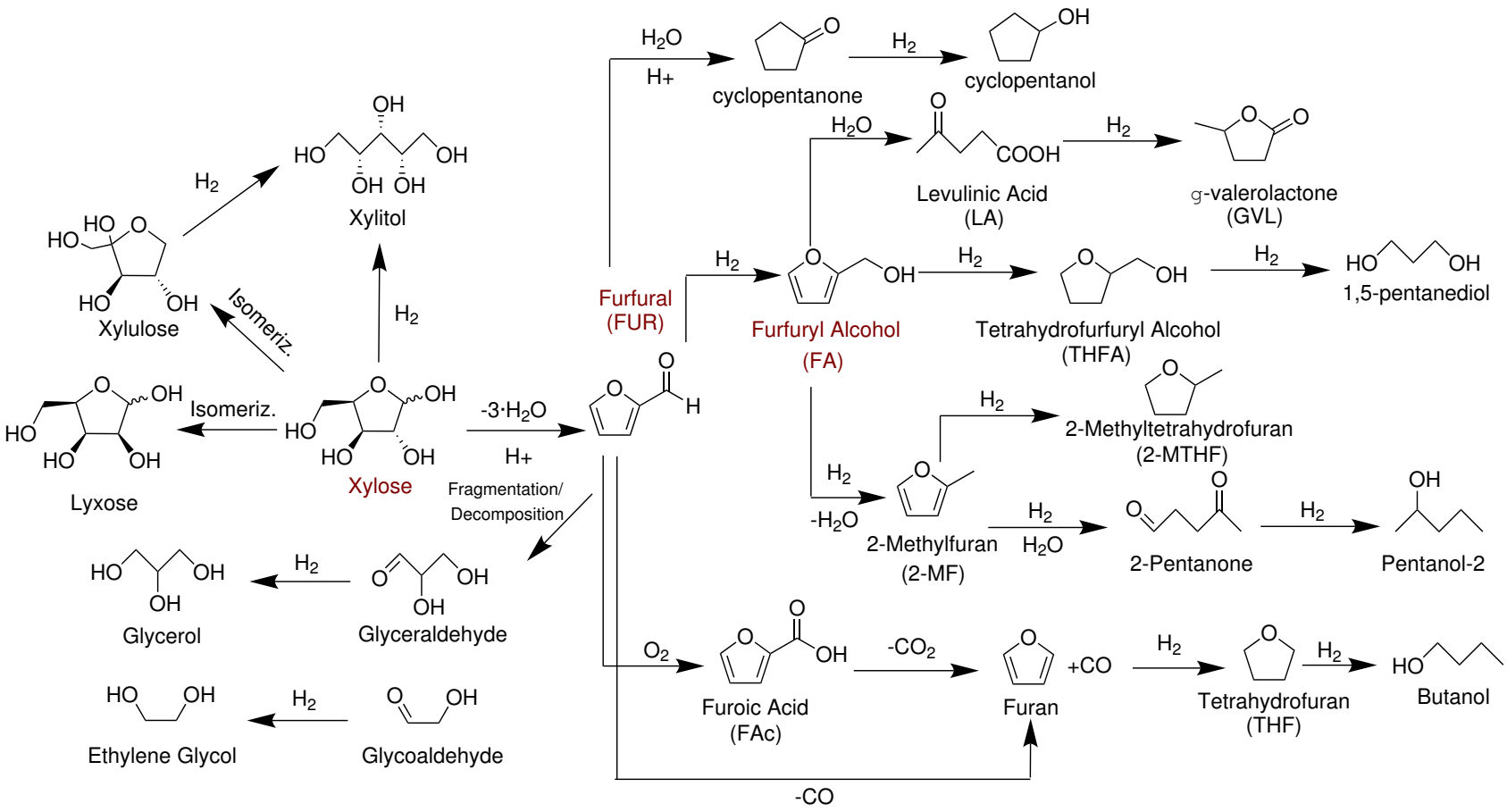

Source: Adapted from Deng *et al.* (2020), Ordomsky *et al.* (2013a), Ordomsky *et al.* (2013b).

3.3.2 Researches in Direct FA Production Since 2016

The recent literature reports several studies into liquid phase FA production from XYL. In 2013, two papers were published reporting the synthesis of FUR derivatives into a biphasic reactor with catalytic foams (3rd approach in Figure 3.15) - (Ordomsky *et al.*, 2013a) and (Ordomsky *et al.*, 2013b).

The first one reported the combined XYL dehydration and FUR reduction in monophasic (only water) or biphasic systems (water + organic phase) at 165 °C and 25 bar of H_2.

The respective catalysts were foams of Amberlyst-15 and Ru/C (Ordomsky *et al.*, 2013a). At water-monophasic system, there was 100% of XYL conversion, though a high production of XOL was reached (89% of selectivity). It was detected, then, that water was not capable to protect XYL molecule from a direct hydrogenation. Then, an organic phase for hydrogenation was tested – butanol-1, 2-MTHF or cyclohexane. As depicted in Table 3.5, despite the low activity (only 41% of XYL conversion), butanol-1 could provide some control to the hydrogenation of XYL (55% of XOL selectivity). On the other hand, 2-MTHF and cyclohexane produced higher selectivities of THFA (29% and 31%), at the same time reducing the formation of XOL. Also, the formation of levulinic acid (LA) in cyclohexane-water system denoted higher presence of FA in aqueous phase, due to a worse extraction of FA by cyclohexane.

Table 3.5: Combined XYL dehydration and FUR reduction in liquid phase (Amberlyst-15 and Ru/C at 165 °C and 25 bar H_2 pressure)

.

Solvent	X_{XYL} (%)	Selectivity to Products (%)				
		XOL	FUR	FA	THFA	LA
Water (*)	78	88.9	0	0	1.4	0
Water + 1-Butanol	41	54.9	4.6	0.8	13.9	0.9
Water + 2-MTHF	72	17.9	4.1	0	20.6	1.8
Water + Cyclohexane	67	1.0	10.4	0.8	29.0	15.3

Source: Adapted from Ordomsky *et al.* (2013a). (*) : selectivity at 78% of xylose conversion, because the complete conversion of 100% was reached.

At the second article, the combined approach was carried out over aqueous phase (Zeolite MOR as catalyst) and with water or organic solvents - 2-MTHF or cyclohexane, (4 wt% Ru/C solid catalyst). According to the researchers, the organic phase could also provide a suitable extraction of furfural and a better selectivity, avoiding side reactions. Concerning to cyclohexane as solvent, the researchers also pointed out a low rate of furfural extraction followed by its hydrogenation, once the main product at low conversions of XYL was FUR (Ordomsky *et al.*, 2013b).

Perez and Fraga (2014) used a dual catalytic system consisted of ZrO_2-SO_4 and 1 wt% Pt/SiO_2 solid catalysts. The modified zirconia had LAS and BAS for XYL dehydration, and Pt metallic sites hydrogenated furfural to FA. The liquid conversion of xylose to FA was carried out in water-isopropanol system at varied ranges of temperature and 30 bar H_2 pressure. Comparing different temperatures, the production of FUR increased, despite the formation of FA. At 150 °C, FA yield was *ca.* 24%, whereas 170 °C it was 15%. According to the researchers, higher conversions produced condensation products, decreasing FA selectivity (Perez and Fraga, 2014).

In 2017, Perez *et al.* (2017) produced a 1 wt% Pt supported on ZrO_2-SO_4 catalyst to liquid phase FA production. An important conclusion of the research was the role of metallic and acid sites in the direct conversion. The acid sites produced higher amounts of FUR while isolated metal sites converted XYL to XOL. This is reinforced at varied acid/metal ratios, as expressed in Table 3.6. The catalyst with the highest acid/metal ratio produced the highest FUR content (*ca.* 13% yield). On the other hand, the lowest acid/metal ratio produced XOL (*ca.* 5% yield) (Perez *et al.*, 2017). Therefore, the vicinity of metallic and acidic sites is an important feature of design of solid catalysts for those combined reactions, as stated in Figure 3.17.

Table 3.6: Combined XYL dehydration and FUR hydrogenation in water-isopropanol liquid phase (1 wt% Pt/ZrO_2-SO_4 at 130 °C and 30 bar H_2 pressure).

Acid/Metal Ratio	Yield (%)		
($mmol \cdot g^{-1}$/ $mmol \cdot g^{-1}$)	XOL	FUR	FA
69	6	1	13
142	2	2	13
532	2	13	12

Source: Adapted from Perez *et al.* (2017).

Figure 3.17: Acid and metal sites in Pt/ZrO_2-SO_4 catalysts.

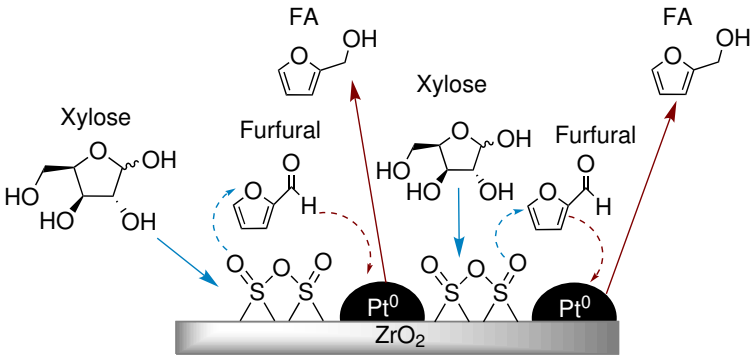

Source: Adapted from Perez *et al.* (2017).

In a similar approach, Canhaci *et al.* (2017) investigated Pt metals supported on SBA-15-SO_3H over water-isopropanol medium. They also reinforced the hypothesis of vicinal acid and metallic sites for an effective FA production. Most important, the researchers pointed out that the BAS in the catalyst system deactivated due to leaching of sulfur after three reaction cycles, even though the SO_3H groups had covalent bonds to silica. Therefore, the stability of the multifunctional catalyst is an issue crucial for this synthesis.

Deng *et al.* (2020) studied the functionalization of supports. The cascade reactions were carried out in water/butanol-1 medium using varied Cu/SBA-15-SO_3H catalysts. The study could draw several conclusions: the effect of acidity, pore sizes and solvents in direct FA synthesis. Concerning to acidity (Table 3.7), an excess of sulfur loading – 1.33 mmol/g decreased the production of FA and raised the formation of xylulose, an intermediate. On the contrary, the lowest SO_3H content – 0.75 mmol/g

provided the formation of XOL, due to the availability of metal sites. Therefore, the content of acid and metallic centers must be balance, in agreement with other studies [(Canhaci *et al.*, 2017), (Perez *et al.*, 2017)]. In Table 3.8, it was noted that an elevated pore size (12 nm) increased the activity of the catalyst, though decreasing the FA selectivity. Besides, the larger pores increased the diffusion of several molecules, reducing the carbon balance. In the final analysis, the reaction was carried out with water, water/toluene, water/isopropanol and water/n-butanol. According to the authors, an excess of water increased the formation of isomerized products – xylulose and also the polycondensation of furfural, which curbed the carbon balance.

Table 3.7: Effect of acidity over Cu/SBA-15-SO_3H catalysts in direct FA production from XYL.

S content (mmol/g)	Acidity (mmol/g)	Acid/Metal Molar Ratio	X_{XYL} (%)	Selectivities (%)		
				XOL	Xylulose	FA
0.75	0.59	0.26	87.4	23	1	57
1.12	0.98	0.40	93.7	14	8	63
1.33	1.25	0.49	95.1	9	15	49

Source: Adapted from Deng *et al.* (2020). Reaction conditions: 130 °C, 30 bar H_2 pressures in 10 mL water/n-butanol (1:3 volume ratio).

Table 3.8: Effect of pore sizes over Cu/SBA-15-SO_3H catalysts in direct FA production from XYL.

Mean pore size (nm)	Acid/Metal Molar Ratio	X_{XYL} (%)	Carbon Balance (%)	Selectivities (%)		
				XOL	Xylulose	FA
4	0.40	93.7	92	7	11	63
7	0.39	94.8	84	10	12	51
12	0.40	95.1	77	12	11	43

Source: Adapted from Deng *et al.* (2020). Reaction conditions: 130 °C, 30 bar H_2 pressures in 10 mL water/n-butanol (1:3 volume ratio).

On the other hand, an apolar solvent, such as toluene, inhibited the formation of XOL and FA, due to the higher extraction of FUR. Therefore, an excess of interaction

between FUR and the organic solvent can lower the hydrogenation route. In the case of isopropanol and n-butanol, the first alcohol presented higher formation of XOL (20% vs 10%). To explain this, the researchers established that the excess of interaction between hydrogen bonds in isopropanol and the C=O bonds increased the formation of XOL and xylulose (Deng *et al.*, 2020).

Deng *et al.* (2020) studied the N-doped carbon that contained confined Co particles. According to the study, 1,4-dioxane, a less polar substance, was the optimum solvent used with water because it prevented condensation and degradation reactions in organic phase. At 160 °C and with absence of H_2, the FA yield reached 70% with formic acid as donor. Compared to the other hydrogen donors, such as ethanol and methanol, the formic acid presented the necessary amount of hydrogen for the reaction (Table 3.9). Nonetheless, the alcohols presented a high interaction with XYL and FUR because of polarity (Xu *et al.*, 2020).

Table 3.9: Effect of H-donor over Co-N-C catalysts in direct FA production from XYL.

H donor	X_{XYL} (%)	Yield (%)		
		XOL	Xylulose	FA
Formic Acid	99.9	3.8	1.1	69.5
Methanol	58.1	0	4.1	0
Ethanol	32.0	0	3.9	0
Isopropanol	59.1	0	4.2	0
Gaseous H2	83.1	0	3.8	0

Source: Adapted from Xu *et al.* (2020). Reaction conditions: 160 °C, 5 bar N_2 pressures in water/1,4-dioxane.

The absence of hydrogen gas as H-donor was also reported by Paulino *et al.* (2017). The group carried out the XYL dehydration followed by a MPV reduction of FUR to FA. Three types of zeolites were used: beta, USY and ZSM-5. First, the USY zeolite presented the lowest selectivity to FA (13%), due to the hydrophilic feature of this material. This was also evidenced by the formation of side-products, such as glyceraldehyde. On the other hand, ZSM-5 zeolite presented narrowed pores providing issues to FA formation (43% of selectivity) and higher xylulose selectivity (30%). Finally, the hydrophobicity

of zeolite beta preserved the activity and the selectivity during the reaction, leading to *ca.* 90% of xylose conversion and 75% of FA selectivity. Then, zeolite beta was the most suitable catalyst for synthesis (Paulino *et al.*, 2017). Perez *et al.* (2019) highlighted the vicinity of LAS and BAS sites as a major factor for suitable FA conversion. Also, a minor deactivation of LAS was noted due to adsorption of FUR intermediates along the cycles (Perez *et al.*, 2019).

Cui *et al.* (2016) used a continuous reactor for direct FA synthesis – as depicted in 2) in Figure 3.15. Instead of the usual biphasic approach, the conversion was carried out with two separated catalysts in a monophasic system (water + γ-butyrolacone). The Hβ zeolite promoted XYL dehydration, whereas the Cu based catalyst ($CuO/ZnO/Al_2O_3$) reduced FUR to its derivatives. Despite the total XYL conversion of 100%, the authors observed that minor temperature variation in Cu-based catalyst bed led to different products: 150 °C (FA) and 190 °C (2-MF). Then, the higher temperatures promoted the hydrogenolysis of FA into 2-MF, as expressed in Table 16. In addition, the authors pointed out the formation of carbon deposits in Hβ zeolite after 120 hours of reaction, probably due to the formation of humins in catalyst. However, the zeolite could be re-activated after exposure to air-flow.

Table 3.10: Direct conversion of xylose to FA and 2-MF in continuous reactor at different temperatures (5 wt% xylose, 20 wt% water and 75 wt% γ-butyrolacone).

Hβ to Cu catalyst ratio (g/g)	T (°C)	X_{XYL} (%)	Yield (%)			
			FUR	FA	2-MF	GVL
2.5	150	100	26.5	59.3	0.4	0.2
2.0	150	100	18.9	68.1	0.6	0.4
1.0	150	100	0.2	87.2	1.1	1.5
0.5	150	100	0	86.9	1.5	2.6
1.0	170*	100	0	40.6	45.2	1.2
1.0	180*	100	0	19.3	68.5	2.6
1.0	190*	100	0	0.1	86.8	1.9

Source: Adapted from Cui *et al.* (2016). H_2 pressure: 1 bar; *: temperature of second catalyst bed, the temperature of first bed was always 150 °C.

3.3.3 Concluding Remarks for FA Production in Liquid Phase from Xylose

Regarding to the reported articles, some conclusions may be explained:

- The challenge for a multifunctional catalyst relies on the optimal combination of metallic sites and LAS/BAS sites. To achieve this, the most common approach is the functionalization of the support with BAS and the loading of an active metal. However, the deactivation and leaching of the anchored sites is also an issue.

- For some catalytic systems, the excess of interaction of isopropanol formed isomers of XYL (xylulose and lyxose) during the conversion. Therefore, an optimum solvent should extract the FUR and FA from aqueous phase, at the same time allowing the H_2 to solubilize.

- The control of acidity and pore sizes is also important for the prevention of undesired reactions and the direct formation of FA from xylose. Larger pores may produce undesired side products.

- The temperatures close to 200 °C promote the formation of 2-MF, *i.e.*, the hydrogenolysis of FA. On the other hand, temperatures at 100 °C decrease the formation of FUR side products, but curb the XYL dehydration. Therefore, intermediate values are preferred.

Chapter 4

Methodology

In this section we explain the main topics of our experimental methods, like: the preparation of the catalysts, the characterization techniques and also the procedure for reactions.

4.1 Selected Supports and Catalysts

Eight solids were chosen based on two modified supports: calcined niobium oxide and phosphated niobia. The original support was the niobic acid (NB) $Nb_2O_5 \cdot nH_2O$ - Niobia HY340 - CBMM. This oxide was used in XYL dehydration and FUR reduction, as reported by the works of Moura (2019), de Lima (2020) and Costa (2021). The calcined Nb_2O_5 support (NB400) was pretreated over calcination at 400 °C during 4 h on synthetic air to maintain low crystalliniy. Literature research reported the first events of crystalline transition to hexagonal phase around 500 °C [(Nowak and Ziolek, 1999), (Mejía *et al.*, 2017)]. For the phosphated support, first the NB400 support was incorporated into a H_3PO_4 treatment (Okazaki and Wada, 1993). After this modification, the same calcination was carried out to provide desorption of weak P groups on surface (de Lima, 2020), producing the NBAc400 support.

Regarding to the metals, three components were researched: cobalt (Co), nickel (Ni) and ruthenium (Ru). Co oxides presented elevated activity for FUR reduction compared to metal Co (Nguyen-Huy *et al.*, 2019). Ni particles have strong adsorption of aldehyde groups, which may increase FA formation (Chen *et al.*, 2018). Finally, despite the oxophilic feature, metal Ru sites can provide activity for hydrogenation routes (Aldosari *et al.*, 2016). The metal active phase was incorporated with chlorine precursors on NB400 and NBAc400 supports using the incipient wetness impregnation methodology (IWI) (Ertl *et al.*, 2008). Cobalt and nickel loadings were 10 wt%, due to their lower activity, whereas the intened Ru content had 5 wt% of content in both supports.

Prior to the reaction, the metal catalysts were activated *ex-situ* by reduction under H_2 flow on a tube at 400 °C during 2 h. For the metal M with X loading supported on NB400, the name was MNBX and MNBAcX on NBAc400, as stated on the Table 4.1.

For instance, a decision flowchart is provided on Figure 4.1. The subsections 4.1.1 to 4.1.4 will provide further details about the methodology.

Table 4.1: Nomenclature of the solids in the research.

Solid Description	Nomenclature	Solid Description	Nomenclature
Acid Niobia Support ($Nb_2O_5 \cdot nH_2O$)	NB400	Acid Niobia Support treated with H_3PO_4 ($Nb_2O_5 \cdot nH_2O$-H_3PO_4)	NBAc400
10 wt% Co/Nb_2O_5	CoNB10	10 wt% Co/Nb_2O_5-H_3PO_4	CoNBAc10
10 wt% Ni/Nb_2O_5	NiNB10	10 wt% Ni/Nb_2O_5-H_3PO_4	NiNBAc10
5 wt% Ru/Nb_2O_5	RuNB05	5 wt% Ru/Nb_2O_5-H_3PO_4	RuNBAc05

Figure 4.1: Concise flowchart for the preparation and activation of catalysts.

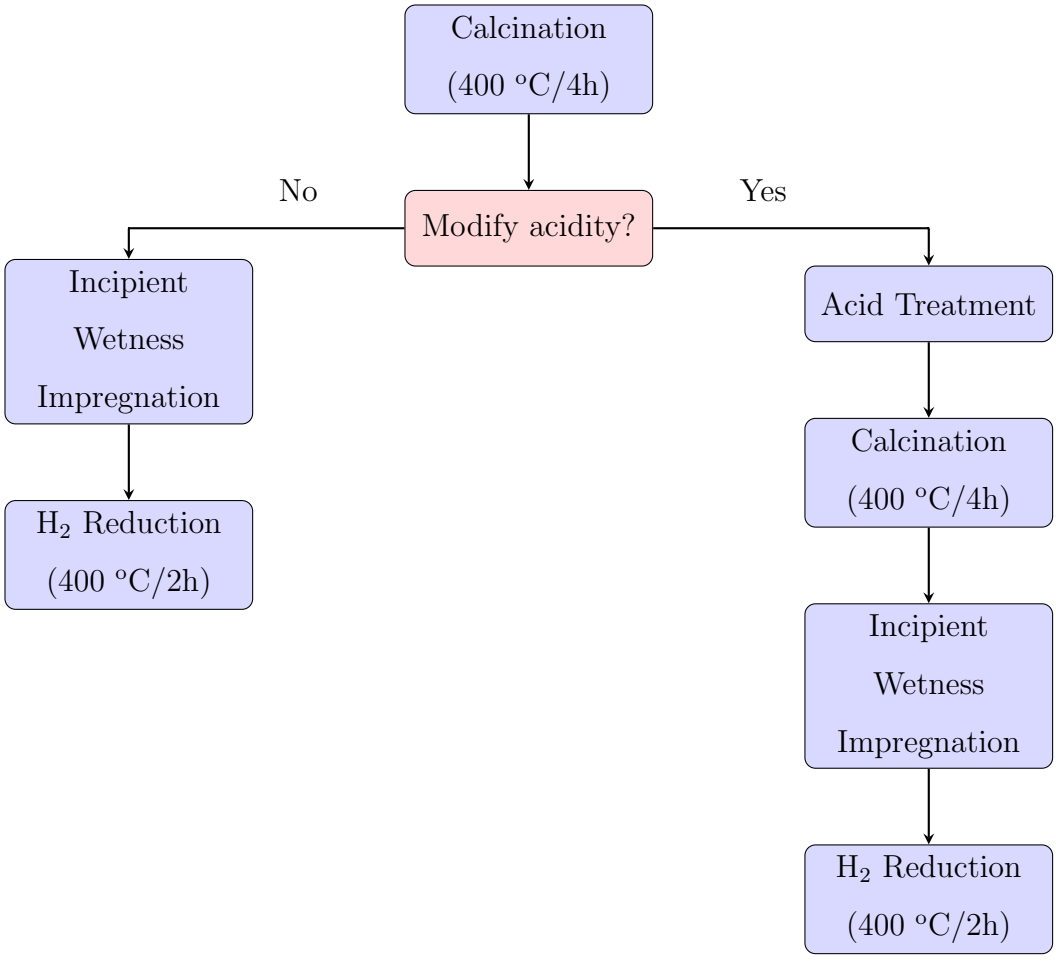

4.1.1 Calcination of the Supports

The pretreatment of the catalyst provides the suitable amount of thermal resistance and stability for the next stages (Ertl *et al.*, 2008). A decrement of specific area is undesirable on supports NB400 and NBAc400, then the temperature for pretreament was set as 400 °C during 4 h in a 10 °C/min heating rate in a quartz cell. The flow of synthetic air was set to 80 mL/min during the experiments. After the calcination step for the niobic acid (NB), the support NB400 was obtained. Also, this stage was repeated to provide desorption of weak phosphate groups after the acid treatment, producing then the NBAc400 support.

Table 4.2: Experimental for calcination of NB into NB400 and NBAc400 supports.

Parameter	Value
Synthetic Air Flow (mL/min)	80
Temperature (°C)	400
Heating rate (°C/min)	10
Time (h)	4.0
Nb_2O_5 sample (g)	10

4.1.2 Acid Treatment

In order to increase the acidity and to insert new acid groups, it was also possible to carry out an acid treatment with phosphoric acid. That was performed according to adaptations on the procedures described by Okazaki and Wada (1993). The H_3PO_4-treatment was based on the immersion of the previously calcined niobic acid (NB400) into a 1 mol/L aqueous solution of H_3PO_4 on a beaker. Furthermore, the ratio between acid solution and solid mass was 30 mL of acid per 10 g of niobium oxide. Then, this suspension was mixed with a magnetic stirrer during 48 h at room temperature to improve the contact between phosphoric acid and niobia.

After the exposure time, the temperature of the stirrer was raised to evaporate higher amounts of liquid for about 5 min. During the evaporation, the niobia suspension was transformed into a humid precipitate. As a final stage, that residual solid was inserted

into an oven during 24 h at 110 °C in order to evaporate remaining liquids. Finally, the sample was crushed with a pestle on a mortar before storage.

During the experiments, it was not possible to insert phosphate on mass superior than 20 g due to issues in mass transfer. Therefore, the synthesis of the support NBAc400 was carried out in several batches, and the final NBAc400 solid was a mixture of them.

4.1.3 Incipient Wetness Impregnation (IWI)

Due to elevated solubility, the precursors of the active phases on NB400 and NBAc400 supports were chlorides (99.9% purity - Sigma Aldrich Chemical Co). The metals (Co, Ni and Ru) were inserted on both supports according to the Incipient Wetness Impregnation (IWI) procedure, as described by Ertl *et al.* (2008).

Before to the IWI, the incipient volume for NB400 and NBAc400 supports was determined experimentally. A fixed volume of deionized water was added to *ca.* 2 g of each support, initially producing a paste. When the paste turned into a suspension, the previous volume was noted. That value might indicate the maximum amount of water (or solution) to promote the cappilary action into the catalyst pores during the IWI (de Jong, 2009). The Table 4.3 below indicated the experimental values of the incipient volume for NB400 and NBAc400 supports.

Table 4.3: Mean experimental values of incipient volumes - NB400 and NBAc400 supports.

Support	Incipient Volume (cm^3/g)
NB400	1.20
NBAc400	0.90

The necessary amount of chloride precursor to produce 10% (Co and Ni) or 5% (Ru) was added to deionized water on a graduated cylinder. Next, the solution was added slowly to the support on a mortar with an automatic pipette. After each drop of dissolved precursor, the system was mixed with a mortar. Next, after all the solution was put in contact with NB400 or NBAc400 support, the system remained during 12 h on the bench to promote the diffusion of the metal into the pores of the support. Also, to

evaporate minor contents of liquid, the solid was dried in an oven at 75 °C during 24 h. Finally, the solid was crushed to be put in the desiccator. The Table 4.4 provided more details of IWI procedure.

It is important to mention that only 2-3 g of the catalyst could be mixed on the mortar. Therefore, the catalysts CoNB10, CoNBAc10, NiNB10, NiNBAc10, RuNB05 and RuNBAc05 were synthesized after successive IWI procedures. Except for the supports NB400 and NBAc400, the catalysts were activated under H_2 flow. Once no reducing agent was used during IWI methodology, those *ex-situ* reductions were carried out under H_2 flow.

Table 4.4: Precursors and metal contents selected for IWI methodology.

Precursor	Catalyst	Active Metal Loading (wt%)
$CoCl_2{\cdot}6H_2O$	CoNB10 and CoNBAc10	10%
$NiCl_2{\cdot}6H_2O$	NiNB10 and NiNBAc10	10%
$RuCl_3{\cdot}xH_2O$	RuNB05 and RuNBAc05	5%

x=1.37 for ruthenium chloride was previously determined by Nascimento (2018).

4.1.4 Catalyst activation under H_2 flow - Co, Ni and Ru

The *ex situ* reduction conditions are expressed in Table 4.5. During those experiments, around 1.5 g of non-activated catalyst was loaded into the furnace and the quartz wool under an H_2 flow of 60 mL/min. The furnace had been heated up to 400 °C during 2 h over a 10 °C/min rate. During the cooling of the furnace to the room temperature, an argon flow of 60 mL/min was set to carry out the remaining hydrogen.

Table 4.5: Parameters for the *ex situ* activation of metallic catalysts (Co, Ni and Ru).

Parameter	Value	Parameter	Value
H_2 Flow (mL/min)	60	Heating rate (°C/min)	10
Ar Flow (mL/min)	60	Time (h)	2.0
Temperature (°C)	400	Sample amount (g)	1.5

It should be addressed that Ru chlorides calcinated at higher temperatures

might produce oxides and oxychlorides species. Mazzieri *et al.* (2003) cited that the calcination of $RuCl_3$ resulted on less mobile Ru particles, which could create issues to reduction. Indeed, even after a similar H_2 reduction at 400 °C, the Ru/Al_2O_3, the total removal of Cl as not possible, according to Mazzieri *et al.* (2003). Therefore, we decided not to carry out a calcination step before the H_2 activation.

4.2 Catalyst Characterization

The characterization of the solids in this study is important for the comprehension of the interactions between the active phase and the supports. The Table 4.6 described the objectives of the techniques performed.

Table 4.6: Physical-chemical and acid properties characterizations.

Characterization	Abbreviation	Main information of the procedure
X-Ray Diffraction	XRD	Investigation about the crystalline phases of the support and catalyst
N_2 Adsorption at 77 K	-	Investigation of the textural properties of solids
Scanning Electron Microscopy + Energy-Dispersive X-Ray Spectroscopy	SEM/EDX	Analysis of morphology and chemical composition of solids
Activation under H_2 Flow	H_2-TPR	Determination of degree of reduction in catalysts
X-Ray Photoelectron Spectroscopy	XPS	Chemical analysis of catalyst surfaces
NH_3 Temperature-Programmed Desorption	NH_3-TPD	Determination of the total acidity in sample

4.2.1 X-Ray Diffraction (XRD)

The XRD analysis is used to investigate the crystallinity of the samples, according to the degree of crystallization and the amount of phases available on catalyst (Lowell *et al.*, 2012). For crystalline events, the crystallite size can also be calculated

according to the Scherrer's equation (Equation 4.1). However, for a more precise approach on particle size, the XRD diffraction pattern does not provide reliable results compared to other experiments like TEM - Transmission Electron Microscopy. Therefore, the results of Equation 4.1 provided estimations of crystalline domain sizes.

$$\tau = \frac{K \cdot \lambda}{\beta \cdot cos(\theta)} \tag{4.1}$$

In the equation 4.1, τ is the mean domain size [m], K is a shape factor [no unit], λ is the X-ray wavelength [m], β is the FWHM, or the line size at the half of maximum intensity [rad] and θ is the Bragg angle [rad]. All the experiments in XRD were carried out at LRAC (Laboratório de Recursos Analíticos e Calibração), with the specifications expressed in Table 4.7.

Table 4.7: Equipment specifications and parameters in XRD analysis.

Information	Description
Equipment brand	Philips Analytical X Ray
Equipment model	X Pert-MPD
Equipment database	PANalytical database version number: 2.1002
Type of radiation	Cu-Kα with λ=1.54056 Å

All the eight solids were analyzed on XRD. The supports NB400 and NBAc400 were calcined at synthetic air during 4 h and 400 °C.The metal solids were previously activated under H_2 low for 2 h and 400 °C.

4.2.2 N_2 Adsorption at 77 K

The gas adsorption manometry is the principle generally used for the determination of adsorption isotherms of N_2 at the temperature of liquid state (*ca.* -196 °C or 77 K). During the procedure, the solid samples were pretreated by applying a combination of heat, vacuum, and/or flowing gas to remove adsorbed contaminants acquired from atmosphere (typically H_2O and CO_2). The solid was then cooled, under vacuum, usually to cryogenic temperature (77 K or -196 °C). Nitrogen was dosed to the solid in controlled increments. After each dose of adsorptive, the pressure is allowed to equilibrate

and the quantity adsorbed is calculated (Lowell *et al.*, 2012). The specifications for the experiments with N_2 adsorption are summarized in Table 4.8.

Table 4.8: Information during the experiments of N_2 adsorption using BET model.

Information	Description
Equipment	Micrometrics Tristar Model ASAP 2010 Chem.
Saturation Pressure [mmHg]	710
Relative Pressure (p/p_o) Range [-]	0.01-0.98
Adsorption Temperature [K]	77
Desorption Temperature [K]	77

4.2.3 SEM/EDX

SEM can provide details about the morphology of the catalyst, the EDX can determine the elementary chemical composition. The EDX spectra does not set a reliable quantitative number compared to other techniques like Inductively Coupled Plasma-Atomic Emission Spectrometry (ICP). Therefore, regarding to EDX percentages, all the results are semi-quantitative. During the preparation of samples for SEM, the material mixed to a golden analyzer to obtain a film of *ca.* 200 Å. Therefore, inside the equipment, after an electron beam hit the samples, the secondary low energy electrons produced a surface image. Besides, the X-ray emissions are used to compute EDX results. The equipment and the conditions of the SEM/EDX analyses are given in Table 4.9.

Table 4.9: Information during the experiments of SEM/EDX.

Information	Description
Equipment	Sputter Coater EMITECH, Model: K450
SEM/EDX Model	Leo 440i/6070
Brand SEM/EDX	LEO Electron Microscopy/Oxford
Golden film thickness [Å]	200

Only metal catalysts were analyzed in SEM/EDX. The Co, Ni and Ru based solids were previously activated under H_2 low for 2 h and 400 °C.

4.2.4 H_2 - TPR

The TPR analysis was important to detect the formation of active phases of Co, Ni and Ru catalysts. Those experiments were carried out at Laboratório para Estudos de Processos de Adsorção e Catálise (LEPAC) at University of Campinas. The equipment used during the experiments was a Micromeritics AutoChem II 2920. First, about 0.2 g of solid was loaded into the reaction system. After that, a mixture of 10% of H_2 into He was inserted on a flow of 50 mL/min and a TCD detector stored the signal.

Due to the elevated Cl contents of the precursors, the TPR experiemnts were different from the catalyst activation. Before H_2-TPR, the calcination of samples was carried out to remove Cl during 2 h at 400 °C. Then, this additional stage could decrease Cl content on samples. A summary of the experimental conditions for TPR studies is provided in Table 4.10.

Table 4.10: Equipment specifications and parameters in H_2-TPR experiments - CoNB10, CoNBAc10, NiNB10, NiNBAc10, RuNB05 and RuNBAc05 solids.

Information	Description
Equipment model	Micromeritics AutoChem II 2920
Gas mixture	10% H_2 in He
Gas flow [mL/min]	50
Final Temperature [°C]	300 - Ru
Final Temperature [°C]	800 - Co and Ni
Heating rate [°C/min]	10
Sample mass [g]	0.20

4.2.5 X-Ray Photoelectron Spectroscopy (XPS)

The XPS analysis is important to provide the species and oxidation states on catalyst surface. The X-ray Photoelectron Spectroscopy (XPS) experiments were carried out at LAB (Laboratório Avançado de Baterias) at Unicamp. The used equipment was a multichannel hemispheric analyzer Thermo-Alpha. During the experiments, the pressure on vacuum chamber was reduced to $2 \cdot 10^{-7}$ Pa, in order to maintain the flow of radiation.

Besides, the radiation used had 1486.6 eV on a Al Ka micro-focused monochromator and the survey spectra were performed under a step of 20 eV. For peak fitting, the software XPSPEAK41 was used. The Table 4.11 provided more details of analysis.

Table 4.11: Equipment parameters in XPS experiments.

Information	Description
Equipment model	Thermo-Alpha multichannel hemispheric analyzer
Pressure [Pa]	$2 \cdot 10^{-7}$
Radiation [eV]	1486.6 Al-Kα

All the eight solids were analyzed on XPS. Conversely with Section 4.1.1, the supports NB400 and NBAc400 were calcined at synthetic air during 4 h and 400 °C. In turn, the metal solids (CoNB10, CoNBAc10, NiNB10, NiNBAc10, RuNB05 and RuNBAc05) were previously activated under H_2 low for 2 h and 400 °C.

4.2.6 NH_3-TPD

The NH_3-TPD experiments were carried out at Laboratório para Estudos de Processos de Adsorção e Catálise (LEPAC) at University of Campinas. Initially, about 0.2 g of samples were pretreated under He at 300 °C (increment of 10 °C/min and flow rate of 25 mL/min). Then, the samples were cooled to about 50 °C and subjected to ammonia flow (25 mL/min) during 30 min. After, the ammonia was removed by purging the system for 30 min under He flow. At the last step, the desorption was carried out under He flow up to 500 °C with heating rate of 10 °C/min and it was observed using a thermal conductivity detector (TCD). A summary of the experimental conditions is provided in Table 4.12.

Conversely to XPS conditions, the supports NB400 and NBAc400 were calcined before the analysis, and the metal catalysts Co, Ni and Ru were activated on hydrogen prior to the experiments.

Table 4.12: Equipment specifications and parameters in TPD experiments.

Information	Description	Information	Description
Equipment	Micromeritics AutoChemII 2920	Amount [g]	0.20
Pretreatment temperature [°C]	300	Cooling temperature [°C]	50
Pretreatment and desorption ramp [°C/min]	10	He flow rate - pretreatment [mL/min]	25
NH_3 flow rate - saturation [mL/min]	25	Final desorption temperature [°C]	500

4.3 Batch Reactions

For the XYL conversion into varied products, the reactions were carried out in a Parr converter. Our solids were tested during 6 h, at 160 °C and 50 bar H_2 pressure. Prior to the reaction stage, 0.8 g of catalyst were mixed with 160 g of deionized water in a batch Parr converter at room temperature. Next, the temperature of reactor was increased to the setpoint (160 °C), while the vessel pressure was raised to 35 bar. After a stabilization on temperature, the XYL aqueous solution was inserted into the reactor into a feed input and the pressure was equalized to 50 bar. Then, this moment was taken as the beginning of reaction.

During our procedure, 12 points were taken to identification of components. The time step was 15, 30 or 60 min each. In fact, the time of the samples were 0, 15, 30, 45, 60, 90, 120, 150, 180, 240 and 360 min of reaction. After the final point, the liquid was filtered and the catalyst was let in an oven during 24 h and 120 °C. No reuse of solids was performed.

For our reactions, the supports NB400 and NBAc400 and the metal catalysts CoNB10, CoNBAc10, NiNB10, NiNBAc10, RuNB05 and RuNBAc05 were tested. Besides, the supports were activated 24 h before the reaction (400 °C/4 h at 80 mL/min synthetic air) as well as the metal solids (400 °C/2 h at 60 mL/min H_2 flow). A summary of our experimental conditions was displayed at Table 4.13.

Table 4.13: Experimental conditions for reactions in Parr converter.

Information	Description	Information	Description
Temperature [°C]	160	Amount of catalyst [g]	0.80
H_2 pressure [bar]	50	Mass of deionized water [g]	200.0
Time [h]	6.0	XYL mass [g] / XYL concentration (g/g of aq. solution)	4.0 / 20.0

OBS: No reuse of any solid was carried out (only 1 reaction cycle.)

4.4 Identification of the Products

As stated on Section 3, the XYL reaction paths may produce different types of isomers, including pentoses and other sugars. In addition, the samples could not be quantified by a typical GC (Gas Chromatography), unless without any technique to convert residual sugars into volatile compounds, like sylanization. Then, an HPLC (High Performance Liquid Chromatography) analysis was used to provide the identification of the products based on the corresponding peaks of the patterns. All the experiments in HPLC were carried out at Laboratório de Equipamentos Cromatográficos (LEC) at the University of Campinas.

Before the identification in the equipment, all the samples were filtered at room temperature in order to remove remained solids. As reported in Table 4.14, the compounds were studied in a HPLC model Water 717 plus Autosamples with a Waters 410 Diferential Refractometer detector. For the separation of the components, the Biorad Aminex HPX-87H ion-exchange column was used at 65 °C with a mobile phase of a $5 \cdot 10^{-3}$ mol/L H_2SO_4 aqueous solution. Finally, the flow of mobile phase was 0.7 mL/min and the time of each run was 45 min.

Calibration curves were taken to calculate the concentration of the compounds [mol/kg of solution]. As XYL is the starting compound and no xylulose was identified, the conversion X_{PEN} was defined at Equation 4.2. The information of selectivity (S_i) and yield (Y_i) for other substances i was disposed in Equations 4.3 and 4.4.

In the Equation 4.2 to 4.4, $C_{XYL_{t=0}}$ is the XYL concentration in the first point of reaction [mol/kg], C_{XYL} is the XYL concentration at any time t of the reaction [mol/kg], $C_{i_{t=0}}$ is the concentration of i substance at the begin of reaction [mol/kg] and C_i is the concentration of i-substance at any point [mol/kg].

Table 4.14: Experimental conditions for analyses at HPLC.

Information	Description
Equipment model	Water 717 plus Autosamples
Ion-exchange column	Biorad Aminex HPX-87H
Temperature of the column [°C]	65
Mobile phase	5 mmol/L solution of H_2SO_4
Mobile phase flow [mL/min]	0.7
Time for each run [min]	45.0

$$X_{PEN} = \frac{C_{XYL_{t=0}} - C_{XYL}}{C_{XYL_{t=0}}} \tag{4.2}$$

$$S_i = \frac{C_i}{C_{XYL_{t=0}} - C_{XYL}} \tag{4.3}$$

$$Y_i = \frac{C_i - C_{i_{t=0}}}{C_{XYL_{t=0}}} \tag{4.4}$$

We have also tried to identify other products from dehydration hydrogenation routes. Among them, there is xylitol (XOL), a product from direct XYL hydrogenation. Also, furfural (FUR) might be produced from XYL dehydration. Finally, another FUR derived products, like furfuryl alcohol (FA), tetrahydrofurfuryl alcohol (THFA), levulinic acid (LA), cyclopentanone (CPO) and γ-valerolactone (GVL) were studied on HPLC. To conclude, the Table 4.15 summarized all the studied compounds and retention times on HPLC experiments. It is also important to point out that GVL was not detected in any time during the reactions.

Table 4.15: Retention times for studied compounds on HPLC analyses.

Compound	Retention time (min)
Xylose (XYL)	7.9
Xylitol (XOL)	9.1
Furfuryl alcohol (FA)	10.0
Levulinic acid (LA)	13.6
Tetrahydrofurfuryl alcohol (THFA)	22.0
γ-valerolactone (GVL)	25.7
Cyclopentanone (CPO)	31.8
Furfural (FUR)	38.0

OBS: No GVL was detected on the reactions.

Marcotullio (2011) reported that the dehydration products from XYL and resinification of FUR could provide issues to identification of compounds. Once the spectra of products is varied on sugar conversions, it was important to have a measure concerning to the proposed products of Table 4.15. One of them is the carbon balance, which was provided in Equation 4.5.

$$CB = \frac{\sum_{i=1}^{N_{comp}} C_i}{C_{XYL_{t=0}}} \tag{4.5}$$

Chapter 5

Results and Discussions

In this chapter, we will provide details about the characterizations results as well as the outcomes of the batch reactions. Furthermore, the routes of identified chemical substances were also explained.

5.1 Characterizations

5.1.1 N_2 Adsorption at 77 K - Textural Properties

The Table 5.1 below collects the results at the nitrogen adsorption at 77 K. The BET model was used to calculate the specific surface area S_{BET} [m^2/g] and the BJH approach determined the mean pore volumes V_{BJH} [cm^3/g] and D_{BJH} mean pore diameters [Å].

Table 5.1: Surface area, pore diameter and pore volume in N_2 adsorption.

Catalyst	S_{BET} [m^2/g]	V_{BJH} [cm^3/g]	D_{BJH} [Å]
NB400	120	0.16	51
NBAc400	37	0.08	87
CoNB10	39	0.12	113
CoNBAc10	82	0.13	60
NiNB10	36	0.11	117
NiNBAc10	50	0.10	72
RuNB05	25	0.07	103
RuNBAc05	42	0.09	81

In both niobia supports (NB400 and NBAc400), the selected temperature of calcination (400 °C) did not provide the phase transition, in agreement with Nowak and Ziolek (1999). In fact, according to Chan *et al.* (2017), the pretreatment temperatures above 500 °C had initiated the process of crystallization on niobia. For our experiments, the maximum value of S_{BET} was 120 m^2/g on support NB400 that did not have any additional acid treatment. In turn, the NBAc400 support was submitted to an acid treatment

and also to one additional calcination to remove weakened adsorbates. Therefore, those might be reasons for the reduction of area for the NBAc400 from 120 to 37 m^2/g and also for the diminution of pore volumes.

Okazaki and Kurosaki (1990) and Okazaki and Wada (1993) cited decrements on the surface area on H_3PO_4-treated niobium oxide. According to them, the aging time on acid treated influenced the superficial area, with diminution of 90% after 120 h days of exposure to acid. Then, the treatment time of 72 h could be a reason for lower superficial area of te NBAc400 support. Besides, Okazaki and Kurosaki (1990) treated niobium oxide with a 0.5 mol/L H_3PO_4 during 48 h and related that calcination temperatures lower than 600 °C decreased the superficial area of treated support up to 30% due to the formation of a phosphoric acid layer. However, pretreatment temperatures of 600 and 800 °C shifted the area of treated niobia to higher values compared to non-treated samples. The authors reported a suppression of crystallization and also more stable sample due to the H_3PO_4-treatment (Okazaki and Kurosaki, 1990).

At Table 5.1, the activated catalysts CoNB10, NiNB10 and RuNB05 presented reduced superficial areas and pore volumes compared to the calcined support NB400. RuNB05 had 25 m^2/g, about 80% less area compared to support NB400. Conversely, CoNB10 and NiNB10 presented the same trend, with 39 and 36 m^2/g respectively. Song and Li (2006) had reported that the incorporation of 15 wt.% Co into SiO_2 by IWI decreased the pore volume by 50%. Also, 20 wt.% Ni/Al_2O_3 showed reduced areas, pore volume and pore sizes related to original support (Cepeda *et al.*, 2016).

Despite the cited literature, several works used WI with higher superficial areas in Ni and Ru catalysts supported on Nb_2O_5 - Table 5.2. A possible cause might be the elevated active phase content on IWI, which could promote obstruction of smaller pores of the original support. In fact, the mean pore diamaters for CoNB10, NiNB10 and RuNB05 were twice compared to NB400 (113, 117 and 103 vs 51 Å).

The Figure 5.1 to 5.8 showed similar types of IUPAC isotherms - mesoporous materials (Thommes *et al.*, 2015). Although the isotherms for NB400 to RuNB05 had similar trends, it was noted that the pore distribution for the supported CoNB10, NiNB10 and RuNB05 solids presented a shift to larger pores - *ca.* 100 Å. Then, the IWI could have shifted the catalyst pores to larger sizes.

Table 5.2: Textural properties of Co, Ni and Ru supported on Nb_2O_5 support.

Metal	S_{BET} [m^2/g]	D_{BJH} [Å]	Method	Reference
10 wt% Co	39	113	IWI	This work
	38	n.a.	GP	(PÂRVULESCU *et al.*, 1998)
10 wt% Ni	36	117	IWI	This work
	104	70	WI	(COSTA, 2021)
5 wt% Ru	25	103	IWI	This work
	128	50	WI	(COSTA, 2021)

Figure 5.1: Isotherm for NB400 catalyst.

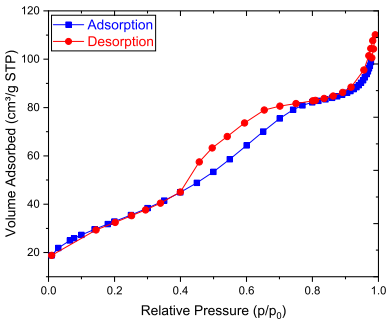

Figure 5.2: dVdlog(D) for NB400 catalyst.

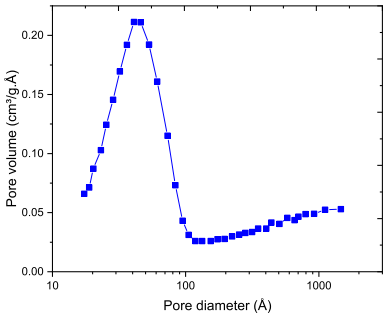

Figure 5.3: Isotherm for CoNB10 catalyst.

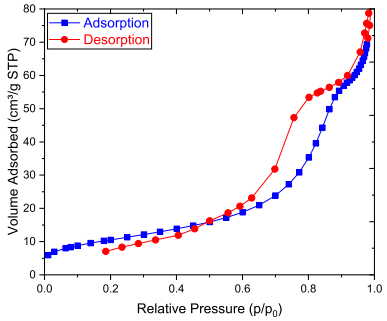

Figure 5.4: dVdlog(D) for CoNB10 catalyst.

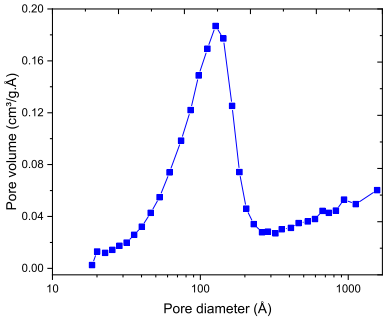

Concerning the acid treatment, the CoNBAc10, NiNBAc10 and RuNBAc05 presented superior specific area compared to the treated support NBAc400. Gao *et al.* (2021) studied acid treatment with phosporic acid on Ni/Al_2O_3 catalysts. Conversely to our results, a 15% incorporation of P into alumina descreased the support area from 168

to 35 m^2/g. Moreover, an addition of 10 wt.% of Ni on treated support increased the area from 35 to 47 m^2/g. The article reported that the incorporation of P into alumina destroyed the original pore structure, once could produce layer of oxides and also $AlPO_4$, curbing the superficial area. Gao *et al.* (2021) also proposed that the incorporation of Ni suppressed the formation of the previous substances, increasing the pore volume of the treated-alumina.

Figure 5.5: Isotherm for NiNB10 catalyst.

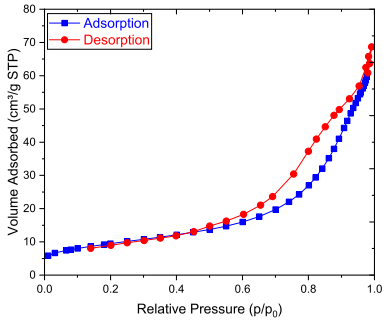

Figure 5.6: dVdlog(D) for NiNB10 catalyst.

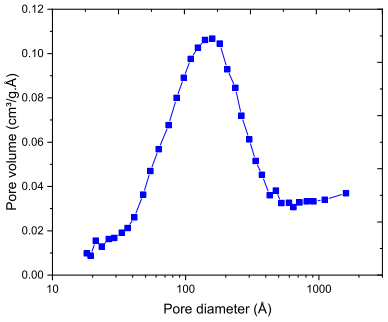

Figure 5.7: Isotherm for RuNB05 catalyst.

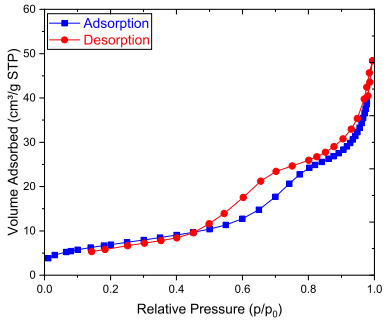

Figure 5.8: dVdlog(D) for RuNB05 catalyst.

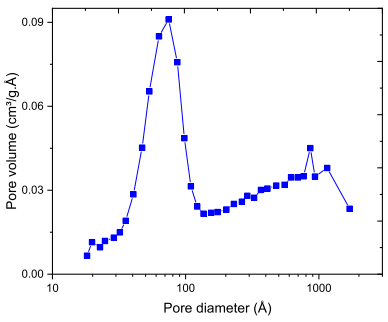

In our CoNBAc10, NiNBAc10 and RuNBAc05 samples, we could observe a similar trend, especially on Figures 5.11 to 5.16. Comparing CoNB10 and CoNBAc10, on Figures 5.4 and 5.12, it was also possible to observe the modification on the pore sizes, from 113 to 60 Å. The same phenomenon occurred on treated NiNBAc10 - 117 to 72 Åand RuNBAc05 - 103 to 81 Å, on Figures 5.6 and 5.14 and Figures 5.8 and 5.16, respectively. Then, we could infer that the acid treatment followed by an H_2 activation might reopen and modify the previous destroyed pores. However, more experimental characterization should be necessary to prove the hypothesis.

Figure 5.9: Isotherm for NBAc400 catalyst.

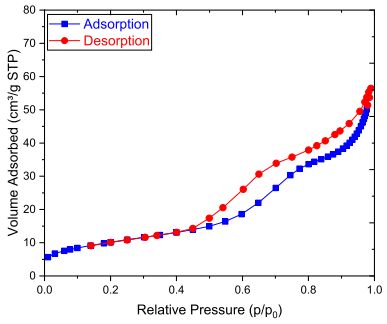

Figure 5.10: dVdlog(D) for NBAc400 catalyst.

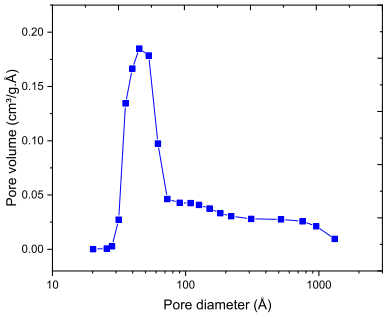

Figure 5.11: Isotherm for CoNBAc10 catalyst.

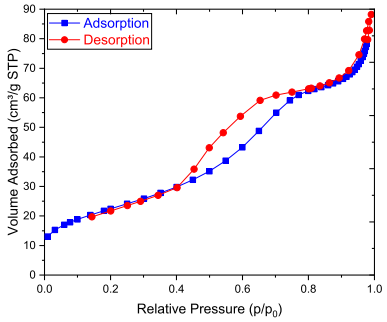

Figure 5.12: dVdlog(D) for CoNBAc10 catalyst.

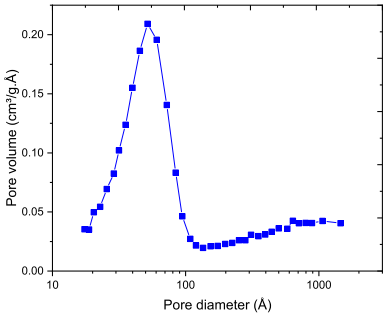

Furthermore, comparing the acid catalysts with acid support NBAc400, the modification of pore diameters was not so high as in the support NB400. As an example, the pore size of CoNB10 was more than twice compared to NB400 whereas the same amount was 30% lower on CoNBAc10 comparing to NBAc400. However, aside from the acid treatment in NBAc400, it was not reported any major modification on the pore volumes of samples. Then, this could be another indication of the reconfiguration of pores after the reduction on acid samples.

Figure 5.13: Isotherm for NiNBAc10 catalyst.

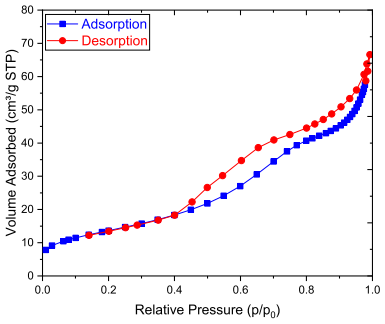

Figure 5.14: dVdlog(D) for NiNBAc10 catalyst.

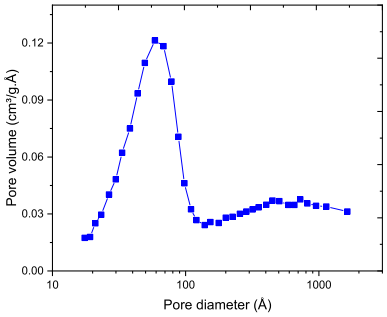

Figure 5.15: Isotherm for RuNBAc05 catalyst.

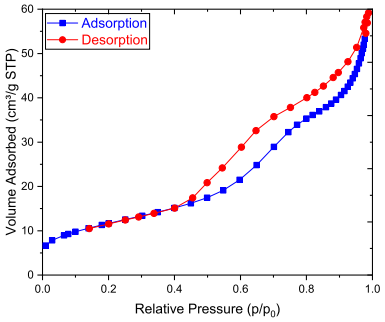

Figure 5.16: dVdlog(D) for RuNBAc05 catalyst.

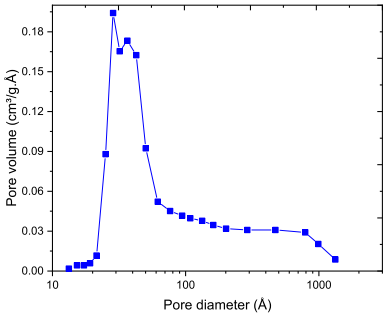

5.1.2 SEM/EDX - Chemical Compositions

The analysis of chemical compositions in the catalyst provided different results about the effects of the acid treatment. The Table 5.3 and Table 5.4 gives the content of Nb, O and metal active phase for each one of the solids.

Table 5.3: Elemental analysis for CoNB10, NiNB10 and RuNB05 after activation on H_2 flow.

Catalyst	Nb (wt%)	O (wt%)	Cl (wt%)	Metal (wt%)
CoNB10	56	34	0.9	9.1
NiNB10	55	35	-	9.6
RuNB05	55	42	-	3.0

Activation conditions: 60 mL/min H_2 at 400 °C during 2 h.

-: Cl was not identified in NiNB10 and RuNB05 samples.

Table 5.4: Elemental analysis for CoNBAc10, NiNBAc10 and RuNBAc05 after activation on H_2 flow.

Catalyst	Nb (wt%)	O (wt%)	P (wt%)	Cl (wt%)	Metal (wt%)
CoNBAc10	44	40	5	0.5	10.0
NiNBAc10	44	41	6	-	8.4
RuNBAc05	48	41	5	-	4.8

Activation conditions: 60 mL/min H_2 at 400 °C during 2 h.

-: Cl was not identified in NiNB10 and RuNB05 samples.

At Table 5.3, the catalysts CoNB10 and NiNB10 presented the mean bulk amount of metal similar to the nominal content (10 wt.%). However, there was detection of Cl on CoNB10 samples. This might be an indication of Cl adsorption over Nb samples, due to the high chloride content on precursors. Furthermore, there is the possibility of a mixture of cobalt oxides in the surface instead of the totally reduced species, once the reduction was carried out at 400 °C. According to the experiments of (Mejía *et al.*, 2017), a similar Co-niobia suported catalyst presented the first event of reduction at 600 °C . On the contrary, the RuNB05 solid presented different amounts of Ru compared to the nominal value - 3 wt.% vs 5 wt.%. In this situation, there was low possibility of EDX analysis error, due to the semi-quantitative approach. One reason for the difference might be experimental erros carried our during the IWI procedure for the RuNB05.

The Table 5.4 expressed contents of P the three samples of CoNBAc10, NiNBAc10 and RuNBAc05 dolids. In fact, the three solids presented at least 5 wt.% of phosphorous on the mean composition. In agreement with NB400 derived solids, the CoNBAc10 solid also presented Cl detected on analysis and the active phases of NiNBAc10 and RuNBAc05 was close to the nominal value. Even after the activation on H_2, the solids presented phosphorous on the composition. Then, the addition of P due to the acid treatment was succeed.

5.1.3 XRD - Presence of Crystalline Phases

The Figures 5.17 to 5.20 showed the results of XRD experiments. The supports NB400 and NBAc400 were calcined in synthetic air with 80 mL/min during 4 h and 400

°C while the metal samples were activated in H_2 with 60 mL/min during 2 h and 400 °C. Once the treatment temperatures were lower than 500 °C, it was not expected that the catalysts presented events of crystallization.

The supports NB400 and NBAc400 did not show any event of crystallization on Figure 5.17. It was possible to make the hypothesis that the calcination temperature did not change the amorphous pattern into crystals. Similar results were reached by Costa (2021) and de Lima (2020).

Figure 5.17: XRD patterns for NB400 and NBAc400.

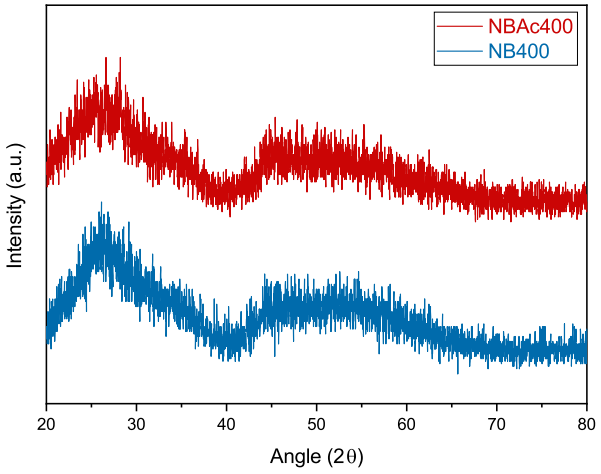

Pretreatment: synthetic air flow 80 mL/min during 4 h and 400 °C.

Step used for the offset: 60 a.u.

In agreement with both supports, the CoNB10 and CoNBAc10 were predominately amorphous, as stated on Figure 5.18. The result was in accordance with recent literature studies. Mejía *et al.* (2017) impregnated 10 wt.% Co on niobic acid ($Nb_2O_5 \cdot nH_2O$) with 120 °C and 600 °C pretreatment temperatures on air. They reported an amourphous samples up to 600 °C, when the events of crystallization on niobia were reported. Then, the calcination at 400 °C did not provide crystal contents either for both Co samples.

Figure 5.18: XRD patterns for CoNB10 and CoNBAc10.

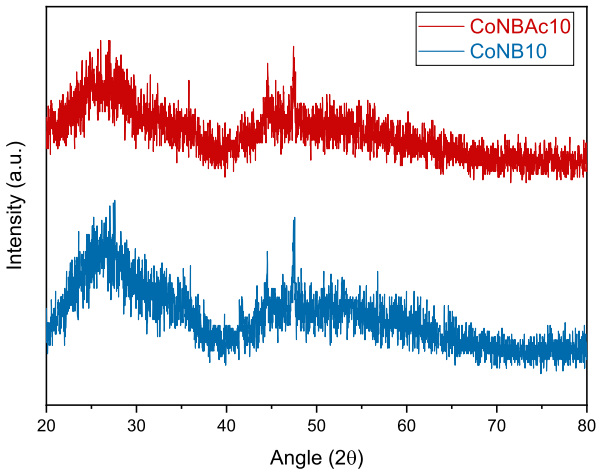

Pretreatment: H_2 flow 60 mL/min during 2 h and 400 °C.

Step used for the offset: 60 a.u.

In turn, the Ni catalysts NiNB10 and NiNBAc10 in Figure 5.19 presented peaks with different events of crystallization.

Figure 5.19: XRD patterns for NiNB10 and NiNBAc10.

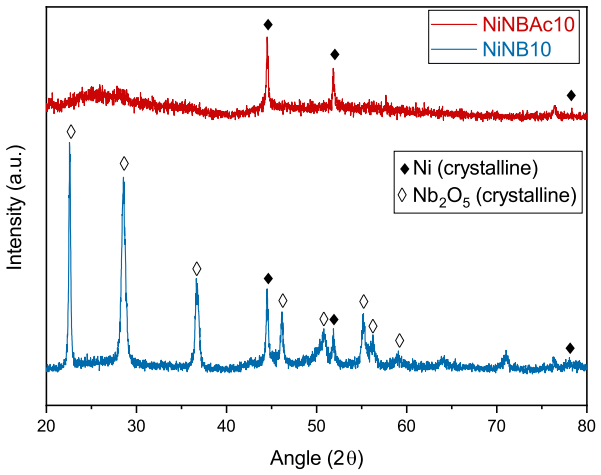

Pretreatment: H_2 flow 60 mL/min during 2 h and 400 °C.

Step used for the offset: 420 a.u.

The database reported three peaks at $2\theta = 44.5^o$, $2\theta = 51.9^o$ and $2\theta = 76.5^o$ for cubic Ni crystals on NiNB10 and NiNBAc10 (Ref. Pattern 01-087-0712 for both solids). In fact, the NiNB10 catalyst not only presented cubic Ni crystals, but also an hexagonal Nb_2O_5 crystalline domain, even though the calcination and reduction temperature did not exceed 400 °C. The peaks related to hexagonal crystalline niobia were observed at

$2\theta = 22.6^o$, $2\theta = 28.6^o$, $2\theta = 36.6^o$, $2\theta = 46.1^o$, $2\theta = 50.8^o$, $2\theta = 55.2^o$, $2\theta = 56.3^o$ and $2\theta = 59.0^o$ (Ref. Pattern 01-087-0712 for 00-028-0317). As a first remark, the possibility upon the reduction of Nb_2O_5 into crystalline NbO_2 under hydrogen flow at 400 °C is not suitable, once this phenomenon was described from 800 °C and beyond by Soares *et al.* (1993), Mendes *et al.* (2003) and da SQ Menezes *et al.* (2020) for pure Nb_2O_5. Then, the crystalline events for Ni and niobia on NiNB10 might be an influence of the metal phase on support.

According to Sankar *et al.* (1988), a 10 wt% Ni/Nb_2O_5 solid reduced under H_2 flow at 500 °C presented an SMSI effect. The elevated Ni content provided a reorganization over the support in the vicinity of nickel particles. This effect probably lead to a change in the amorphous content of the support into crystals. Furthermore, de Sousa *et al.* (2017) proposed that more flexible pores of niobia were filled with Ni, changing also the conformation of Nb_2O_5 network. Other literature works reported that Ni contents above 5 wt.% induced to crystallization of the Nb_2O_5 support, like Chary *et al.* (2004) and Wojcieszak *et al.* (2006). So, the elevated content of Ni during IWI in our NiNB10 solid might had induced the crystallization of our support, even at activation temperatures lower than 500 °C.

However, contrary to the NiNB10 solid, the NiNBAc10 catalyst had only cubic Ni peaks on XRD as depicted on Figure 5.19. Some causes were studied on recent articles. Rocha *et al.* (2020) demonstrated that the acid treatment at 0.5 to 2.0 M of H_3PO_4 up-shifted the original crystallization temperature of niobia at 500 °C. In addition, a charge modification on NBAc400 surface cannot be discarded, once the phosphate provided stabilization of niobia surface (Okazaki and Kurosaki, 1990). Then, the crystallization of the acid support NBAc400 was not observed or there was lack of interaction of Ni.

The Ru catalysts RuNB05 and RuNBAc05 did not presented any peak concerning to the metal nor the support on Figure 5.20. As related by Costa (2021), this probably occurred due to the low content in impregnation on niobia.

Figure 5.20: XRD patterns for RuNB05 and RuNBAc05.

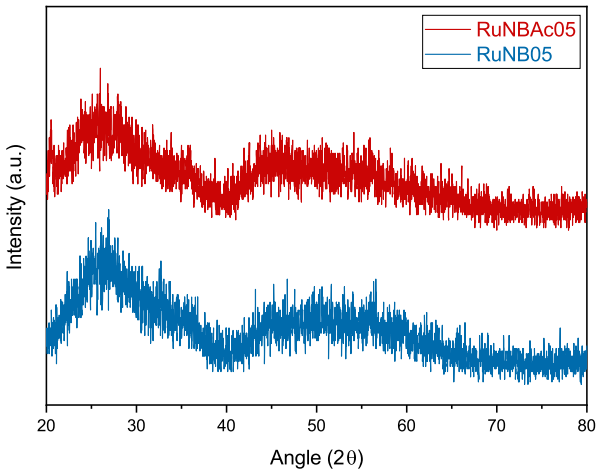

Pretreatment: H_2 flow 60 mL/min during 2 h and 400 °C.

Step used for the offset: 60 a.u.

To conclude this section, the crystallite size was calcuated using the Scherrer relation for NiNB10 and NiNBAc10. At Table 5.5, the major peaks, references, as well as the results were summarized. Even though the shape factor was supposed to be 0.9 (spherical domain condition), the outcomes does not equal to particle size due to approximations over the Scherrer equation. For a more realistic measure of particle size, a TEM analysis would be more suitable.

Table 5.5: Crystalline domain size calculated by XRD patterns.

Catalyst	Phase	2θ Peaks [°]	Reference	Crystalline size [nm]
NiNB10	Cubic Ni	44.5/51.9/76.5	Swanson and Tatge (1953)	34
NiNBAc10	Cubic Ni	44.5/51.9/76.5	Swanson and Tatge (1953)	38
NiNB10	Hexag. Nb_2O_5	22.6/28.6/36.6/46.1 50.8/55.2/56.3/59.0	Frevel and Rinn (1955)	35

5.1.4 H_2 - TPR - Study About the Formation of Active Phases

The Table 5.6 expressed the results of TPR analyses. All catalysts presented similar H_2 uptakes - close to 10 μmol H_2/mg metal. In short, the Co based solids did not reach the first event of reduction, the Ni catalysts were in the middle of the reduction and there was a complete reduction of Ru samples.

Table 5.6: TPR uptakes and temperature events.

Catalyst	H_2 uptake (μmol/mg metal)	Calculated H_2 uptake (μmol/mg metal)	Peaks (°C)
CoNB10	13	23	460/592
CoNBAc10	7	23	458/582
NiNB10	16	17	425
NiNBAc10	14	17	435
RuNB05	12	20	176
RuNbAc05	11	20	172

Samples calcined prior to the H_2-TPR for 400 °C and 4 h in synthetic air.

At Table 5.6, the catalysts with acid treatment presented a lower H_2 uptake compared to non-treated solids. In the case of CoNBAc10, that difference was up to 50%. Even with higher areas, those results could exist due to P-groups on catalyst surface, that hindered an more effective reduction of CoNBAc10, NiNBAc10 and RuNBAc10. However, further studies and analysis are required to an exact conclusion.

Furthermore, another indication of the reduction of metal species on surface was expressed on Equations 5.1, 5.2 and 5.3. Supposing the existance of oxides on surface CoNB10 and CoNBAc10 reached 57% and 31% of theoretical H_2 uptake respectively. Indeed, the results for Ni were 95% and 84% for treated and non-treated solids; and for Ru, 60% for RuNB05 and 54% for RuNBAc05. Then, those outcomes could be an indication of the reduced availability of metal sites due to IWI.

$$Co_3O_4 + 4 \cdot H_2 \rightarrow 3 \cdot Co^0 + 4 \cdot H_2O \quad (23 \mu mol H_2/mg Co) \tag{5.1}$$

$$NiO + H_2 \rightarrow Ni^0 + H_2O \quad (17\mu molH_2/mgNi) \tag{5.2}$$

$$RuO_2 + 1.5 \cdot H_2 \rightarrow Ru^0 + 3 \cdot H_2O \quad (20\mu molH_2/mgRu) \tag{5.3}$$

On Table 5.6 and Figures 5.21, 5.22 and 5.23, the temperature for TPR events were determined. Concerning to CoNB10 sample, it had two major peaks at *ca.* 460 and 590 °C. Noronha *et al.* (1999) had studied similar TPR results on a 10% Co/Nb_2O_5 solids. They had observed the formation of two minor peaks at 360 and 460 °C - related to the reduction of Co_3O_4 to CoO. Furthermore, a final event on 521 °C was assigned to CoO complete reduction to Co (Noronha *et al.*, 1999). Then, the two peaks on CoNB10 existed because of the two step reduction of Co_3O_4 to Co. Also, the differences on temperatures might be assigned to precursors: Co chlorine was used on this work instead of Co nitrate. Even on other supports, the steps of Co reduction were observed, as reported by Oliveira *et al.* (2014) - ca. 510 and 730 °C on Co/Al_2O_3 solid.

The CoNBAc10 presented the same peaks compared to CoNB10. However, the first (458 °C) presented similar intensity, whereas the second (582 °C) had a lower value. Furthermore, the CoNBAc10 had a final peak at 730 °C. However, it was not possible to determine whether that peak could be assigned to phosphorous decomposition on catalyst surface, or even if the acid treatment delayed the reduction of Co particles. Therefore, that value was not calculated for Co reduction.

The NiNB10 had a peak on 425 °C, which was in accordance to reported results on literature. Lensveld *et al.* (2001) had observed the NiO reduction to Ni^0 at 400 °C on a Ni/MCM-41 solid. Furthermore, Mile *et al.* (1990) divided the Ni reduction on Ni/silica on 3 steps. At 200 °C (reduction of Ni^{3+}), 400 °C (reduction of NiO with low interaction with support) and 500 °C (NiO with elevated interaction with support). To complete, Mejía *et al.* (2020) reported peaks at 430 °C on Ni/Nb_2O_5 solid, which was also assigned to NiO reduction. Then, the event on NiNB10 solid might be related to NiO conversion to Ni.

Figure 5.21: H_2 TPR results - CoNB10 and CoNBAc10.

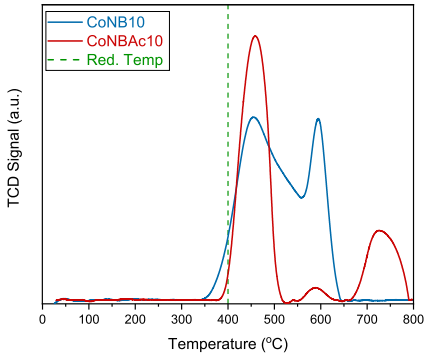

Figure 5.22: H_2 TPR results - NiNB10 and NiNBAc10.

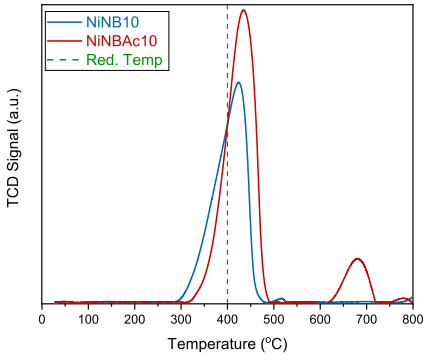

Figure 5.23: H_2 TPR results - RuNB05 and RuNBAc05.

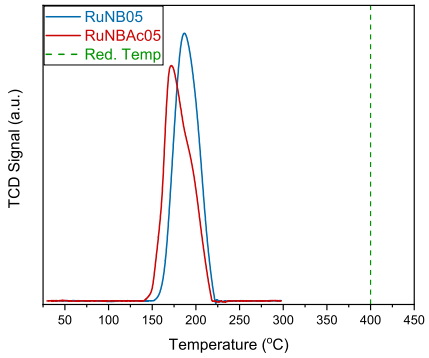

Concerning to acid treatment, the NiNBAc10 solid had two peaks on Figure 5.22: 435 and 680 °C. As previously cited, the first one could be assigned to NiO reduction to Ni. Related to the second peak, though, several results detailed the P incorporation on Ni/Al_2O_3 catalysts (Gao *et al.*, 2021). Their TPR results had a second event *ca.* 750 °C. Gao *et al.* (2021) established that high contents of P induced the passivation of Ni surface, curbing the formation of Ni^0 on lower temperatures. Then, the acid treatment could delayed the reduction of metal species. However, on NiNBAc10 solid, the similar peak could be assigned to P elimination on higher temperatures, or even the reduction of Nb_2O_5 to NbO_2 (Mejía *et al.*, 2017). Then, the event at 680 °C was not accounted on H_2 uptake, once further analysis would be necessary to prove or not a P release.

Our RuNB05 solid presented a sharp peak at Figure 5.23 at about 176 °C. First, the presence of only one peak at Ru/Nb_2O_5 denoted the reduction of Ru^{4+} to

Ru^0, *i.e.*, the existence of oxides on surface (Chary *et al.*, 2009). Chary *et al.* (2009) had also reported a similar peak on a 5 wt% Ru/Nb_2O_5 at 220 ° C. Furthermore, the transformation of RuO_2 into Ru was demonstrated by Mendes *et al.* (2004) on a bimetallic $Ru\text{-}Co/Nb_2O_5$ catalyst. Their TPR event was assigned on 260 °C. To conclude, Suppino (2014) observed two peaks on Ru-niobia solids - 60 °C and 250 °C, the first related to Ru chlorine transformation and the latter with Ru oxides. Then, the event on RuNB05 catalyst may be related to Ru oxides reaction to metal Ru.

Nonetheless, the RuNBAc05 presented an H_2 uptake at 172 °C on Figure 5.23. An opposite trend was observed on modified P-Ru catalysts supported on alumina (Fovanna *et al.*, 2020). The modifications with ammonium hypophosphite changed their H_2 events from 195 °C to 98 °C. They related that the phosphorous induced to a reduced activation barrier of H_2 dissociation, especially on minor Ru clusters. Moreover, Fovanna *et al.* (2020) demonstrated that P also induced an improvement of Ru particles on alumina support. Then, despite the minor H_2 intake, the acid treatment could had modified the Ru behavior into Nb_2O_5 support.

5.1.5 XPS - Oxidation of species

In this section, the results of the catalyst prior to reactions were given. The Figure 5.24 to 5.26 summarized the results of XPS analyses over the catalyst samples of NB400 and NBAc400. The Figures 5.27 to 5.31 provided results for CoNB10 and CoNBAc10 solids. The XPS for nickel catalysts NiNB10 and NiNBAc10 were expressed on Figures 5.32 to 5.36. Finally, the Figures 5.37 to 5.41 demonstrated the XPS outcomes for RuNB05 and RuNBAc05 catalysts.

The Figure 5.24 showed that the NB400 catalyst had a peak on 207.1 eV and a doublet separation of 2.8 eV. Those values of Nb $3d_{5/2}$ were reported on literature concerning to formation of Nb_2O_5 species on surface, according to Simon *et al.* (1976) and García-Sancho *et al.* (2014). Then, only Nb and O species were detected on NB400, once this solid was an outcome of the calcination pretreatment.

Figure 5.24: XPS spectrum and fitting for Nb 3d on NB400.

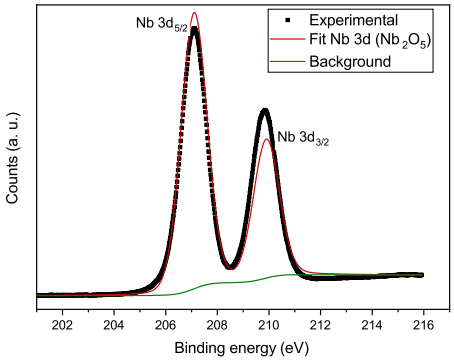

Figure 5.25: XPS spectrum and fitting for Nb 3d on NBAc400.

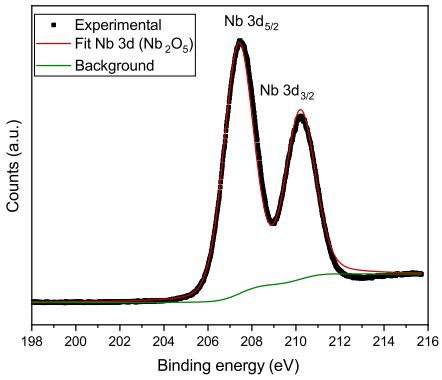

Figure 5.26: XPS spectrum and fitting for P 2p on NBAc400.

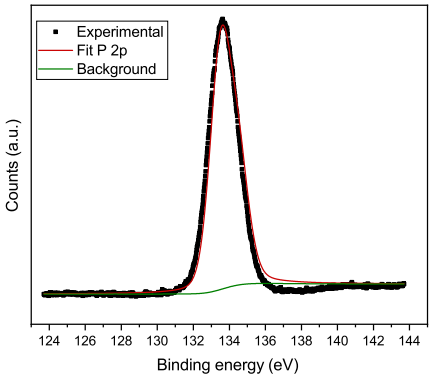

The utilization of the acid treatment provided some changes on NBAc400 spectra. The spectrum was shifted by 0.3 eV compared to carbon. The main peak ($3d_{5/2}$) was fitted on 207.4 eV and the separation was 2.8 eV (Figure 5.25). Once again, the most prominent phase of Nb was under Nb_2O_5 phase. Another important feature on NBAc400 was also the detection of P 2p species, as stated on Figure 5.26. The major peak was detected on 133.5 eV, probably related to $2p_{3/2}$. According to Rotole and Sherwood (1998) and Pereira *et al.* (2014), this binding energy was related to phosphate species configuration of P. Therefore, there was an indication of P incorporation due to acid treatment. The Table 5.7 described the results of XPS and peak attribution of species NB400 and NBAc400.

Table 5.7: Resume of XPS spectra - NB400 and NBAc400.

Catalyst	Element	B.E (eV)	Species	References
NB400	Nb - $3d_{5/2}$	207.1	Nb_2O_5	García-Sancho *et al.* (2014)
NBAc400	Nb - $3d_{5/2}$	207.4	Nb_2O_5	García-Sancho *et al.* (2014)
	P - $2p_{3/2}$	133.5	Phosphate	Pereira *et al.* (2014)

B.E.: binding energy

The cobalt solid CoNB10 presented several peaks, as depicted on Figure 5.27: one at 780.6 eV and another on 786 eV. According to (Noronha *et al.*, 1999), the event at 780.6 eV could be assigned to a variety of Co oxides and hydroxides, including CoO, Co_3O_4 and $Co(OH)_2$. In addition, Tan *et al.* (1991) mentioned that Co^{2+} and Co^{3+} species had satellite peaks *ca.* 786 eV. On both situations, the doublet separation was 16.0 eV, which was confirmed by XPS Nist Database. Also, it was possible to identify CoO or Co_3O_4 substances. As reported by Noronha *et al.* (1999), the first compound had sharp satellites, while the second one had broader features. So, the observation of Figure 5.27 was an indication of Co^{2+} as the most prominent state of oxidation on CoNB10.

Concerning to niobium oxide, the same spectrum for Nb was detected on CoNB10, as reported on Figure 5.28. Then, the probability for reduction of niobia the support is reduced. In addition, the formation of cobalt-niobate is reported at elevated temperatures, *e.g.* 900 to 1100 K (Noronha *et al.*, 1999).

The CoNBAc10 solid presented different outcomes compared to non-treated CoNB10. Regarding to Co species, the satellite peaks were less pronounced, as reported on Figure 5.29. Therefore, the acid treatment induced a mixture of oxidation states in Co (2+ and 3+), once the most prominent species on CoNBAc10 was pointed out as Co_3O_4. As opposed to other samples, the XPS spectrum of Nb 3d on CoNBAc10 solid was the only contrasting - Figure 5.29. Besides, the fitting calculated two main peaks of Nb $3d_{5/2}$: 206.6 eV and 207.6 eV. Fontaine *et al.* (1977) pointed out the 207.6 eV as the characteristic energy for niobium pentoxide solids, *i.e.*, Nb_2O_5. Then, the peak at 206.6 eV required further investigation.

Xiang *et al.* (2017) reported that Nb_2O_5 had the feature to produce structural defects combined with base metals. Among the base species, Co_3O_4 induced vacancies

on Nb_2O_5 surface (Xiang *et al.*, 2017). In addition, the mentioned events could lead to the formation of oxophilic NbO_x species during reduction with H_2, particularly Nb^{4+} and Nb^{5+} Barrios *et al.* (2018). Also, Tran *et al.* (2019) established that the reduction of niobium pentoxide is less probable on crystalline states, due to low mobility of species. Therefore, given the previous information, and also the corresponding peaks of 206.6 eV and 205.9 eV as Nb^{4+}, remarked by the works of Fontaine *et al.* (1977) and Tran *et al.* (2019), the acid treatment could have produced new vacancies on the acid treated CoNBAc10 amorphous surface, leading to the formation of NbO_x species at lower reduction temperatures. Nonetheless, the hypothesis require more characterization results for confirmation.

As well as Nb spectrum on CoNBAc10 analysis, the P spectrum contrasted to the others on Figure 5.31. According to the recent research of Hu *et al.* (2019b), the acid treatment of phosphoric acid over starch led to defects on surface and different oxidation number on P species, changing then its spectrum. Again, this hypothesis may be reinforced by more experimental data. To summarize the discussed peaks and compounds for CoNB10 and CoNBAc10 solids, the Table 5.8 presented the main results.

Table 5.8: Resume of XPS spectra - CoNB10 and CoNBAc10.

Catalyst	Element	B.E (eV)	Species	References
CoNB10	Co - $2p_{3/2}$	780.6	CoO	Noronha *et al.* (1999)
	Nb - $3d_{5/2}$	208.6	Nb_2O_5	García-Sancho *et al.* (2014)
CoNBAc10	Co - $2p_{3/2}$	781.4	Co_3O_4	Noronha *et al.* (1999)
	Nb - $3d_{5/2}$	207.6	Nb_2O_5	Fontaine *et al.* (1977)
	Nb - $3d_{5/2}$	206.6	NbO_2	Fontaine *et al.* (1977)
	P - $2p_{3/2}$	132.6	Phosphates	Hu *et al.* (2019b)

B.E.: binding energy

Figure 5.27: XPS spectrum and fitting for Co 2p on CoNB10.

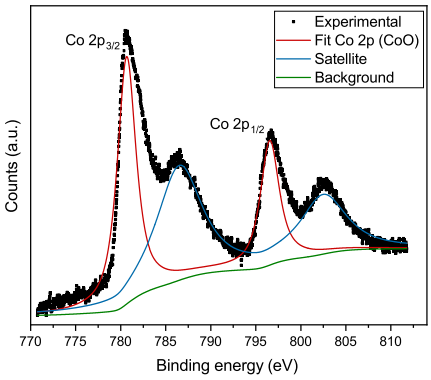

Figure 5.28: XPS spectrum and fitting for Nb 3d on CoNB10.

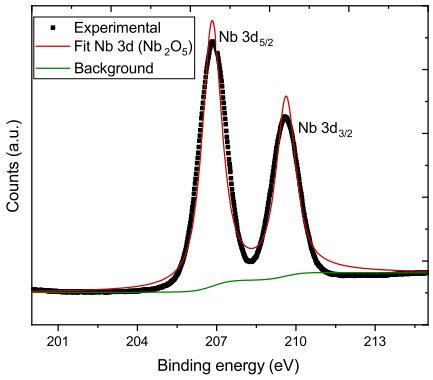

Figure 5.29: XPS spectrum and fitting for Co 2p on CoNBAc10.

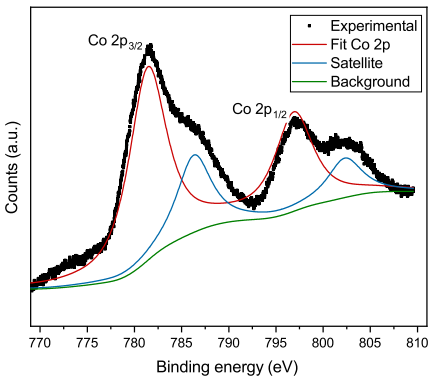

Figure 5.30: XPS spectrum and fitting for Nb 3d on CoNBAc10.

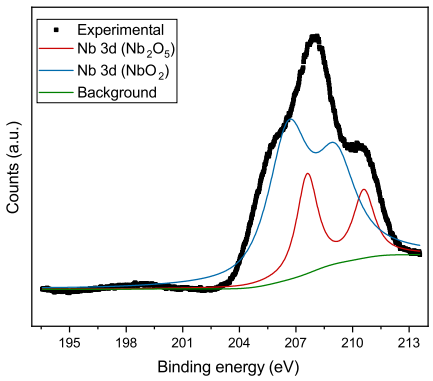

Figure 5.31: XPS spectrum for P 2p on CoNBAc10.

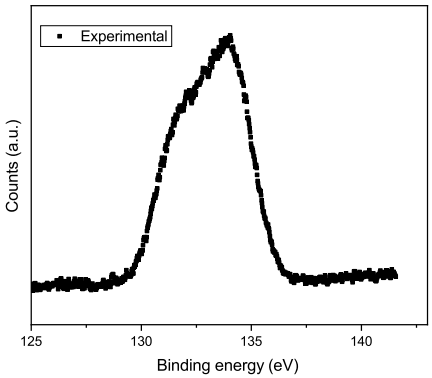

The catalyst NiNB10 had two Ni peaks at 852.0 eV and 855.7 eV, both with a doublet separation of 18.0 eV (Figure 5.32). The studied literature reported similar values: Furstenau *et al.* (1985) established 852.2 eV as a binding energy for Ni and Ertl *et al.* (1980) cited 855.5 eV as the binding energy for NiO. Besides, at 861.3 eV and 879.8 eV there were evidences of satellite peaks, which can be set to NiO or $Ni(OH)_2$, according to NIST XPS Database. As the reduction of sample was carried out under H_2 flow and the Ni impregnation was incipient, the formation of hydroxide on surface is not expected. Then, the oxidation states of Ni on NiNB10 surface after reduction were +2 and 0. The Nb 3d spectrum had on NiNB10 similar behavior compared to support NB400, as stated on Figure 5.33. The major 3d peak was detected on 206.8 eV, with a doublet separation of 2.8 eV. So, the formation of NbO_x, *i.e.*, reduction of Nb_2O_5 support, might be excluded.

Compared to the non-treated solid, the XPS outcome for NiNBAc10 on Figure 5.34 presented shifts on the peaks related to Ni: 818.8 eV and 856.0 eV. Similarly to the NiNB10 solid, a mixture of NiO and Ni was proposed on catalyst surface. According to Okazaki and Kurosaki (1990), the presence of P could disturbed Nb atoms, which was an indication of the shift on XPS peaks on niobium catalysts. In addition, similar shifts were reported for Nb $3d_{5/2}$ on Figure 5.35, on the peak of 207.1 eV and doublet separation of 2.8 eV. However, no indication of Nb_2O_5 was detected. Finally, the Figure 5.36 provided the peak of 133.1 eV for P, indicating the incorporation of the species due to acid treatment. To sum up, the results and literature for NiNB10 and NiNBAc10 solids were expressed at Table 5.9.

Table 5.9: Resume of XPS spectra - NiNB10 and NiNBAc10.

Catalyst	Element	B.E (eV)	Species	References
NiNB10	Ni - $2p_{3/2}$	852.0	Ni^0	Furstenau *et al.* (1985)
	Ni - $2p_{3/2}$	855.7	NiO	Ertl *et al.* (1980)
	Nb - $3d_{5/2}$	206.9	Nb_2O_5	García-Sancho *et al.* (2014)
NiNBAc10	Ni - $2p_{3/2}$	851.8	Ni^0	Furstenau *et al.* (1985)
	Ni - $2p_{3/2}$	856.0	NiO	Ertl *et al.* (1980)
	Nb - $3d_{5/2}$	207.1	Nb_2O_5	Fontaine *et al.* (1977)
	P - $2p_{3/2}$	133.1	Phosphates	Pereira *et al.* (2014)

B.E.: binding energy

Figure 5.32: XPS spectrum and fitting for Ni 2p on NiNB10.

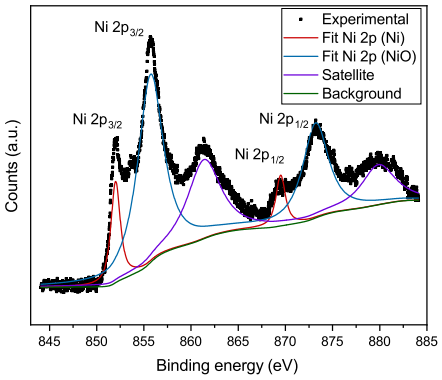

Figure 5.33: XPS spectrum and fitting for Nb 3d on NiNB10.

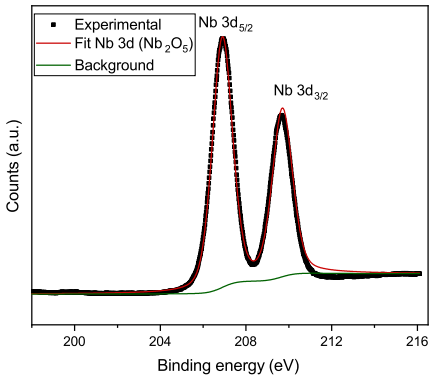

Figure 5.34: XPS spectrum and fitting for Ni 2p on NiNBAc10.

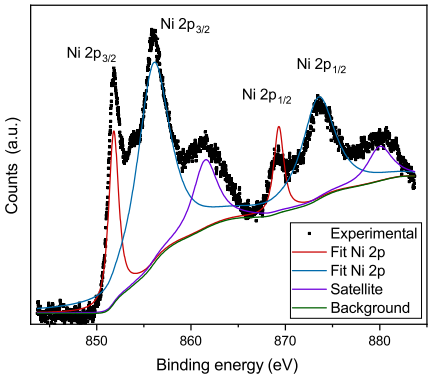

Figure 5.35: XPS spectrum and fitting for Nb 3d on NiNBAc10.

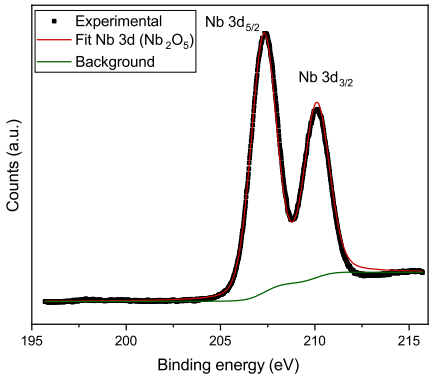

Figure 5.36: XPS spectrum for P 2p on NiNBAc10.

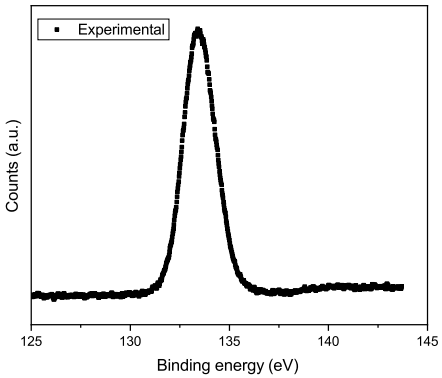

The spectra of RuNB05 and RuNBAc05 were presented on Figures 5.37 to 5.41. The lines of C 1s may disturb the results of Ru 3d, once the peak of carbon is close to 284.6 eV. This value is a separation of the peak of metallic Ru at around 280.6 eV (Morgan, 2015). The Figure 5.37 presented the Ru results over RuNB05 solid. According to Morgan (2015), the main peak for Ru - $3d_{5/2}$ is related to the binding energy of 280.6 eV - presence of Ru or Ru oxides. However, due to reduction conditions, most of the Ru on surface may be metallic. Besides, in our sample, the reported peak was over 284.6 eV instead of 280.6 eV. This could occur due to the carbon on sampler analyzer. Egawa *et al.* (1987) cited 285.0 eV as a binding energy for reduced species of Ru. The same peak of 284.6 eV for Ru was reported for acid treatment on RuNBAc05 solids - Figure 5.39. Again, this was an indication for the existence of metallic sites on surface. Conversely with RuNB05, the sample also presented the same peaks for Nb 3d at 206.9 eV (Figure 5.40). On RuNBAc05 samples, conversely to NBAc400 and NiNBAc10 solid, the phosphorous also was detected on the acid treatment, as given on Figure 5.41. Finally, the Table 5.10 expressed the results for Ru catalysts.

Table 5.10: Resume of XPS spectra - RuNB05 and RuNBAc05,

Catalyst	Element	B.E (eV)	Species	References
RuNB05	Ru - $3d_{5/2}$	284.6	Ru^0	Egawa *et al.* (1987)
	Nb - $3d_{5/2}$	206.8	Nb_2O_5	García-Sancho *et al.* (2014)
RuNBAc05	Ru - $3d_{5/2}$	284.6	Ru^0	Egawa *et al.* (1987)
	Nb - $3d_{5/2}$	206.8	Nb_2O_5	García-Sancho *et al.* (2014)
	P - $2p_{3/2}$	133.1	Phosphate	Pereira *et al.* (2014)

B.E.: binding energy

Figure 5.37: XPS spectrum for Ru 3d on RuNB05.

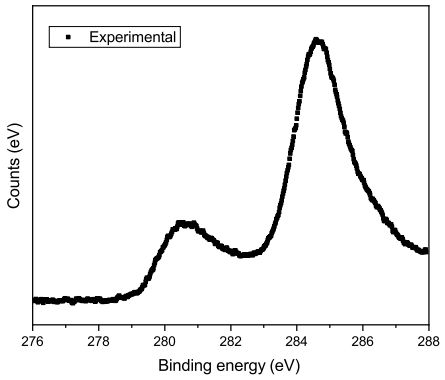

Figure 5.38: XPS spectrum for Nb 3d on RuNB05.

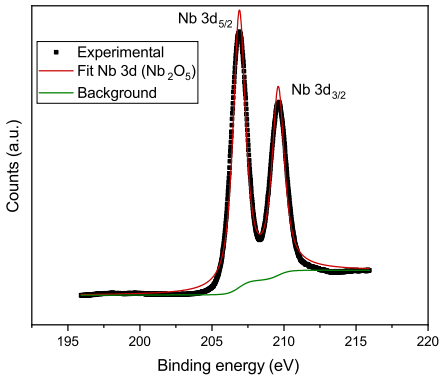

Figure 5.39: XPS spectrum for Ru 3d on RuNBAc05.

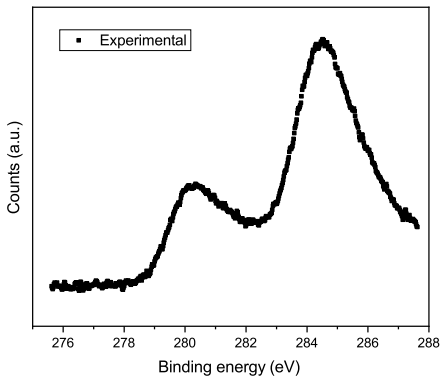

Figure 5.40: XPS spectrum for Nb 3d on RuNBAc05.

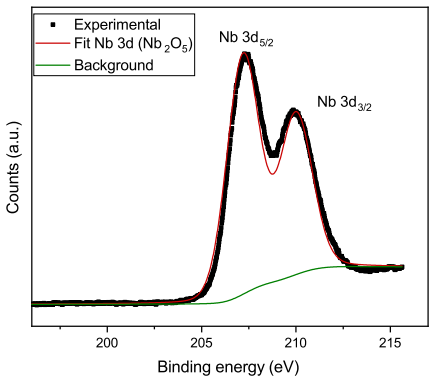

Figure 5.41: XPS spectrum for P 2p on RuNBAc05.

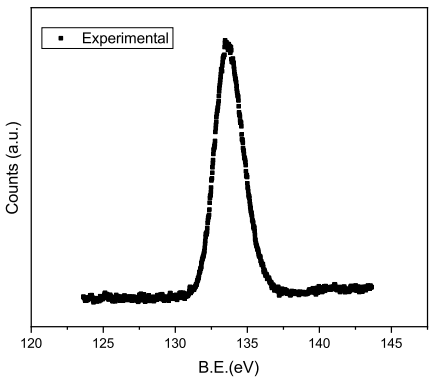

5.1.6 NH_3 - TPD - Total Acidity

The Figures 5.42 to 5.45 showed the TPD results for all solids. Also, only the total acidity and the strength of the acid sites were calculated, not LAS and BAS sites. As a consequence, the LAS and BAS sites were not differentiated, once the NH_3 may be adsorved on both sites. For this type of information, another experiments, such as FTIR with pyridine as probe molecule are recommended. Therefore, the effects of the H_3PO_4 acid treatment and the metal impregnation might be inferred.

Figure 5.42: TPD results for NB solids.

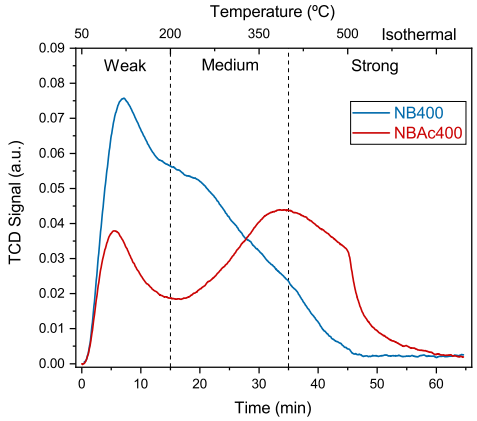

Figure 5.43: TPD results for Co solids.

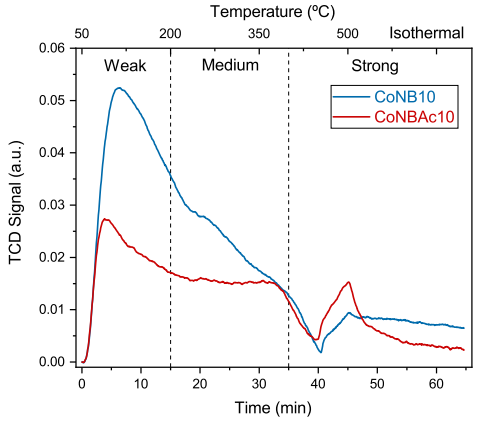

Figure 5.44: TPD results for Ni solids.

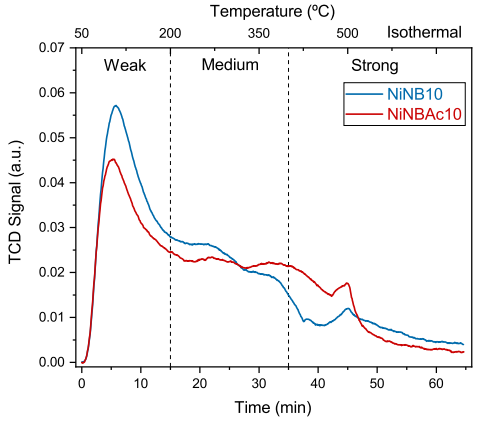

Figure 5.45: TPD results for Ru solids.

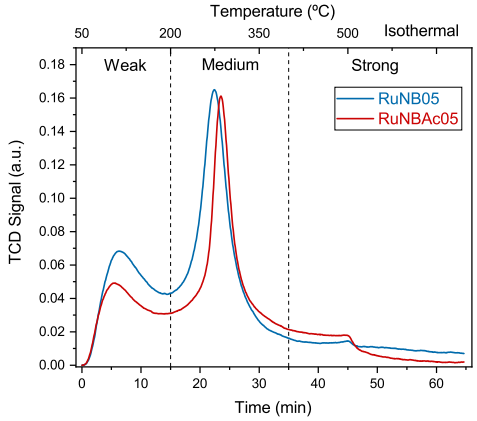

At Figure 5.42 the effects of the acid treatment were noted due to the change in amount of medium acid sites on NB and NB400 (50% and 63%, respectively). Those outcomes were pointed out by literature [(Brandão *et al.*, 2009), (de Pietre *et al.*, 2010) and (Tang *et al.*, 2010)]. According to them, the acid treatment not only provided new textural properties to niobia but also inserted a stronger acidity compared to the non-treated solid. In addition, Okazaki *et al.* (1987) attributed the high amount of stronger

sites to the formation of a non-volatile polyphosphate layer during pre-treatment and the ability of the niobia to retain acid groups. Once Gnanakumar *et al.* (2019) attributed the peaks at 500 °C as possible dehydroxylation of the niobia -OH groups, those event could not be assigned as a strong acid site. Further confirmation will be necessary using a blank TPD.

Apart from NB400 support, the catalyst CoNB10 showed varied events after 350 °C, as reported on Figure 5.43. After all, an intense diminution followed by a rapid increase on TCD signal. Then, there was an unusual interaction of NH_3 with Co. As an example, Pendyala *et al.* (2013) studied the irreversible adsorption of NH_3 into Co/Al_2O_3 solids. They pointed out that 100 ppm of NH_3 adsorved into Co sites, curbing the catalyst activity. Then, the intensity of the signal at higher temperatures on CoNB10 may not be assigned to strong acid sites. Besides, a similar trend was also noticed on CoNBAc10 sample, also on Figure 5.43. The difference on the spectra after 350 °C could not be assigned to the release of ammonia or he phosphate groups from acid treatment, once a thermal conductivity detector was used. Therefore, conversely to CoNB10, the presence of strong acid sites on CoNBAc10 cannot be inferred from NH_3-TPD.

The Figure 5.44 depicted the results of TPD on NiNB10 and NiNBAc10 samples. Concerning to Ni sites, Weng *et al.* (2015) and Henpraserttae (2018) mentioned the decomposition of NH_3 into H_2 and N_2 on metal Ni sites above 400 °C. As XPS results on Figures 5.32 and 5.34 provided the presence of Ni and NiO after reduction, the peak on both samples at *ca.* 450 °C cannot be appointed only to NH_3. As consequence, the presence of strong acid sites is not preserved on Ni solids.

Compared to Ni and Co solids, both Ru catalysts provided a sharp peak on TCD signal around 300 °C on Figure 5.45. The same trend was detected on the experiments carried out by Nagai *et al.* (1997) on a 3 wt% Ru/Al_2O_3 catalyst. According to mass spectroscopy measures, they concluded that two types of acid sites co-existed at the solid: the sites capable of adsorption and desorption of NH_3 (support and Ru) and the metallic sites that promoted the low temperature decomposition of ammonia from 300 °C to above. Therefore, not only the detection of strong acid sites was not clear, but the temperatures above 300 °C. So, most of the sites were considered weak to medium.

Based on the previous results, the Table 5.11 showed the trends of NH_3-TPD on all catalysts. On all samples, the acid treatment decreased the total acidity. However,

only on NBAc400 the density of acid sites was twice compared to NB400, once the metallic solids presented asymmetric events above 300 or 400 °C. Then, there were difficulties on determination of strong acid sites on those samples. Furthermore, the content of medium acid sites on those catalysts had a slight increase, indicating the presence of new groups, probably phosphates, as demonstrated by XPS studies.

Table 5.11: Total acidity and strength of supports and catalysts studied.

Catalyst	Total Acidity (μmolNH$_3$/g)	Density of Acid Sites (μmolNH$_3$/m^2)	Strength of the sites (%)		
			Weak	Medium	Strong
NB400	614	5	50	50	-
NBAc400	397	9	37	63	-
CoNB10	408	11	56	44	-
CoNBAc10	214	3	49	51	-
NiNB10	371	10	55	45	-
NiNBAc10	341	7	51	49	-
RuNB05	721	29	37	63	-
RuNBAc05	594	11	34	66	-

Weak sites: 0 to 200 °C; Medium sites: 200 to 400 °C; Strong sites: above 400 °C.

Source: (Berteau and Delmon, 1989); -: events at strong sites region.

To conclude this section, the Figures 5.46 and 5.48 provided a summary about the total acidities for samples (μmolNH$_3$/g), acidities per area (μmolNH$_3$/m^2) and also the strength distribution of the sites.

Among the catalysts of Figure 5.46, the Ni-based samples presented the lower difference of total acidity, about 30 μmolNH$_3$/g or less than 10%. As a first remark, the interference of Ni over niobia might be inferred. Gnanakumar *et al.* (2019) cited that a 40 wt.%Ni/Nb_2O_5 solid had elevated contents of weak and medium sites, conversely to our samples. Then, the incorporation of Ni into niobia might provide deposit on Nb_2O_5 acid sites. However, further investigation is necessary to confirm the hypothesis.

Figure 5.46: Total acidities (μmolNH$_3$/g) over TPD studies.

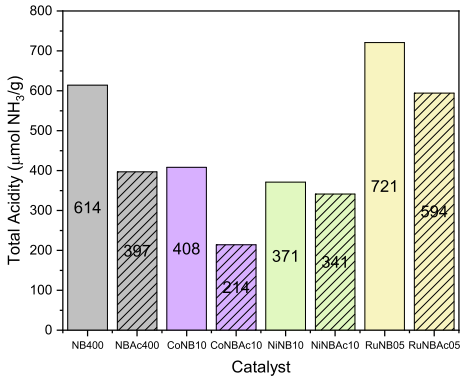

Figure 5.47: Specific acidities (μmolNH$_3$/m^2) over TPD studies.

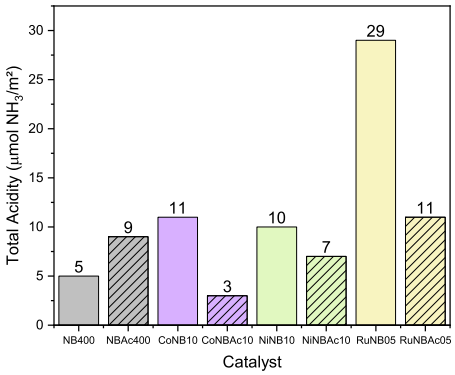

Figure 5.48: TPD - percentage of weak, medium and strong sites.

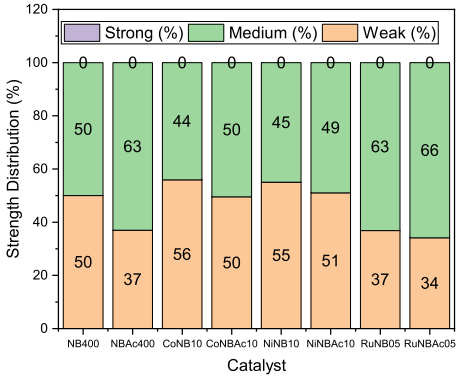

5.2 Reactions Results

On this section, the results of conversion and selectivity were explored. It is important to point out that only xylose (XYL) was identified as pentose, even though other substances, as xylylose, may exist over the reaction. So our conversion will be assigned as pentoses conversion (PEN conversion). Furthermore, the other identified compounds were furfural (FUR), furfuryl alcohol (FA), tetrahydrofurfuryl alcohol (THFA), xylitol (XOL), levulinic acid (LA) and cyclopentanone (CPO), with their HPLC chromatography patterns on Section 7.

It should be also remarked that the supports NB400 and NBAc400 were previously calcined at synthetic air for 400 °C during 4 h before the reaction. In turn, the

Co, Ni and Ru based-solids were activated at H_2 flow for 400 °C during 2 h.

5.2.1 Catalytic Performance

The Figures 5.49 to 5.50 showed the performance of the calcined NB400 catalyst at 160 °C and 50 bar of H_2 pressure. No GVL was detected on any reaction.

Figure 5.49: PEN conversion, FA, FUR and THFA selectivity - NB400.

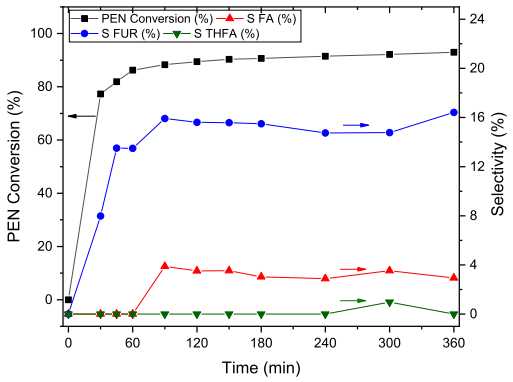

Figure 5.50: Carbon balance - NB400.

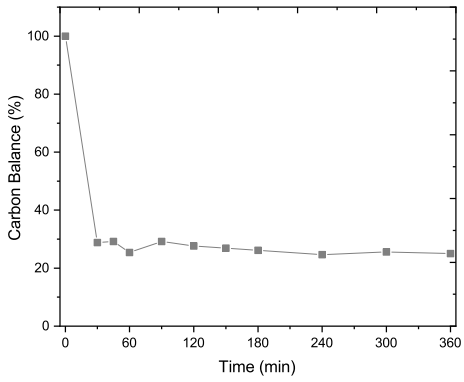

The Figure 5.49 showed a pentose conversion of 93%, followed by a FUR and FA selectivities of 16% and 3%, respectively on NB400 solid. Indeed, the conversion was *ca.* 90% from 60 min to the end of reaction. Even producing humins, Pholjaroen *et al.* (2013) reported an increased catalyst activity on FUR synthesis at elevated temperatures. Besides, concerning to FUR production, de Carvalho *et al.* (2019) reported similar outcomes with niobia in water medium: 92% of XYL conversion and 9% of FUR selectivity. According to the authors, the formation of carbon deposits over niobic acid was a reason for reduced FUR selectivity.

During our NB400 reactions, no production of XOL, CPO, GVL or LA was detected because the Nb_2O_5 did not provide further metal sites for hydrogenation. However, a minor production of FA and THFA was detected, with 3% and 1% of selectivity. Considering this outcome, two hypothesis may be described. First, the BAS content could have transformed FUR into FA (Karinen *et al.*, 2011). And second, the excess of H_2 on reaction medium, could make a minor hydrogenation route on N_2O_5, though no evidence was pointed out by recent literature.

More specifically, Gupta *et al.* (2017) demonstrated the presence of water-

tolerant LAS on N_2O_5 at 120 °C, which could be another explanation for the high conversion. Furthermore, de Lima *et al.* (2021) also reported that a major LAS content on niobia promoted the formation of soluble byproducts. Therefore, it might explain the low values of carbon balance on Figure 5.50, with 25% at the end of reaction. It was corroborated by Figure 5.51 below, where several peaks could not be assigned, especially from 12 to 20 min of analysis.

Figure 5.51: Chromatogram at HPLC of the reaction system after 6 h of reaction with NB400 catalyst.

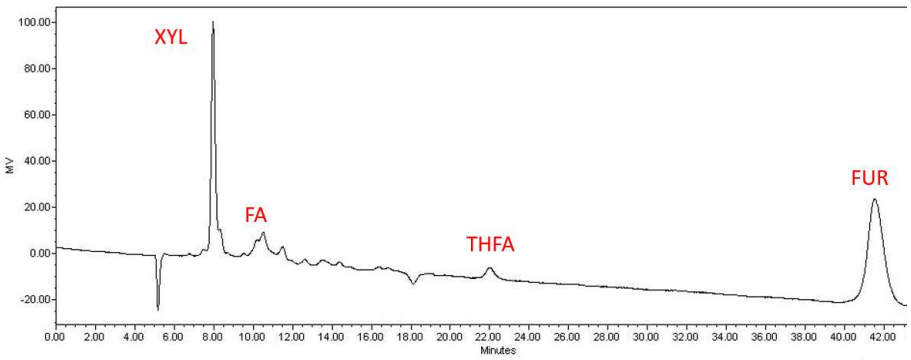

The Figures 5.52 to 5.53 reported the PEN conversion, selectivity to other substances and carbon balance on NBAc400 catalyst. There were differences on catalyst performance compared to NB400. On Figure 5.52, the reported PEN conversion at the end of reaction decreased from 90% on NB400 to 71% on NBAc400. Besides, the trend of conversion curve changed from a saturation shape to a linear behavior. The diminution on conversion might be correlated to the 60% less area on NBAc400 solid, providing more reactions on surface instead of pores, in agreement with de Lima (2020).

The NBAc400 catalyst provided 45% of FUR selectivity at the end of reaction. In fact, several researches on literature have confirmed this trend. Tang *et al.* (2010) used a similar niobia modified by H_3PO_4 on sorbitol dehydration to isosorbide. They reached the conclusion that the interaction of NB=O groups with adjacent POH and NbOH species increased the selectivity on dehydration routes. Besides, Pholjaroen *et al.* (2013) reported that niobium phosphate increased selectivity to FUR on XYL dehydration, due to promotion of direct route - without isomers. At last, Termvidchakorn *et al.* (2017) used H_3PO_4-modified carbon catalysts on XYL dehydration and confirmed that the acid-functionalized solid prevented humins formation, avoiding an excess of LAS groups. Then, the superior performance of NBAc400 related to FUR frmation might be assigned to the

presence of the new P groups from acid treatment.

Figure 5.52: PEN conversion, FA, FUR and THFA selectivity - NBAc400.

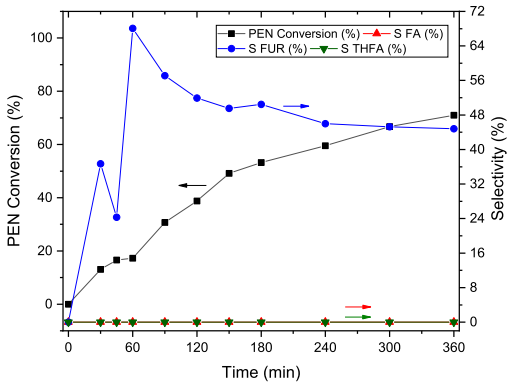

Figure 5.53: Carbon balance - NBAc400.

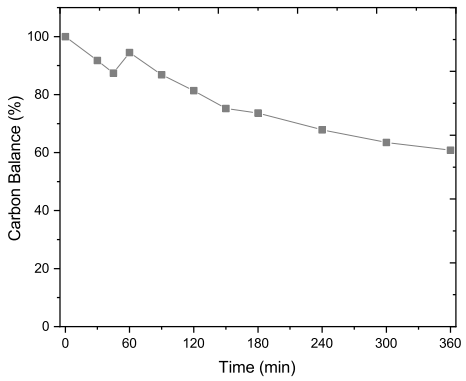

The NH_3-TPD results showed an incorporation of medium acid groups on NBAc400 solid compared to NB400 (50% vs 63%).Zhu *et al.* (2017a) used a similar acid-modified niobia solid, and treated solid could improve the 5-HMF selectivity on fructose dehydration. The researchers reported that the incorporation of phosphorous by acid treatment also contributed to stronger acid groups P-OH. Then, the P groups on NBAc400 contributed to stronger acidity and could shift the reaction to FUR synthesis.

Conversely with NB400, the NBAc400 catalyst presented low contents of hydrogeneation route products - 0% of FA and THFA as reported on Figure 5.52. In contrast, the Figure 5.53 showed a final carbon balance of 61% on NBAc400 reaction, which may be related to the superior FUR formation. Carniti *et al.* (2006) demonstrated that niobium phosphate deactivated less rapidly than niobium oxide due to less humins formation on fructose dehydration.

In addition, it was reported that the phosphate groups were more active in polar and protic media, as water or ethanol (Carniti *et al.*, 2006). Therefore, the acid treatment could improve the carbon balance at NBAc400 support. This is reinforced by the HPLC result on Figure 5.54, showing less unidentified peaks than NB400 from the region of 12 to 20 min.

Figure 5.54: Chromatogram at HPLC of the reaction system after 6 h of reaction with NBAc400 catalyst.

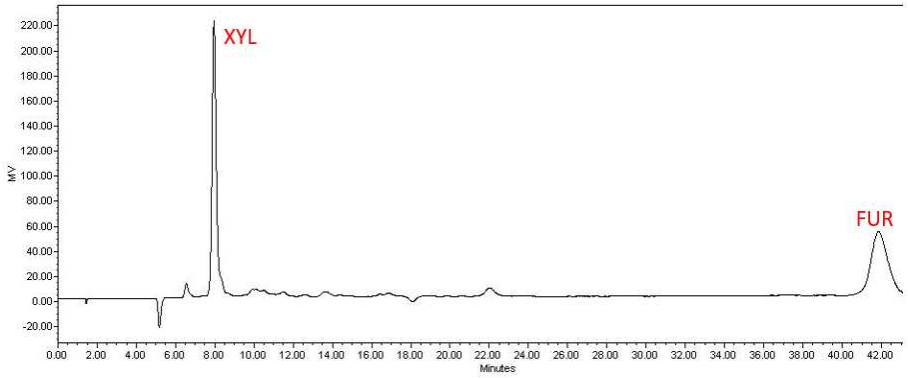

The Figures 5.55 to 5.56 showed the catalytic performance of Co solid CoNB10. Conversely to the support NB400, the final PEN conversion reported on Figure 5.55 was *ca.* 99%. Also, besides the FUR selectivity of 5%, a considerable amount of FA and THFA were produced - 14% and 5% of selectivity, respectively. In this situation, the influence of both support NB400 and active phase CoO were studied.

Figure 5.55: PEN conversion, FA, FUR and THFA selectivity - CoNB10.

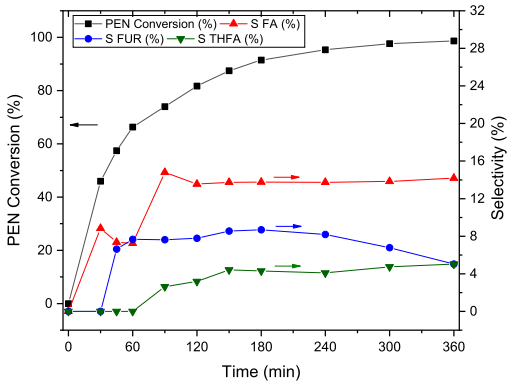

Figure 5.56: Carbon balance - CoNB10.

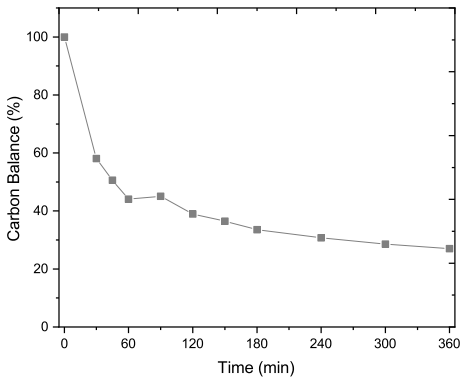

With regard to FA production from FUR, the control of hydrogenation is a major concern, once there is a competition between C=C and C=O bonds on FUR (Wang *et al.*, 2020). In addition, Parikh *et al.* (2019) established that the metals of group IB (Co and Cu) do not saturate C=C bond, making the furan ring not reactive. In fact, the XPS results of Figure 5.27 showed that major species on CoNB10 surface was CoO (Co^{2+}). Liu *et al.* (2019) did not report metal Co sites on Co/SiO_2 solids on temperatures lower than 500 °C because Co induced many oxygen vacancies on catalytic system. Therefore, there were evidences for the existence of CoO species on CoNB10.

However, there was not an agreement on literature about the activity of Co^0, CoO and Co_3O_4 on FUR hydrogenation. According to Audemar *et al.* (2015), the presence of metal Co^0 sites were essential to FA production. On the other hand, the DFT calculations of Nguyen-Huy *et al.* (2019) demonstrated that the cleavage of -OH group on FA was easier on CoO than in Co, showing then, higher activity to FUR and FA hydrogenation. Also, Wang *et al.* (2020) reported that a bulk CoO catalyst induced the FUR reduction to FA and THFA on water at 120°C and 10 bar H_2 pressure. They pointed out that the THFA production was promoted due to the cleavage of C-OH bond on FA to THFA on CoO solids. Therefore, the presence of THFA might exist due to CoO sites on CoNB10.

It was reported a minor production of LA and CPO with 1% of selectivity for both compounds. The literature reported excess of water as a reaction media for LA production from FUR over water and acidity, because of the FUR ring opening (Albilali *et al.*, 2018). In addition, the H^+ acidity and the reduction of FUR may produce CPO (Hronec and Fulajtarová, 2012). Also, (Jiang *et al.*, 2018) reported that low dissolution of FUR on water did not provide high reaction rates and exposure to further hydrogenation paths. Then, the use of water as solvent and the low hydrogenation of CoO might explain the low formation of LA and CPO.

The final value of carbon balance of CoNB10 solid was 27% at Figure 5.56. It could be assigned as an influence of support NB400 that presented 20% of this value. Again, the HPLC on CoNB10 on Figure 5.57 remained to show unidentified products from 14 to 20 min. The incorporation of Co oxides on niobia surface could also produce LAS that are responsible for the generation of more soluble products. As example, the studies of Mekhemer *et al.* (1999) and Dewangan *et al.* (2019) demonstrated that Co^{+n} species on silica and alumina surfaces could enhance the formation of potential Lewis acid sites. Therefore, aside from the water-tolerant LAS from niobia support, there could be the existence of LAS from CoO, curbing the carbon balance.

In addition, the Figure 5.57 expressed the HPLC results at the end of the reaction for the CoNB10 solid. Specially for the 12 to 20 min region of the unidentified prodcuts, the CoNB10 catalyst had a similar pattern compared to NB400. Also, the incorporation of Co had increased the contents of FA and THFA, even with minor contents of CPO and LA.

Figure 5.57: Chromatogram at HPLC of the reaction system after 6 h of reaction with CoNB10 catalyst.

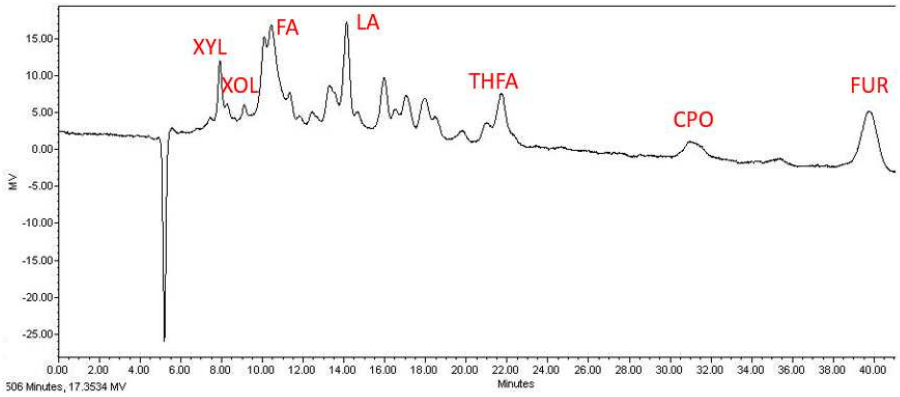

The Figures 5.58 to 5.59 showed the catalytic performance of Co solid CoNBAc10. Except for a growing trend, the final PEN conversion was 90%, as provided on Figure 5.58, a similar value compared to 98% on CoNB10. Furthermore, the FA and THFA selectivities were 9% and 3% respectively. The reduced FA production could occur once a FUR content of 11% was reported after 6 h of reaction. Then, the incorporation of P on niobia support had influenced the performance of CoNBAc10 solid.

Figure 5.58: PEN conversion, FA, FUR and THFA selectivity - CoNBAc10.

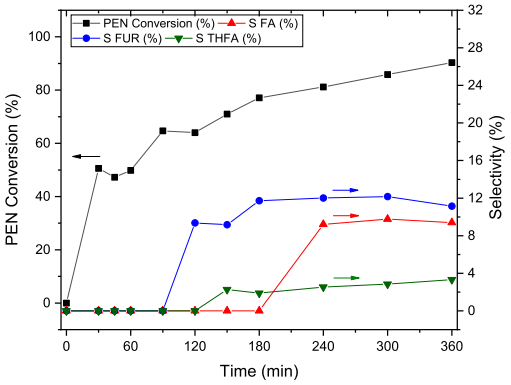

Figure 5.59: Carbon balance - CoNBAc10.

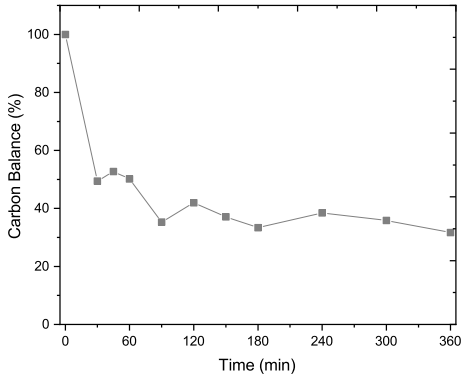

The major species on CoNBAc10 surface was Co_3O_4, as described by Figure 5.28. It is a mixture of Co^{3+} and Co^{2+} (Noronha *et al.*, 1999). In conformity with recent researches, Co_3O_4 (CoNBAc10) provided less formation of FA than CoO (CoNB10). Nguyen-Huy *et al.* (2019) reported that Co_3O_4 showed little activity for FUR hydrogenation on liquid phase, and Wang *et al.* (2020) pointed out 0% of FA selectivity on FA production in water. Moreover, when Co_3O_4/SBA-15 solid was reduced to Co/SBA-15 at 500°C, the obtained FA yield increased from 0% to 88% (Audemar *et al.*, 2015).

Second, the acid treatment inserted new P groups on CoNBAc10 surface, especially phosphates (Figure 5.31). As far as researched, no work about acid treated niobia for FUR hydrogenation was found. However, Liu *et al.* (2021) produced a modified TiO_2 catalyst with a similar H_3PO_4 treatment for the acetalization of FUR. The paper described that the acid treatment had created potential BAS (PO_4^{3-}) on titania surface. However, those new groups not only had contributed to lower FA formation, but also modified the binding energy of H_2 over catalyst surface (Liu *et al.*, 2021). Besides, a recent outcome published by Fang and Riisager (2022) established that elevated acidities (above 300 μmol/g) contributed to reduced FA formation on aluminum-phosphates catalysts. Then, the P incorporation from the acid treatment could have damaged the FUR conversion on further products.

Only 0.5% of LA formation was detected on CoNBAc10 solid. In addition, the production was reported after 240 min of reaction. So, this could be another indication of the outcome of acid treatment on further FUR reactions of CoNBAc10. Nonetheless, the reduced PEN conversion and increased FUR formation did not improve the carbon balance on Figure 5.59 - 32% at the end of reaction, compared to 27% on CoNB10 sample. Especially on the HPLC on Figure 5.60, the unidentified peaks had lower intensity. Furthermore, humin formation was also present. Then, the acid treatment on CoNBAc10 reduced the selectivity of products from FUR hydrogenation rather than improving both routes (XYL dehydration and FUR reduction).

Figure 5.60: Chromatogram at HPLC of the reaction system after 6 h of reaction with CoNBAc10 catalyst.

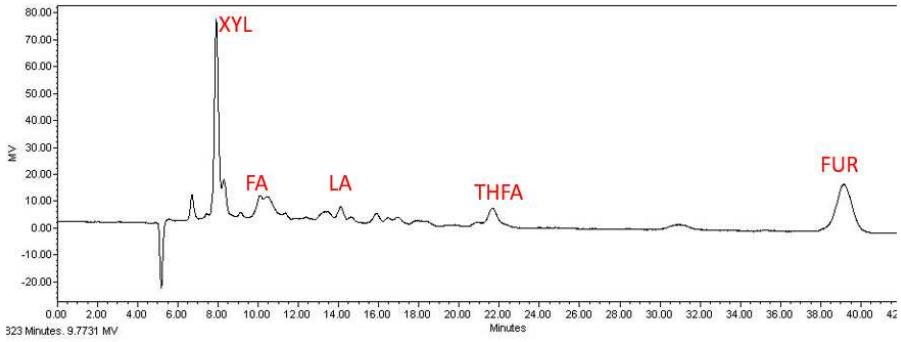

The Ni catalyst NiNB10 had their catalytic performances expressed from Figures 5.61 to 5.63. Despite the elevated XYL conversion (98% at the end of reaction), the catalyst remained inactive up to 45 min of reaction. This could be an influence of the low superficial area (36 m^2/g), once the reaction could take place on the surface. Besides,

once the NiNB10 sample was not totally reduced, the activation of the catalyst by H_2 atmosphere could take some time, generating then the profile of Figure 5.61. Furthermore, different trends were related to FA, THFA and other products. At Figure 5.61, the final selectivity of FA and THFA were 16% and 6%, respectively. However, the FA selectivity presented a peak of 32% at 60 min and the THFA selectivity one with 6% at 180 min. Besides, the FUR selectivity during all the reaction was 0%.

Figure 5.61: PEN conversion, FA, FUR and THFA selectivity - NiNB10.

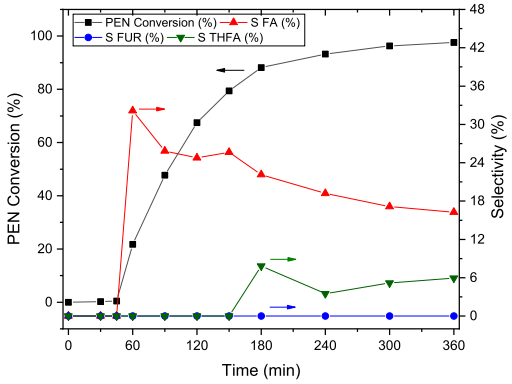

Figure 5.62: Selectivity to XOL, LA, CPO and GVL - NiNB10.

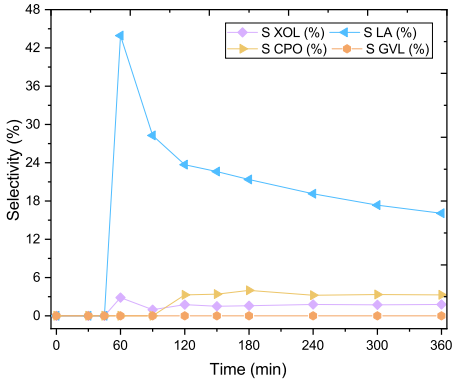

Figure 5.63: Carbon balance - NiNB10.

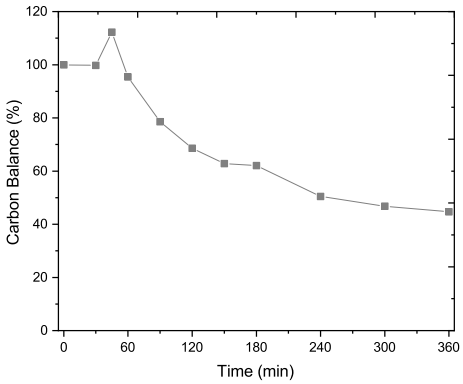

The Figure 5.62 also pointed out several differences to the previous Co-based catalysts. At 60 min, the LA selectivity was 44%, though it reduced to 16% at the end of reaction. The CPO selectivity was also superior than Co solids - 3%. Even the XOL production was identified, with 2% after 360 min of reaction. So, the presence of Ni and NiO on NiNB10 must be studied.

No Ni/Nb_2O_5 catalyst was found on literature research for the XYL to FA reaction. However, some works might draw varied conclusions of the NiNB10 performance.

Yu *et al.* (2014) demonstrated that Ni^0 had adsorved liquid FUR on furan ring and carbonyl groups, *i.e.*, on C=C and C=O bonds, which promoted further hydrogenation to other products, like THFA, CPO and 2-MF. As a result, Ni particles were reported as non-selective catalysts to FA production, due to lack of control on hydrogenation step [(Yan *et al.*, 2014), (O'Driscoll *et al.*, 2017), (Guo *et al.*, 2019)]. In fact, the hydrogenation route could have been more favored than the dehydration, once XOL was produced and no FUR was identified.

The Ni content on NiNB10 sample was close to 10 wt%. Hu *et al.* (2019a) reported that non-uniform sites on Ni/alumina solids lead to generation of THFA. They also remarked that elevated Ni contents curbed metal dispersion and promoted excessive FA hydrogenation and hydrogenolysis, producing THFA and CPO (Hu *et al.*, 2019a). It was also confirmed that the presence of water on FUR hydrogenation generated 1-pentanol and 1,5-pentanediol from FA (Merat *et al.*, 1990). For those reasons, the presence of Ni sites and water on NiNB10 caused not only an uncontrolled FUR hydrogenation to FA, but also the production of THFA, LA and CPO.

The carbon balance on Figure 5.63 showed improvements, with a final value of 45% at the end of reaction. However, the value showed decrement along the reaction.Merat *et al.* (1990) linked the reduction of activity Ni catalyst on FUR hydrogenation due to poisoning and deactivation of the solid. Besides, loss of performance on NiO catalyst during FA production was reported due to adsorption of organic species (He *et al.*, 2018). Those results could support the formation of resins on Ni catalysts. In fact, the XPS results on Table 5.9 confirmed the presence of NiO on NiNB10 surface. Then, the NiO could had produced undesired products, as resins.

Conversely to NB400 and CoNB10 solids, the HPLC result for the NiNB10 solid remained with unidentified peaks, especially from the region between 16 and 20 min. As expressed on Figure 5.64, another special region on NiNB10 sample was from 23 to 25 min. Then, the support of niobium oxide could have influenced the formation of those products. Indeed, Gnanakumar *et al.* (2019) related that a 40 wt.%Ni/Nb_2O_5 catalyst was practically a Lewis catalyst, which could increase the formation of soluble products from XYL.

Figure 5.64: Chromatogram at HPLC of the reaction system after 6 h of reaction with NiNB10 catalyst.

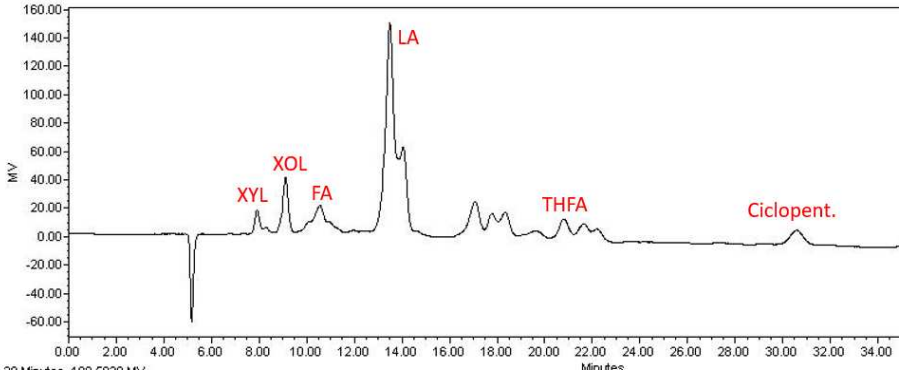

Conversely to CoNBAc10, the NiNBAc10 solid produced less hydrogenation products, as exposed from Figures 5.65 to 5.67.

Figure 5.65: PEN conversion, FA, FUR and THFA selectivity - NiNBAc10.

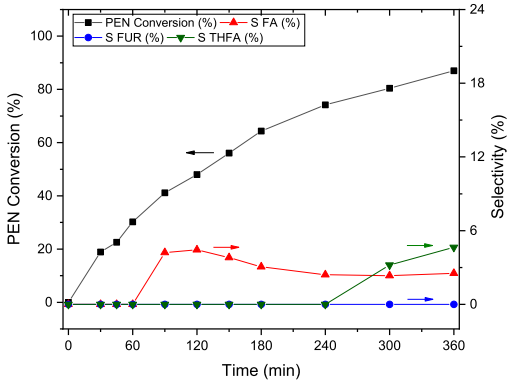

Figure 5.66: Selectivity to XOL, LA, CPO and GVL - NiNBAc10.

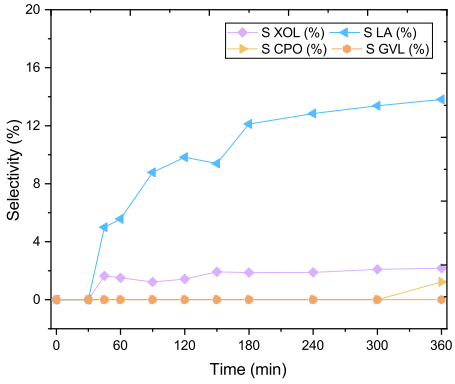

Figure 5.67: Carbon balance - NiNBAc10.

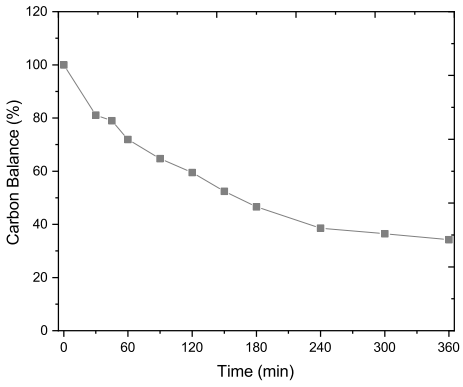

On Figure 5.65, the final PEN conversion was 87%, *ca.* 10% less than NiNB10. However, low contents of FA and THFA were reported on Figure 5.66, with 3% and 5%

respectively. Furthermore, the final selectivities for XOL, LA and CPO had also reduced with acid treatment - 2%, 14% and 1% each. Finally, even with less PEN conversion, the carbon balance did not show improvements - 34% on Figure 5.67. Then, the influence of the acid treatment on Ni catalysts should be studied.

As a remark, the HPLC of NiNBAc10 still presented unidentified products from 14 to 23 min region, as observed over the NiNB10 reaction. The Figure 5.68 also reported larger peaks from XYL, which detoned lower conversions and lower intensity peaks of FA and THFA, in accordance with the reduced formation of hydrogenation products.

Figure 5.68: Chromatogram at HPLC of the reaction system after 6 h of reaction with NiNBAc10 catalyst.

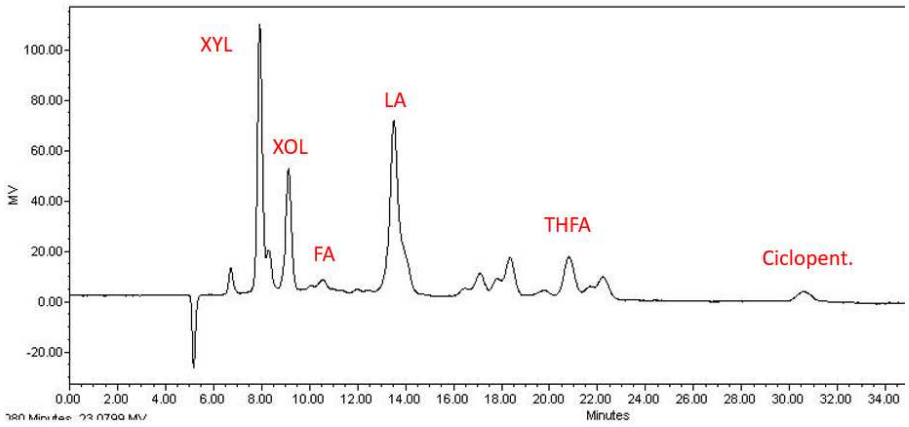

Compared to NiNB10 solids, there were presence of Ni, NiO and Nb_2O_5 on surface. The major differences of NiNBAc10 relied on the incorporation of P groups on surface and the amorphous structure. Recently, Gao *et al.* (2021) studied the effects of P on a Ni/Al_2O_3 catalyst for an oriented CPO synthesis from FUR. The research pointed out that the order of impregnation of Ni and P were crucial for FUR reactions. When P was added after the Ni impregnation, the catalyst inhibited the metal activity for hydrogenation, *i.e.* because the method had modified the distribution of acidity and it had produced NiP (nickel phosphides). Therefore, as the acid treatment was separated of metal loading, this could be a possible reason for the reduced selectivity of FA, THFA, LA and XOL.

The list of Figures 5.69 to 5.71 provided the conversion, selectivities and carbon balance profiles for RuNB05 solid. On Figure 5.69, after 150 min of reaction, the PEN conversion was 99%, providing the highest value of all catalysts. Besides, the FA selectivity reached a peak of 65% on 30 min, decreasing to *ca.* 17% at the end of reaction. On the

contrary, the THFA reached 20% on 60 min, reaching the same value at the end of reaction. No FUR was detected on reaction.

Figure 5.69: PEN conversion, FA, FUR and THFA selectivity - RuNB05.

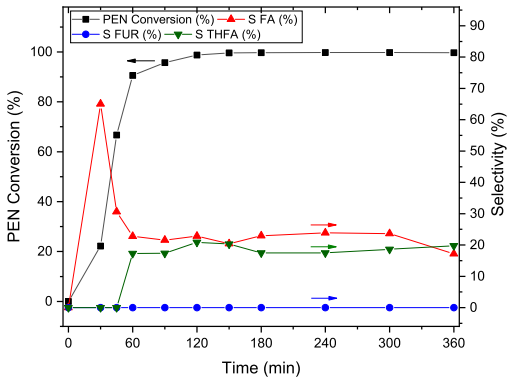

Figure 5.70: Selectivity to XOL, LA, CPO and GVL - RuNB05.

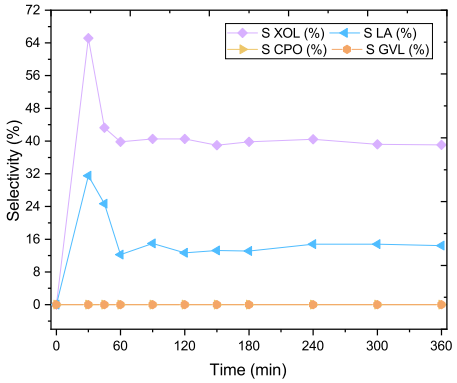

Figure 5.71: Carbon balance - RuNB05.

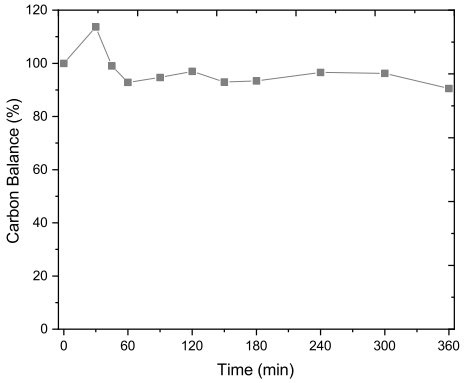

The Figure 5.70 also displayed a considerable LA and XOL selectivity on 30 min - 65% and 31% respectively. Conversely to FA profile, both substances had presented a sharp decrease on the selectivity, with 39% and 14% for each. However, those reductions on selectivity did not damage the carbon balance on Figure 5.71, once it was 90% at the end of reaction, the highest value among the studied catalysts. (Ramirez-Barria *et al.*, 2018) reported that the use of $RuCl_3$ as precursor did not reduced the PEN conversion or FUR hydrogenation, in agreement with our results.

One possible reason for the direct hydrogenation products, as XOL, is the reduced area of the RuNB05 catalyst. This sample presented the lowest value of superficial area - 25 m^2/g, then, most of the reactions might take place on catalyst surface. Besides, the H_2 activation on 400 °C might had induced an excess of metal sites on catalytic

surface, producing direct hydrogenation routes.

The Figure 5.72 provided a HPLC result after 6 h for the RuNB05 solid. Compared to the other chromatograms, the trend for the formation of hydrogenation products (XOL, FA, LA and THFA) was confirmed. Also, the content of unidentified peaks was lower, in agreement with the 90% of carbon balance at the end of the reaction.

Figure 5.72: Chromatogram at HPLC of the reaction system after 6 h of reaction with RuNB05 catalyst.

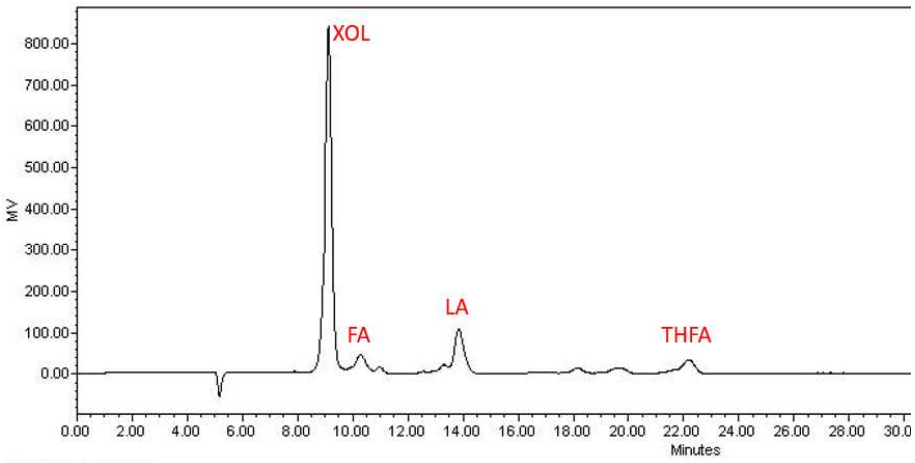

Several researches had studied the XYL and FUR aqueous hydrogenation using Ru catalysts. Ramirez-Barria *et al.* (2018) cited that the FUR reduction on water is damaged due to low solubility of H_2 and bonds H_2O-Ru, changing the H_2 coverage on catalyst surface. At the same time, temperatures above 100°C could shift the transformation of FA into THFA, CPO and 1,5-pentanediol (Ramirez-Barria *et al.*, 2018). As no CPO was identified on reaction and the XPS analysis showed Ru on RuNB05 surface, it could draw some conclusions about the a total FUR hydrogenation.

Delbecq and Sautet (1995) reported that a large band of d-orbital caused an electronic attraction of C=C bond, inducing also partial hydrogenation. However, metal sites of Ru contain a reduced d-band, curbing partial reduction and causing a total hydrogenation (Musci *et al.*, 2017). One solution reported was the use of a base metal - Sn or Co - to stretch this band and to change the adsorption mode (Musci *et al.*, 2017). Then, this could explain the production of THFA and LA on RuNB05 reaction.

It was also reported that metal Ru is the central site for XYL hydrogenation to XOL. In addition, the LAS sites could induce to XOL selectivity (Mishra *et al.*, 2013). So, the presence of Ru and niobia could explain the elevated XOL selectivity at 30 min

of reaction. Furthermore, the XYL hydrogenation to XOL on water produced arabitol (a side-product from XOL hydrogenation) on temperatures above 100 °C. Therefore, the arabitol may be one of the products of RuNB05.

To summarize the RuNB05 analysis, some researches had pointed out the loss of activity of Ru catalysts after FUR hydrogenation. Musci *et al.* (2017) cited the resin formation on catalyst surface and Ramirez-Barria *et al.* (2018) demonstrated the adsorption of FA on catalyst due to increase of oxygen content - RuO_2 formation. Then, the oxophilicity of Ru might have produced Ru oxides after the reaction cycle.

The Figures 5.73 to 5.75 showed that the acid treatment had caused differences on RuNBAc05 catalytic performance.

Figure 5.73: PEN conversion, FA, FUR and THFA selectivity - RuNBAc05.

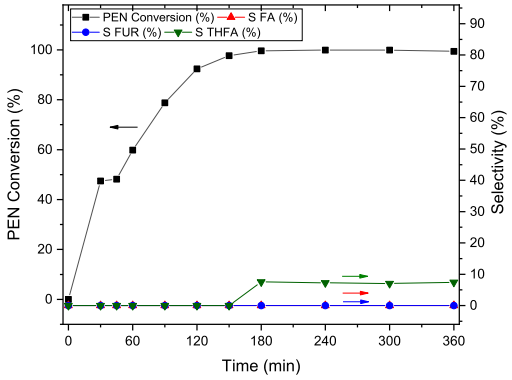

Figure 5.74: Selectivity to XOL, LA, CPO and GVL - RuNBAc05.

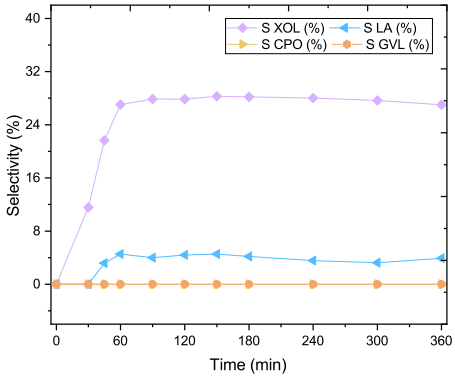

Figure 5.75: Carbon balance - RuNBAc05.

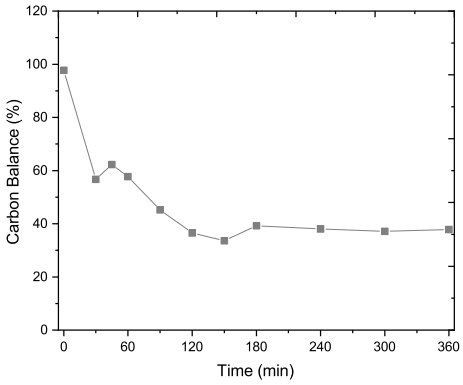

Despite the elevated PEN conversion - *ca.* 99% - the selectivity of FA, THFA, XOL and LA were modified. On Figure 5.74, no FA was produced, though the final selectivity of THFA was 8%. Furthermore, the XOL selectivity was maintained at 28%

from 60 to 360 min. At the same time, the LA selectivity was 4%. Those reduced selectivities had curbed the final carbon balance to 38%, as expressed on Figure 5.75. Then, there were influences of the acid treatment on the Ru based catalyst.

The HPLC result of the RuNBAc05 reaction after 6 h also showed reduced peaks for LA and THFA - Figure 5.76. Neither FUR nor FA were detected on the peaks. In addition, compared to RuNB05, the carbon balance was reduced from 91% to 31%, then the formation of other products that could not be identified might have occurred.

Figure 5.76: Chromatogram at HPLC of the reaction system after 6 h of reaction with RuNBAc05 catalyst.

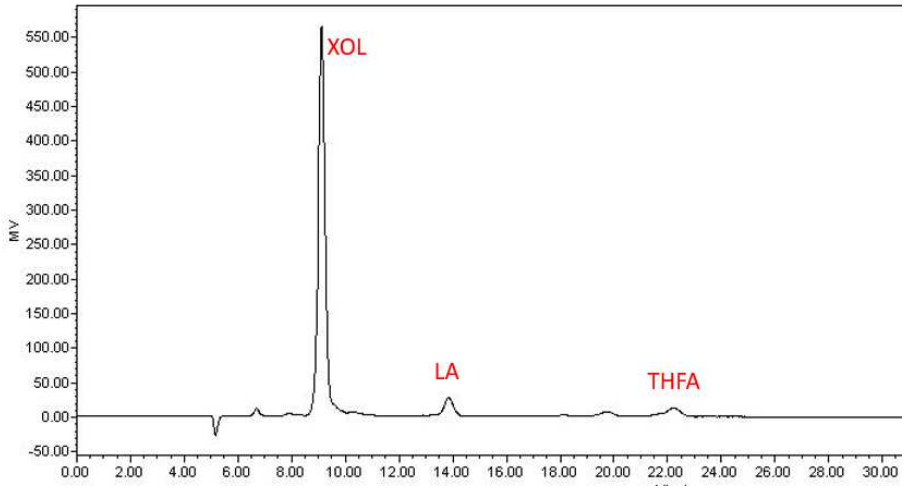

The recent results of Fovanna *et al.* (2020) showed the influence of the incorporation of P on Ru/Al_2O_3 catalysts. On FUR reduction to FA, the FA yield was reduced from 77% to 65%. According to them, the treatment had increased the content of BAS on samples, which generated co-products with FUR. Furthermore, the presence of P promoted the coexistence of Ru-RuO_x on surface decreasing, then, the hydrogenation route. However, there were not indications about the influence of P loading on catalysts. All in one, conversely to CoNBAc10 and NiNBAc10, the acid treatment attenuated the selectivity to hydrogenation products.

To sum up, the Tables 5.12 and 5.13 of this section summarized all results for PEN conversion, selectivities and yields of out eight studied catalysts. It should be pointed out that the acid treatment decreased the production of products concerning to FUR and further hydrogenation.

Table 5.12: Summary of catalyst performance - PEN conversions (%), selectivities (%) and carbon balance (%) after 360 min.

Catalyst	X_{PEN}	S_{FA}	S_{THFA}	S_{FUR}	S_{XOL}	S_{LA}	S_{CPO}	S_{GVL}	CB
NB400	93	3	0	16	0	0	0	0	25
NBAc400	71	0	0	45	0	0	0	0	61
CoNB10	99	14	5	5	0	1	1	0	27
CoNBAc10	90	9	3	11	0	1	0	0	32
NiNB10	98	16	6	0	2	16	3	0	45
NiNBAc10	87	3	5	0	2	14	1	0	34
RuNB05	99	17	20	0	39	14	0	0	91
RuNBAc05	99	0	8	0	27	4	0	0	38

Table 5.13: Summary of catalyst performance - yields to products(%) after 360 min.

Catalyst	Y_{FA}	Y_{THFA}	Y_{FUR}	Y_{XOL}	Y_{LA}	Y_{CPO}	Y_{GVL}	CB
NB400	3	0	16	0	0	0	0	25
NBAc400	0	0	32	0	0	0	0	61
CoNB10	14	5	5	0	1	1	0	27
CoNBAc10	8	3	10	0	1	0	0	32
NiNB10	16	6	0	2	16	3	0	45
NiNBAc10	2	4	0	2	13	1	0	34
RuNB05	17	20	0	39	14	0	0	91
RuNBAc05	0	8	0	27	4	0	0	38

Furthermore, the RuNB05 solid was compared to similar works on literature concerning to FA production on Table 5.14. It should be pointed out that even though our research used only water as solvent, the results of FA yield were close to the literature. Besides, the majority of works studied noble metals, due to higher hydrogenation capacity and isopropanol as co-solvent, in order to solubilize FUR and prevent side reactions (Hu *et al.*, 2014).

Table 5.14: Comparison of RuNB05 to researches on direct FA production from XYL.

Catalyst/ Support	T (°C)	pH_2 (bar)	Solv.	Co-solv.	Yield (%)			Reference
					FA	THFA	XOL	
Ru/Nb_2O_5	160	50	H_2O	-	17	20	39	This work
Ru/C	165	25	CHE	H_2O	1	21	1	Ordomsky *et al.* (2013a)
Pt/SiO_2*	170	-	H_2O	IPA	12	n.r.	2	Perez and Fraga (2014)
Pt/SBA-15**	130	30	H_2O	IPA	47	n.r.	5	Canhaci *et al.* (2017)
(Al)-SBA-15	150	-	H_2O	IPA	13	n.r.	n.r.	Perez *et al.* (2019)
Cu/SBA-15*	130	30	H_2O	BUT	60	n.r.	4	Deng *et al.* (2020)

*: mixed with ZrO_2-SO_4, **: sulfonated SBA-15, CHE: cyclohexene, IPA: isopropanol, BUT: 1-butanol, n.r.: not reported, -: N_2 was used instead of H_2.

5.2.2 Leaching - Metal Catalysts

The liquid phase reactions provide several issues about metal leaching on the catalysts, once water is a polar and abrasive medium. Therefore, the heterogeneous catalysis over water remains as a challenge, especially for base metals, like Mo, Co and Ni (Vemic, 2015). The Figures 5.77 and 5.78 provided the results of EDX before and after one reaction cycle.

Figure 5.77: EDX - Metal content before and after the reaction (CoNB10, NiNB10 and RuNB05).

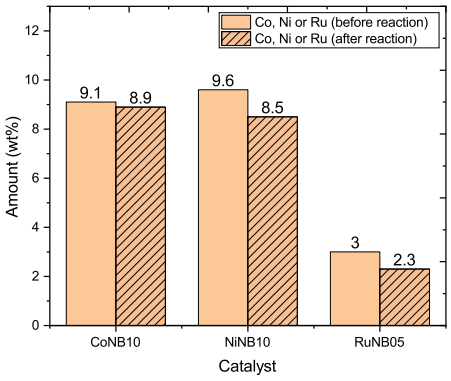

Figure 5.78: EDX - Metal and P contents before and after the reaction (CoNBAc10, NiNBAc10 and RuNBAc05).

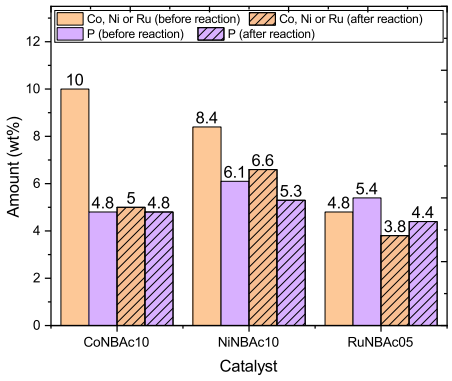

The Figure 5.77 reported little modifications on Co loading after the reaction (9.1% vs 8.9%). On the contrary, both Ni and Ru contents were decreased after only one

reaction. The Ni amount was reduced from 9.6% to 8.5%, whereas Ru was curbed from 3.0% to 2.3%. Those values had represented a loss of 11% and 23%, respectively. Then, an evident leaching of Ni and Ru took place on NiNB10 and RuNB05 solids.

Nakagawa and Tomishige (2010) related Ni leaching on a bimetallic Ni-Pd/SiO_2 catalyst on water on 5-HMF hydrogenation. They reported the low interaction of Ni oxides on acid medium as a possible reason. Piskun *et al.* (2016) pointed out a minor Ru leaching on Ru/C solid on LA hydrogenation on water due to increased particle sizes. So, the existence of metal sites on NiNB10 and RuNB05 could have provided an active phase leaching on water.

On Figure 5.78, it was noted that the acid treatment also changed the catalyst leaching. The Co content was reduced from 10 wt% to 5 wt% - almost 50% of loss. A similar trend took place on Ni and Ru. The NiNBAc10 solid reduced the Ni amount from 8.4 to 6.6 wt%, a reduction of 20%. Besides, the similar 20% decrement on Ru amount was reported on RuNBAc05 - 4.8 to 3.8 wt%. Therefore, there was some influence of P incorporation into metal losses. However, our acid treatment showed opposite trends related the literature. Their Ru impregnation on P-Al_2O_3 improved metal dispersion and also had strengthened the interaction between Ru and alumina. By contrast, not only the metal content had decreased, but also the P amount on NiNBAc10 and RuNBAc05 - 11 and 18 wt% respectively.

Nakagawa and Tomishige (2010) and Vemic (2015) also pointed out the elevated acidity as an issue for catalysts leaching. However, the elevated acidity could be provided due to leaching of P groups or the formation of acid products from acid treatment that changed the acid medium. Therefore, regarding to acid treatment on niobia, it had not improved the catalyst stability after the cycles.

5.3 Concluding Remarks - Characterizations/Results and Discussions

- The IWI method curbed the superficial area of the catalysts. For example, as the support NB400 presented 120 m^2/g of area, the RuNB05 solid had only 25 m^2/g, more than 60% of area loss. On the contrary, the metals supported on acid support NBAc400 increased their areas, probably due to a reorganization of catalyst surface.

The H_2 activation procedure after the IWI probably had produced new pores on the previous collapsed ones.

- Aside for the RuNB05 catalyst, the SEM/EDX results showed that the active phase content was close to the nominal values. Furthermore, there was detection of P on acid treatment, showing that P groups had resisted to calcination and H_2 activation steps.

- Except for the NiNB10 solid, all other catalysts had low crystalline contents, once the crystallization temperature of the NB400 support is 500 °C and the calcination took place at 400 °C. Concerning to NiNB10, the literature previuosly reported that elevated Ni contents on Nb_2O_5 had induced to both metal and support crystallization. In addition, the acid treamtment had modified the crystallization events, once the NiNBAc10 solid only had Ni events and no niobia events.

- The TPR outcomes demonstrated several differences between the solids with or without acid treatment. The P-modified catalysts CoNBAc10, NiNBAc10 and RuNBAc05 had lower H_2 uptakes related to the non-modified ones, with differences up to 50% in the case of CoNBAc10. Then, the acid treatment could have changed the catalyst surface, curbing the activation of metals particles. Furthermore, most H_2 intakes were about 50% compared to the theoretical value. It could be an indication of low metal exposure on those catalysts. So, the IWI could reduce the catalyst area, and also difficult further reduction of metals compared to other methods of impregnation.

- In accordance with EDX, the XPS results presented P on the samples with acid treatment. The researched articles reported that those groups could be phosphate and/or phosphides. Concerning to Co based-catalysts, both Co solids showed a majority of oxides on their surfaces - CoO and Co_3O_4, probably because the reduction temperature was lower than the Co^0 formation. The Ni solids had NiO and Ni^0 particles, contributing to the existence of metal sites. And the Ru solids only presented Ru^0 sites after the activation on H_2 flow. Nonetheless, those results were prior to the reaction because the water medium could modify catalyst structure.

- The support NBAc400 had 63% of medium sites, whereas the NB400 had 50%.

So, the acid treatment changed not only the surface but also the strength of sites on catalysts. However, all the metal catalysts presented events with NH_3 molecule after 400 °C, like strong adsorption (Co) or even NH_3 decomposition (Ni and Ru). Besides, it was not possible to determine whether those desorptions occurred due to decompostion or even P groups releasing of acid treatment. Then, it was not possible to assign the existence of strong sites on those solids.

- Comparing NB400 and NBAc400 reactions, the influence of acid treatment was noted. The FUR yield after 6 h was 16% and 32%, respectively. So, the acid treatment had influenced the catalyst performance. The Co solids produced FA with 14% and 8% of yield each, also with FUR production. However, no FUR was detected on Ni and Ru catalysts. On the contrary, there was notable XOL production on Ru catalysts, probably due to the presence of metal sites. Especially on RuNB05, the final XOL yield was 39% as XYL solubility on water was higher than FUR. Furthermore, on the acid-treated solids, less production of FUR hydrogenated compounds was related. Then, the acid treatment on the concentration of 1 mol/L decreased the PEN conversion and the selectivity to hydrogenation products.

- Even after only 1 cycle of reaction, some catalysts samples showed metal leaching. In fact, the catalysts with acid treatment (CoNBAc10, NiNBAc10 and RuNBAc05) had the highest metal leachings - up tp 50 wt.% of active phase on CoNBAc10. Two possible causes were related: the incorporation of P weakened the interaction between metals and acid-niobia and/or the leaching of P increased the acidity of medium dissolving the metals. Even though it was not possible to conclude the determinant reason for that, it was demonstrated the acid treatment reduced the stability of our solids after the reaction.

Chapter 6

Conclusions and Suggestions for Future Works

6.1 Conclusions

The results presented on our work demonstrated that all metal supported niobia based catalysts were active both for xylose dehydration and furfural hydrogenation into several products, like furfuryl alcohol (FA), levulinic acid (LA) and so on. Moreover, the influence of a P-based acid treatment on niobia support was also studied.

The incipient wetness impregnation led to reduced areas on non-treated solids, due to higher diffusion and obstruction of catalyst pores. Besides, all catalysts were non-crystalline, except for NiNB10 solid, which presented and event of support and metal crystallization because of the interference of Ni on niobia. Furthermore, the TPR and XPS results showed low possibility of reductions for Co and Ni at 400 °C, leading to an increased portion of oxides on catalyst surface. During the reactions, the three solids (CoNB10, NiNB10 and RuNB05) produced FA after 6 h (*ca.* 15% of selectivity). However, on CoNB10 a final FUR selectivity of 5% was reported, which was not found on NiNB10 and RuNB05, probably due to the presence of metal sites. One possible reason was that even the existence of Co oxides on surface could catalyze the FUR further conversions. In addition, the NiNB10 and RuNB05 solid also produced LA and XOL. The first had 16% and 2% on final selectivities, and the second had 14% and 39%. Then, those catalysts were more pronounced to synthesis of further hydrogenation products, probably due to a higher content of metal sites. However, aside from the RuNB05 catalyst, the Co and Ni solids did not have suitable values for carbon balance, with 27% and 45%, respectively. On those situations, we could point out several causes for those decrements: the production of humins, the production of non-identifed products on HPLC analyses and even the formation FA resins. In addition, the calcined niobia support could also had generated XYL isomers, which were not accounted on the HPLC results.

Concerning to P-modified solids, some differences were noted on characterizations and reaction results. The support NBAc400 was more selective to FUR, with 32% of yield instead of 16% of NB400. So, at least on support, the acid treatment induced

an oriented production of FUR. However, the acid treatment did not improve the performance of metallic phases. As example, despite the higher areas, the FA yield was reduced on all solids - CoNBAc10, NiNBAc10 and RuNBAc05. Indeed, the CoNBAc10 provided only 8% of FA yield (almost 50% less than the non treated catalyst), NiNBAc10 had only 2% of FA yield (on NiNB10 it was 16%) and RuNBAc05 did not produce FA. Therefore, the acid treatment did not transform those solids into a bifunctional performance, *i.e.*, to shift XYL conversion into FUR without damaging hydrogenation route. On the contrary, it was noted that the selectivity and yields of FUR hydrogenation products were reduced with that feature. Several causes might be related to the loss of performance: the incorporation of potential BAS changed the energy barrier for hydrogenation, the formation of phosphides on catalysts during reduction and even the steric hindrance on surface. However, for a more precise conclusion, further analyses are required.

The leaching experiments also demonstrated that the acid treatment did not improve the metal stability after one cycle of reaction. On NiNBAc10 and RuNBAc05, a metal leaching of almost 30% was detected, and also a P loss of 20%. Therefore, the inclusion of P groups on the concentration of our study has damaged the catalysts reuse.

6.2 Suggestions for Future Works

During this work, we hope to reach some insights about the lignolcelluosic biomass conversion. We have seen that the XYL conversion to FA was not easy, and that our catalyst need to de designed with a balance of acid and metal sites. Furthermore, the concentration of 1 mol/L of the acid treatment was not suitable for the direct conversion, but other concentrations might be studied. Therefore, we propose suggestions for future works in this research field.

- Reuse of catalysts on reactions.
- Investigation of acid treatment on different concentrations.
- Use of bimetallic combinations: Co-Ru, Ni-Ru and Ni-Co.

References

ADKINS, H. and CONNOR, R. Method of hydrogenation of furfural to furfuryl alcohol. United states patent office n. 2,094,975, The Quaker Oats Company, October 1937.

AGUIAR, M.M.; FERREIRA, L.F.R. and MONTEIRO, R.T.R. Use of vinasse and sugarcane bagasse for the production of enzymes by lignocellulolytic fungi. **Brazilian Archives of Biology and Technology**, v. 53, n. 5, 1245–1254, 2010.

AHMAD, T.; KENNE, L.; OLSSON, K. and THEANDER, O. The formation of 2-furaldehyde and formic acid from pentoses in slightly acidic deuterium oxide studied by 1h nmr spectroscopy. **Carbohydrate research**, v. 276, n. 2, 309–320, 1995.

ALBILALI, R.; DOUTHWAITE, M.; HE, Q. and TAYLOR, S.H. The selective hydrogenation of furfural over supported palladium nanoparticle catalysts prepared by sol-immobilisation: effect of catalyst support and reaction conditions. **Catalysis Science & Technology**, v. 8, n. 1, 252–267, 2018.

ALDOSARI, O.F.; IQBAL, S.; MIEDZIAK, P.J.; BRETT, G.L.; JONES, D.R.; LIU, X.; EDWARDS, J.K.; MORGAN, D.J.; KNIGHT, D.K. and HUTCHINGS, G.J. Pd-ru/tio2 catalyst–an active and selective catalyst for furfural hydrogenation. **Catalysis Science & Technology**, v. 6, n. 1, 234–242, 2016.

ANTAL JR, M.J.; LEESOMBOON, T.; MOK, W.S. and RICHARDS, G.N. Mechanism of formation of 2-furaldehyde from d-xylose. **Carbohydrate Research**, v. 217, 71–85, 1991.

AUDEMAR, M.; CIOTONEA, C.; DE OLIVEIRA VIGIER, K.; ROYER, S.; UNGUREANU, A.; DRAGOI, B.; DUMITRIU, E. and JÉRÔME, F. Selective hydrogenation of furfural to furfuryl alcohol in the presence of a recyclable cobalt/sba-15 catalyst. **ChemSusChem**, v. 8, n. 11, 1885–1891, 2015.

AUDEMAR, M.; WANG, Y.; ZHAO, D.; ROYER, S.; JÉRÔME, F.; LEN, C. and DE OLIVEIRA VIGIER, K. Synthesis of furfuryl alcohol from furfural: A comparison between batch and continuous flow reactors. **Energies**, v. 13, n. 4, 1002, 2020.

BAJWA, D.S.; PETERSON, T.; SHARMA, N.; SHOJAEIARANI, J. and BAJWA, S.G. A review of densified solid biomass for energy production. **Renewable and Sustainable Energy Reviews**, v. 96, 296–305, 2018.

BARRIOS, A.M.; TELES, C.A.; DE SOUZA, P.M.; RABELO-NETO, R.C.; JACOBS, G.; DAVIS, B.H.; BORGES, L.E. and NORONHA, F.B. Hydrodeoxygenation of phenol over niobia supported pd catalyst. **Catalysis Today**, v. 302, 115–124, 2018.

BHAUMIK, P. and DHEPE, P.L. Solid acid catalyzed synthesis of furans from carbohydrates. **Catalysis Reviews**, v. 58, n. 1, 36–112, 2016.

BHAUMIK, P. and DHEPE, P.L. From lignocellulosic biomass to furfural: insight into the active species of a silica-supported tungsten oxide catalyst. **ChemCatChem**, v. 9, n. 14, 2709–2716, 2017.

BHOGESWARARAO, S. and SRINIVAS, D. Catalytic conversion of furfural to industrial chemicals over supported pt and pd catalysts. **Journal of Catalysis**, v. 327, 65–77, 2015.

BIRADAR, N.; HENGNE, A.; SAKATE, S.; SWAMI, R. and RODE, C. Single pot transfer hydrogenation and aldolization of furfural over metal oxide catalysts. **Catalysis Letters**, v. 146, n. 8, 1611–1619, 2016.

BP. **BP Energy Outlook 2019 Edition The Energy Outlook Explores the Forces Shaping the Global Energy Transition out to 2040 and the Key Uncertainties Surrounding That**. BP, England, 2019.

BRANDÃO, R.F.; QUIRINO, R.L.; MELLO, V.M.; TAVARES, A.P.; PERES, A.C.;

GUINHOS, F.; RUBIM, J.C. and SUAREZ, P.A. Synthesis, characterization and use of nb2o5 based catalysts in producing biofuels by transesterification, esterification and pyrolysis. **Journal of the Brazilian Chemical Society**, v. 20, n. 5, 954–966, 2009.

BROWNLEE, H.J. Process for manufacturing furfural. United states patent office n. 1,919,878, The Quaker Oats Company, July 1933a.

BROWNLEE, H.J. Process for manufacturing furfural. United states patent office n. 1,919,877, The Quaker Oats Company, July 1933b.

BROWNLEE, H.J. Process for producing furfural. United states patent office n. 2,140,572, The Quaker Oats Company, June 1938.

BRUCE, S.M.; ZONG, Z.; CHATZIDIMITRIOU, A.; AVCI, L.E.; BOND, J.Q.; CARREON, M.A. and WETTSTEIN, S.G. Small pore zeolite catalysts for furfural synthesis from xylose and switchgrass in a γ-valerolactone/water solvent. **Journal of molecular catalysis a: chemical**, v. 422, 18–22, 2016.

BURKET, C. and SABESAN, S. Process for furfural production from biomass. United states patent us 8,524,924 b2, E I du Pont de Nemours and Company, September 2015.

CAMPOS-MOLINA, M.J.; CORRAL-PÉREZ, J.J.; MARISCAL, R. and GRANADOS, M.L. Silica-poly (styrenesulphonic acid) nanocomposites as promising acid catalysts. **Catalysis Today**, v. 279, 155–163, 2017.

CANHACI, S.J.; PEREZ, R.F.; BORGES, L.E. and FRAGA, M.A. Direct conversion of xylose to furfuryl alcohol on single organic–inorganic hybrid mesoporous silica-supported catalysts. **Applied Catalysis B: Environmental**, v. 207, 279–285, 2017.

CARNITI, P.; GERVASINI, A.; BIELLA, S. and AUROUX, A. Niobic acid and niobium phosphate as highly acidic viable catalysts in aqueous medium: Fructose dehydration

reaction. **Catalysis Today**, v. 118, n. 3-4, 373–378, 2006.

CEPEDA, E.A.; CALVO, B.; SIERRA, I. and IRIARTE-VELASCO, U. Selective hydrogenation of sunflower oil over ni catalysts. **Korean Journal of Chemical Engineering**, v. 33, n. 1, 80–89, 2016.

CHAN, X.; PU, T.; CHEN, X.; JAMES, A.; LEE, J.; PARISE, J.B.; KIM, D.H. and KIM, T. Effect of niobium oxide phase on the furfuryl alcohol dehydration. **Catalysis Communications**, v. 97, 65–69, 2017.

CHARY, K.V.; LAKSHMI, K.S.; RAO, P.V.R.; RAO, K.S.R. and PAPADAKI, M. Characterization and catalytic properties of niobia supported nickel catalysts in the hydrodechlorination of 1, 2, 4-trichlorobenzene. **Journal of Molecular Catalysis A: Chemical**, v. 223, n. 1-2, 353–361, 2004.

CHARY, K.V.; SRIKANTH, C.S. and RAO, V.V. Characterization and reactivity of nb2o5 supported ru catalysts. **Catalysis Communications**, v. 10, n. 5, 459–463, 2009.

CHATTERJEE, A.; HU, X. and LAM, F.L.Y. Towards a recyclable mof catalyst for efficient production of furfural. **Catalysis Today**, v. 314, 129–136, 2018.

CHEN, S.; WOJCIESZAK, R.; DUMEIGNIL, F.; MARCEAU, E. and ROYER, S. How catalysts and experimental conditions determine the selective hydroconversion of furfural and 5-hydroxymethylfurfural. **Chemical Reviews**, v. 118, n. 22, 11023–11117, 2018.

CHEN, X.; ZHANG, L.; ZHANG, B.; GUO, X. and MU, X. Highly selective hydrogenation of furfural to furfuryl alcohol over pt nanoparticles supported on gc3n4 nanosheets catalysts in water. **Scientific reports**, v. 6, n. 1, 1–13, 2016.

CHOUDHARY, V.; PINAR, A.B.; SANDLER, S.I.; VLACHOS, D.G. and LOBO, R.F. Xylose isomerization to xylulose and its dehydration to furfural in aqueous media. **Acs**

Catalysis, v. 1, n. 12, 1724–1728, 2011.

CHOUDHARY, V.; SANDLER, S.I. and VLACHOS, D.G. Xylose isomerization to xylulose and its dehydration to furfural in aqueous media. **Acs Catalysis**, v. 2, n. 12, 2022–2028, 2012.

COSTA, M. M. **Emprego da Nióbia como Suporte em Catalisadores para Hidrogenação de Furfural a Álcool Furfurílico em Fase Líquida**. 2021. Dissertation (Mastering). Universidade Estadual de Campinas, Campinas.

CUI, J.; TAN, J.; CUI, X.; ZHU, Y.; DENG, T.; DING, G. and LI, Y. Conversion of xylose to furfuryl alcohol and 2-methylfuran in a continuous fixed-bed reactor. **ChemSusChem**, v. 9, n. 11, 1259–1262, 2016.

DA COSTA, R.M.; PATTATHIL, S.; AVCI, U.; WINTERS, A.; HAHN, M.G. and BOSCH, M. Desirable plant cell wall traits for higher-quality miscanthus lignocellulosic biomass. **Biotechnology for biofuels**, v. 12, n. 1, 1–18, 2019.

DA SQ MENEZES, J.P.; DUARTE, K.R.; MANFRO, R.L. and SOUZA, M.M. Effect of niobia addition on cobalt catalysts supported on alumina for glycerol steam reforming. **Renewable Energy**, v. 148, 864–875, 2020.

DALVAND, K.; RUBIN, J.; GUNUKULA, S.; WHEELER, M.C. and HUNT, G. Economics of biofuels: Market potential of furfural and its derivatives. **Biomass and Bioenergy**, v. 115, 56–63, 2018.

DANON, B.; MARCOTULLIO, G. and DE JONG, W. Mechanistic and kinetic aspects of pentose dehydration towards furfural in aqueous media employing homogeneous catalysis. **Green Chemistry**, v. 16, n. 1, 39–54, 2014.

DASHTBAN, M.; GILBERT, A. and FATEHI, P. Production of furfural: overview and

challenges. **J. Sci. Technol. Forest Prod. Process**, v. 2, n. 4, 44–53, 2012.

DE CARVALHO, R.S.; RODRIGUES, F.D.A.; MONTEIRO, R.S. and DA SILVA FARIA, W.L. Optimization of furfural synthesis from xylose using niobic acid and niobium phosphate as catalysts. **Waste and Biomass Valorization**, v. 10, n. 9, 2673–2680, 2019.

DE JONG, K.P. **Synthesis of solid catalysts**. John Wiley & Sons, 2009.

DE LIMA, Letícia Franzo. **Efeitos de Tratamentos Ácidos Aplicados a Catalisadores à Base de Nióbia sobre o Desempenho Catalítico na Reação de Desidratação da Xilose a Furfural em Fase Líquida**. 2020. Thesis (Doctorate). Universidade Estadual de Campinas, Campinas.

DE LIMA, L.F.; LIMA, J.L.M.; JORQUEIRA, D.S.S.; LANDERS, R.; MOYA, S.F. and SUPPINO, R.S. Use of amorphous nb2o5 and nb2o5/al2o3 as acid catalysts for the dehydration of xylose to furfural. **Reaction Kinetics, Mechanisms and Catalysis**, v. 132, n. 1, 73–92, 2021.

DE PIETRE, M.; ALMEIDA, L.; LANDERS, R.; VINHAS, R. and LUNA, F. H3po4-and h2so4-treated niobic acid as heterogeneous catalyst for methyl ester production. **Reaction Kinetics, Mechanisms and Catalysis**, v. 99, n. 2, 269–280, 2010.

DE SOUSA, L.F.; TONIOLO, F.S.; LANDI, S.M. and SCHMAL, M. Investigation of structures and metallic environment of the ni/nb2o5 by different in situ treatments–effect on the partial oxidation of methane. **Applied Catalysis A: General**, v. 537, 100–110, 2017.

DELBECQ, F. and SAUTET, P. Competitive c=c and c=o adsorption of α-β-unsaturated aldehydes on pt and pd surfaces in relation with the selectivity of hydrogenation reactions: A theoretical approach. **Journal of Catalysis**, v. 152, n. 2, 217–236, 1995.

DELBECQ, F.; WANG, Y.; MURALIDHARA, A.; EL OUARDI, K.; MARLAIR, G. and LEN, C. Hydrolysis of hemicellulose and derivatives—a review of recent advances in the production of furfural. **Frontiers in chemistry**, v. 6, 146, 2018.

DENG, T.; XU, G. and FU, Y. One-pot cascade conversion of xylose to furfuryl alcohol over a bifunctional cu/sba-15-so3h catalyst. **Chinese Journal of Catalysis**, v. 41, n. 3, 404–414, 2020.

DEWANGAN, N.; ASHOK, J.; SETHIA, M.; DAS, S.; PATI, S.; KUS, H. and KAWI, S. Cobalt-based catalyst supported on different morphologies of alumina for non-oxidative propane dehydrogenation: effect of metal support interaction and lewis acidic sites. **ChemCatChem**, v. 11, n. 19, 4923–4934, 2019.

DOHADE, M. and DHEPE, P. Efficient hydrogenation of concentrated aqueous furfural solutions into furfuryl alcohol under ambient conditions in presence of ptco bimetallic catalyst. **Green Chemistry**, v. 19, n. 4, 1144–1154, 2017.

DOISEAU, Aude-Claire. **Déshydratation Catalytique Du Xylose En Furfural**. 2014. Thesis (Doctorate). Université Claude Bernard - Lyon I, Lyon, France.

DULIE, N.W.; WOLDEYES, B.; DEMSASH, H.D. and JABASINGH, A.S. An insight into the valorization of hemicellulose fraction of biomass into furfural: catalytic conversion and product separation. **Waste and Biomass Valorization**, pp. 1–22, 2020.

DUMESIC, J.; ALONSO, D.M.; BOND, J.Q.; ROOT, T. and CHIA, M. Method to produce, recover and convert furan derivatives from aqueous solutions using alkylphenol extraction. United states patent office n. 8,389,749 b2, Wisconsin Alumni Research Foundation, May 2013.

DURNDELL, L.J.; ZOU, G.; SHANGGUAN, W.; LEE, A.F. and WILSON, K. Structure-reactivity relations in ruthenium catalysed furfural hydrogenation. **ChemCatChem**, v. 11, n. 16, 3927–3932, 2019.

DUTTA, S.; DE, S.; SAHA, B. and ALAM, M.I. Advances in conversion of hemicellulosic biomass to furfural and upgrading to biofuels. **Catalysis Science & Technology**, v. 2, n. 10, 2025–2036, 2012.

DUVAL, A. and LAWOKO, M. A review on lignin-based polymeric, micro-and nano-structured materials. **Reactive and Functional Polymers**, v. 85, 78–96, 2014.

EGAWA, C.; ARUGA, T. and IWASAWA, Y. Epitaxial growth of fe overlayers on the ru (001) surface. **Surface Science**, v. 188, n. 3, 563–574, 1987.

EITELMAN, S.J. and HORTON, D. Studies on enolization of aldehydo-aldose derivatives. **Carbohydrate research**, v. 341, n. 16, 2658–2668, 2006.

ENNAERT, T.; VAN AELST, J.; DIJKMANS, J.; DE CLERCQ, R.; SCHUTYSER, W.; DUSSELIER, M.; VERBOEKEND, D. and SELS, B.F. Potential and challenges of zeolite chemistry in the catalytic conversion of biomass. **Chemical Society Reviews**, v. 45, n. 3, 584–611, 2016.

ENSLOW, K.R. and BELL, A.T. The kinetics of brønsted acid-catalyzed hydrolysis of hemicellulose dissolved in 1-ethyl-3-methylimidazolium chloride. **RSC advances**, v. 2, n. 26, 10028–10036, 2012.

ENSLOW, K.R. and BELL, A.T. The role of metal halides in enhancing the dehydration of xylose to furfural. **ChemCatChem**, v. 7, n. 3, 479–489, 2015.

ERTL, G.; HIERL, R.; KNÖZINGER, H.; THIELE, N. and URBACH, H. Xps study of copper aluminate catalysts. **Applications of Surface Science**, v. 5, n. 1, 49–64, 1980.

ERTL, G.; KNÖZINGER, H. and WEITKAMP, J. **Handbook of Heterogeneous Catalysis**. VCH Weinheim, 2008.

FANG, C.; WU, W.; LI, H.; YANG, T.; ZHAO, W.; ZHONGWEI, W. and YANG, S. Production of bio-based furfural from xylose over a recyclable niobium phosphate (nbopo3) catalyst. **Energy Sources, Part A: Recovery, Utilization, and Environmental Effects**, v. 39, 2072–2077, 2017a.

FANG, W. and RIISAGER, A. Improved catalytic transfer hydrogenation of biomass-derived aldehydes with metal-loaded aluminum phosphate. **ACS Sustainable Chemistry & Engineering**, 2022.

FANG, Z.; SMITH, R.L. and QI, X. **Production of platform chemicals from sustainable resources**. Springer, 2017b.

FILICIOTTO, L.; BALU, A.M.; VAN DER WAAL, J.C. and LUQUE, R. Catalytic insights into the production of biomass-derived side products methyl levulinate, furfural and humins. **Catalysis Today**, v. 302, 2–15, 2018.

FONTAINE, R.; CAILLAT, R.; FEVE, L. and GUITTET, M. Déplacement chimique esca dans la série des oxydes du niobium. **Journal of Electron Spectroscopy and Related Phenomena**, v. 10, n. 4, 349–357, 1977.

FOVANNA, T.; CAMPISI, S.; VILLA, A.; KAMBOLIS, A.; PENG, G.; RENTSCH, D.; KRÖCHER, O.; NACHTEGAAL, M. and FERRI, D. Ruthenium on phosphorous-modified alumina as an effective and stable catalyst for catalytic transfer hydrogenation of furfural. **Rsc Advances**, v. 10, n. 19, 11507–11516, 2020.

FRAGA, M.A. and PEREZ, R.F. Processo de obtenção de Álcool furfurílico por meio de catalisadores multifuncionais. Instituto nacional de propriedade intelectual br 10 2013 025330-8 a2, Instituto Militar de Engenharia e Instituto Nacional de Tecnologia, August 2015.

FRAINIER, L.J. and FINEBERG, H.H. Cooper chromite catalyst for preparation of furfuryl alcohol from furfural. United states patent office n. 4,251,396, Ashland Oil,

February 1981.

FREVEL, L. and RINN, H. Powder diffraction standards for niobium pentoxide and tantalum pentoxide. **Analytical Chemistry**, v. 27, n. 8, 1329–1330, 1955.

FURSTENAU, R.; MCDOUGALL, G. and LANGELL, M. Initial stages of hydrogen reduction of nio (100). **Surface science**, v. 150, n. 1, 55–79, 1985.

GALLO, J.M.R. and TRAPP, M.A. The chemical conversion of biomass-derived saccharides: an overview. **Journal of the Brazilian Chemical Society**, v. 28, n. 9, 1586–1607, 2017.

GAO, G.; SHAO, Y.; GAO, Y.; WEI, T.; GAO, G.; ZHANG, S.; WANG, Y.; CHEN, Q. and HU, X. Synergetic effects of hydrogenation and acidic sites in phosphorus-modified nickel catalysts for the selective conversion of furfural to cyclopentanone. **Catalysis Science & Technology**, v. 11, n. 2, 575–593, 2021.

GAO, Z.; YANG, L.; FAN, G. and LI, F. Promotional role of surface defects on carbon-supported ruthenium-based catalysts in the transfer hydrogenation of furfural. **ChemCatChem**, v. 8, n. 24, 3769–3779, 2016.

GARCíA-SANCHO, C.; RUBIO-CABALLERO, J.; MÉRIDA-ROBLES, J.; MORENO-TOST, R.; SANTAMARíA-GONZÁLEZ, J. and MAIRELES-TORRES, P. Mesoporous nb2o5 as solid acid catalyst for dehydration of d-xylose into furfural. **Catalysis today**, v. 234, 119–124, 2014.

GIORGIANNI, G.; ABATE, S.; CENTI, G.; PERATHONER, S.; VAN BEUZEKOM, S.; SOO-TANG, S.H. and VAN DER WAAL, J.C. Effect of the solvent in enhancing the selectivity to furan derivatives in the catalytic hydrogenation of furfural. **Acs Sustainable Chemistry & Engineering**, v. 6, n. 12, 16235–16247, 2018.

GíRIO, F.M.; FONSECA, C.; CARVALHEIRO, F.; DUARTE, L.C.; MARQUES, S. and BOGEL-ŁUKASIK, R. Hemicelluloses for fuel ethanol: a review. **Bioresource technology**, v. 101, n. 13, 4775–4800, 2010.

GNANAKUMAR, E.S.; CHANDRAN, N.; KOZHEVNIKOV, I.V.; GRAU-ATIENZA, A.; FERNÁNDEZ, E.V.R.; SEPULVEDA-ESCRIBANO, A. and SHIJU, N.R. Highly efficient nickel-niobia composite catalysts for hydrogenation of co2 to methane. **Chemical Engineering Science**, v. 194, 2–9, 2019.

GOLDSMITH, B.R.; PETERS, B.; JOHNSON, J.K.; GATES, B.C. and SCOTT, S.L. Beyond ordered materials: understanding catalytic sites on amorphous solids. **ACS Catalysis**, v. 7, n. 11, 7543–7557, 2017.

GONG, W.; CHEN, C.; WANG, H.; FAN, R.; ZHANG, H.; WANG, G. and ZHAO, H. Sulfonate group modified ni catalyst for highly efficient liquid-phase selective hydrogenation of bio-derived furfural. **Chinese Chemical Letters**, v. 29, n. 11, 1617–1620, 2018a.

GONG, W.; CHEN, C.; ZHANG, H.; WANG, G. and ZHAO, H. In situ synthesis of highly dispersed cu–co bimetallic nanoparticles for tandem hydrogenation/rearrangement of bioderived furfural in aqueous-phase. **ACS Sustainable Chemistry & Engineering**, v. 6, n. 11, 14919–14925, 2018b.

GUO, P.; LIAO, S. and TONG, X. Heterogeneous nickel catalysts derived from 2d metal–organic frameworks for regulating the selectivity of furfural hydrogenation. **ACS omega**, v. 4, n. 26, 21724–21731, 2019.

GUPTA, N.K.; FUKUOKA, A. and NAKAJIMA, K. Amorphous nb2o5 as a selective and reusable catalyst for furfural production from xylose in biphasic water and toluene. **Acs Catalysis**, v. 7, n. 4, 2430–2436, 2017.

HE, J.; SCHILL, L.; YANG, S. and RIISAGER, A. Catalytic transfer hydrogenation of

bio-based furfural with nio nanoparticles. **ACS Sustainable Chemistry & Engineering**, v. 6, n. 12, 17220–17229, 2018.

HE, Y.C.; JIANG, C.X.; CHONG, G.G.; DI, J.H.; WU, Y.F.; WANG, B.Q.; XUE, X.X. and MA, C.L. Chemical-enzymatic conversion of corncob-derived xylose to furfuralcohol by the tandem catalysis with so42-/sno2-kaoline and e. coli cczu-t15 cells in toluene–water media. **Bioresource technology**, v. 245, 841–849, 2017.

HENPRASERTTAE, S. **The Development of Nickel Catalyst for Ammonia Decomposition**. 2018. Thesis (Doctorate). Sirindhorn International Institute of Technology, Thammasat, Tailand.

HRONEC, M. and FULAJTAROVÁ, K. Selective transformation of furfural to cyclopentanone. **Catalysis Communications**, v. 24, 100–104, 2012.

HRONEC, M.; FULAJTAROVÁ, K. and LIPTAJ, T. Effect of catalyst and solvent on the furan ring rearrangement to cyclopentanone. **Applied Catalysis A: General**, v. 437, 104–111, 2012.

HU, F.; WANG, Y.; XU, S.; ZHANG, Z.; CHEN, Y.; FAN, J.; YUAN, H.; GAO, L. and XIAO, G. Efficient and selective ni/al2o3–c catalyst derived from metal–organic frameworks for the hydrogenation of furfural to furfuryl alcohol. **Catalysis Letters**, v. 149, n. 8, 2158–2168, 2019a.

HU, X.; FAN, M.; ZHU, Y.; ZHU, Q.; SONG, Q. and DONG, Z. Biomass-derived phosphorus-doped carbon materials as efficient metal-free catalysts for selective aerobic oxidation of alcohols. **Green Chemistry**, v. 21, n. 19, 5274–5283, 2019b.

HU, X.; JIANG, S.; WU, L.; WANG, S. and LI, C.Z. One-pot conversion of biomass-derived xylose and furfural into levulinate esters via acid catalysis. **Chemical Communications**, v. 53, n. 20, 2938–2941, 2017.

HU, X.; WESTERHOF, R.J.; DONG, D.; WU, L. and LI, C.Z. Acid-catalyzed conversion of xylose in 20 solvents: insight into interactions of the solvents with xylose, furfural, and the acid catalyst. **ACS sustainable chemistry & engineering**, v. 2, n. 11, 2562–2575, 2014.

ISIKGOR, F.H. and BECER, C.R. Lignocellulosic biomass: a sustainable platform for the production of bio-based chemicals and polymers. **Polymer Chemistry**, v. 6, n. 25, 4497–4559, 2015.

JIANG, P.; LI, X.; GAO, W.; WANG, X.; TANG, Y.; LAN, K.; WANG, B. and LI, R. Highly selective hydrogenation of α, β-unsaturated carbonyl compounds over supported co nanoparticles. **Catalysis Communications**, v. 111, 6–9, 2018.

KAIPROMMARAT, S.; KONGPARAKUL, S.; REUBROYCHAROEN, P.; GUAN, G. and SAMART, C. Highly efficient sulfonic mcm-41 catalyst for furfural production: Furan-based biofuel agent. **Fuel**, v. 174, 189–196, 2016.

KARINEN, R.; VILONEN, K. and NIEMELÄ, M. Biorefining: heterogeneously catalyzed reactions of carbohydrates for the production of furfural and hydroxymethylfurfural. **ChemSusChem**, v. 4, n. 8, 1002–1016, 2011.

KIM, Y.C. and LEE, H.S. Selective synthesis of furfural from xylose with supercritical carbon dioxide and solid acid catalyst. **Journal of Industrial and Engineering Chemistry**, v. 7, n. 6, 424–429, 2001.

KOCH, S. and KINDLER, A. Production of furfural from xylose. World intellectual property organization wo 2015/087248 al, BASF, June 2015.

KOHLI, K.; PRAJAPATI, R. and SHARMA, B.K. Bio-based chemicals from renewable biomass for integrated biorefineries. **Energies**, v. 12, n. 2, 233, 2019.

KOZINSKI, A.A. Furfuryl alcohol production process. United states patent office n. 4,185,022, The Quaker Oats Company, January 1980.

KREISSL, H.T.; LI, M.M.; PENG, Y.K.; NAKAGAWA, K.; HOOPER, T.J.; HANNA, J.V.; SHEPHERD, A.; WU, T.S.; SOO, Y.L. and TSANG, S.E. Structural studies of bulk to nanosize niobium oxides with correlation to their acidity. **Journal of the American Chemical Society**, v. 139, n. 36, 12670–12680, 2017.

KREISSL, H.T.; NAKAGAWA, K.; PENG, Y.K.; KOITO, Y.; ZHENG, J. and TSANG, S.C.E. Niobium oxides: correlation of acidity with structure and catalytic performance in sucrose conversion to 5-hydroxymethylfurfural. **Journal of Catalysis**, v. 338, 329–339, 2016.

LAOHAPORNCHAIPHAN, J.; SMITH, C.B. and SMITH, S.M. One-step preparation of carbon-based solid acid catalyst from water hyacinth leaves for esterification of oleic acid and dehydration of xylose. **Chemistry–An Asian Journal**, v. 12, n. 24, 3178–3186, 2017.

LENSVELD, D.J.; MESU, J.G.; VAN DILLEN, A.J. and DE JONG, K.P. Synthesis and characterisation of mcm-41 supported nickel oxide catalysts. **Microporous and Mesoporous Materials**, v. 44, 401–407, 2001.

LI, F.; ZHU, W.; JIANG, S.; WANG, Y.; SONG, H. and LI, C. Catalytic transfer hydrogenation of furfural to furfuryl alcohol over fe3o4 modified ru/carbon nanotubes catalysts. **International Journal of Hydrogen Energy**, v. 45, n. 3, 1981–1990, 2020.

LI, L.; ROWBOTHAM, J.S.; CHRISTOPHER GREENWELL, H. and DYER, P.W. An introduction to pyrolysis and catalytic pyrolysis: Versatile techniques for biomass conversion. In **New and Future Developments in Catalysis: Catalytic Biomass Conversion**, v. 1, pp. 173–208. Elsevier, 2013.

LIU, B.; CHENG, L.; CURTISS, L. and GREELEY, J. Effects of van der waals density

functional corrections on trends in furfural adsorption and hydrogenation on close-packed transition metal surfaces. **Surface science**, v. 622, 51–59, 2014.

LIU, D.; ZEMLYANOV, D.; WU, T.; LOBO-LAPIDUS, R.J.; DUMESIC, J.A.; MILLER, J.T. and MARSHALL, C.L. Deactivation mechanistic studies of copper chromite catalyst for selective hydrogenation of 2-furfuraldehyde. **Journal of catalysis**, v. 299, 336–345, 2013.

LIU, L.; LOU, H. and CHEN, M. Selective hydrogenation of furfural to tetrahydrofurfuryl alcohol over ni/cnts and bimetallic cuni/cnts catalysts. **International Journal of Hydrogen Energy**, v. 41, n. 33, 14721–14731, 2016.

LIU, P.; QIU, W.; ZHANG, C.; TAN, Q.; ZHANG, C.; ZHANG, W.; SONG, Y.; WANG, H. and LI, C. Kinetics of furfural hydrogenation over bimetallic overlayer catalysts and the effect of oxygen vacancy concentration on product selectivity. **ChemCatChem**, v. 11, n. 14, 3296–3306, 2019.

LIU, X.; ZHOU, Y.; ZENG, D.; WANG, H.; QIAO, S.; ZHANG, L. and WANG, W. Catalytic acetalization and hydrogenation of furfural over the light-tunable phosphated tio2 catalyst. **ChemistrySelect**, v. 6, n. 31, 8074–8079, 2021.

LÓPEZ-ASENSIO, R.; CECILIA, J.; JIMÉNEZ-GÓMEZ, C.; GARCíA-SANCHO, C.; MORENO-TOST, R. and MAIRELES-TORRES, P. Selective production of furfuryl alcohol from furfural by catalytic transfer hydrogenation over commercial aluminas. **Applied Catalysis A: General**, v. 556, 1–9, 2018.

LOWELL, S.; SHIELDS, J.E.; THOMAS, M.A. and THOMMES, M. **Characterization of Porous Solids and Powders: Surface area, Pore Size and Density**, v. 16. Springer Science & Business Media, 2012.

MAKI-ARVELA, P.; SALMI, T.; HOLMBOM, B.; WILLFOR, S. and MURZIN, D.Y. Synthesis of sugars by hydrolysis of hemicelluloses-a review. **Chemical Reviews**, v. 111,

n. 9, 5638–5666, 2011.

MARCOTULLIO, Gianluca. **The Chemistry and Technology of Furfural Production in Modern Lignocellulose-Feedstock Biorefineries**. 2011. Thesis (Doctorate). Delft University of Technology, Delft, Netherlands.

MARISCAL, R.; MAIRELES-TORRES, P.; OJEDA, M.; SÁDABA, I. and GRANADOS, M.L. Energy environ. **Energy Environ. Sci**, v. 9, n. 4, 1144–1189, 2016.

MASTAGLI, P. Method for the catalytic hydrogenation of furfural. United states patent office n. 2,763,666, Etablissements Huillard, September 1956.

MAZZIERI, V.; COLOMA-PASCUAL, F.; ARCOYA, A.; LARGENTIERE, P. and FıGOLI, N. Xps, ftir and tpr characterization of ru/al2o3 catalysts. **Applied Surface Science**, v. 210, n. 3-4, 222–230, 2003.

MCCAIN JR, W.D. **Properties of Petroleum Fluids**. PennWell Corporation, 2017.

MEDOFF, M.; MASTERMAN, T.C.; KHAN, J. and COOPER, C. Conversión de biomasa. Oficina espanola de patentes y marcas n. 2 650 990, Xyleco Incorporated, January 2018.

MEJíA, C.H.; DEN OTTER, J.; WEBER, J. and DE JONG, K. Crystalline niobia with tailored porosity as support for cobalt catalysts for the fischer–tropsch synthesis. **Applied Catalysis A: General**, v. 548, 143–149, 2017.

MEJíA, C.H.; VOGT, C.; WECKHUYSEN, B. and DE JONG, K. Stable niobia-supported nickel catalysts for the hydrogenation of carbon monoxide to hydrocarbons. **Catalysis Today**, v. 343, 56–62, 2020.

MEKHEMER, G.; ABD-ALLAH, H. and MANSOUR, S. Surface characterization of

silica-supported cobalt oxide catalysts. **Colloids and Surfaces A: Physicochemical and Engineering Aspects**, v. 160, n. 3, 251–259, 1999.

MENDES, F.; PEREZ, C.; SOARES, R.; NORONHA, F. and SCHMAL, M. Ammonium complex of niobium as a precursor for the preparation of nb2o5/al2o3 catalysts. **Catalysis today**, v. 78, n. 1-4, 449–458, 2003.

MENDES, F.M.; NORONHA, F.B.; SOUZA, C.D.; DA SILVA, M.A.; GASPAR, A.B. and SCHMAL, M. The effect of pressure on promoted ru and re-co/niobia catalysts in the fischer-tropsch synthesis. In **Studies in surface science and catalysis**, v. 147, pp. 361–366. Elsevier, 2004.

MERAT, N.; GODAWA, C. and GASET, A. High selective production of tetrahydrofurfuryl alcohol: Catalytic hydrogenation of furfural and furfuryl alcohol. **Journal of Chemical Technology & Biotechnology**, v. 48, n. 2, 145–159, 1990.

MILE, B.; STIRLING, D.; ZAMMITT, M.; LOVELL, A. and WEBB, M. Tpr studies of the effects of preparation conditions on supported nickel catalysts. **Journal of molecular catalysis**, v. 62, n. 2, 179–198, 1990.

MILLÁN, G.G.; EL ASSAL, Z.; NIEMINEN, K.; HELLSTEN, S.; LLORCA, J. and SIXTA, H. Fast furfural formation from xylose using solid acid catalysts assisted by a microwave reactor. **Fuel processing technology**, v. 182, 56–67, 2018.

MISHRA, D.K.; DABBAWALA, A.A. and HWANG, J.S. Ruthenium nanoparticles supported on zeolite y as an efficient catalyst for selective hydrogenation of xylose to xylitol. **Journal of Molecular Catalysis A: Chemical**, v. 376, 63–70, 2013.

MISHRA, R.K.; KUMAR, V.B.; VICTOR, A.; PULIDINDI, I.N. and GEDANKEN, A. Selective production of furfural from the dehydration of xylose using zn doped cuo catalyst. **Ultrasonics sonochemistry**, v. 56, 55–62, 2019.

MÖLLER, M. and SCHRÖDER, U. Hydrothermal production of furfural from xylose and xylan as model compounds for hemicelluloses. **Rsc Advances**, v. 3, n. 44, 22253–22260, 2013.

MOREAU, C.; BELGACEM, M.N. and GANDINI, A. Recent catalytic advances in the chemistry of substituted furans from carbohydrates and in the ensuing polymers. **Topics in Catalysis**, v. 27, n. 1-4, 11–30, 2004.

MORGAN, D.J. Resolving ruthenium: Xps studies of common ruthenium materials. **Surface and Interface Analysis**, v. 47, n. 11, 1072–1079, 2015.

MOURA, L. V. **Production of Furfural from Xylose: Determination of Kinetic Parameters and Simulation of a Reactive Stripping Process**. 2019. Dissertation (Mastering). Universidade Estadual de Campinas, Campinas.

MUSCI, J.J.; MERLO, A.B. and CASELLA, M.L. Aqueous phase hydrogenation of furfural using carbon-supported ru and rusn catalysts. **Catalysis Today**, v. 296, 43–50, 2017.

NAGAI, M.; KOIZUMI, K. and OMI, S. Nh3-tpd and xps studies of ru/al2o3 catalyst and hds activity. **Catalysis today**, v. 35, n. 4, 393–405, 1997.

NAKAGAWA, Y. and TOMISHIGE, K. Total hydrogenation of furan derivatives over silica-supported ni–pd alloy catalyst. **Catalysis Communications**, v. 12, n. 3, 154–156, 2010.

NAKAJIMA, K.; BABA, Y.; NOMA, R.; KITANO, M.; N. KONDO, J.; HAYASHI, S. and HARA, M. Nb2o5· nh2o as a heterogeneous catalyst with water-tolerant lewis acid sites. **Journal of the American Chemical Society**, v. 133, n. 12, 4224–4227, 2011.

NAKAJIMA, K.; FUKUI, T.; KATO, H.; KITANO, M.; KONDO, J.N.; HAYASHI, S.

and HARA, M. Structure and acid catalysis of mesoporous nb2o5· n h2o. **Chemistry of Materials**, v. 22, n. 11, 3332–3339, 2010.

NASCIMENTO, I. L. **Hidrogenação do furfural a álcool furfurílico em fase líquida: efeitos das condições reacionais e do método de redução sobre o desempenho de catalisadores de Cu, Ru e Pd suportados em alumina**. 2018. Dissertation (Mastering). Universidade Estadual de Campinas, Campinas.

NEELI, C.K.P.; CHUNG, Y.M. and AHN, W.S. Catalytic transfer hydrogenation of furfural to furfuryl alcohol by using ultrasmall rh nanoparticles embedded on diamine-functionalized kit-6. **ChemCatChem**, v. 9, n. 24, 4570–4579, 2017.

NGUYEN-HUY, C.; LEE, J.; SEO, J.H.; YANG, E.; LEE, J.; CHOI, K.; LEE, H.; KIM, J.H.; LEE, M.S.; JOO, S.H. *et al.* Structure-dependent catalytic properties of mesoporous cobalt oxides in furfural hydrogenation. **Applied Catalysis A: General**, v. 583, 117125, 2019.

NIMLOS, M.R.; QIAN, X.; DAVIS, M.; HIMMEL, M.E. and JOHNSON, D.K. Energetics of xylose decomposition as determined using quantum mechanics modeling. **The Journal of Physical Chemistry A**, v. 110, n. 42, 11824–11838, 2006.

NORONHA, F.B.; PEREZ, C.A.; SCHMAL, M. and FRETY, R. Determination of cobalt species in niobia supported catalysts. **Physical Chemistry Chemical Physics**, v. 1, n. 11, 2861–2867, 1999.

NOWAK, I. and ZIOLEK, M. Niobium compounds: preparation, characterization, and application in heterogeneous catalysis. **Chemical Reviews**, v. 99, n. 12, 3603–3624, 1999.

O′DRISCOLL, Á.; CURTIN, T.; HERNANDEZ, W.Y.; VAN DER VOORT, P. and LEAHY, J.J. Hydrogenation of furfural with a pt–sn catalyst: The suitability to sustainable industrial application. **Organic Process Research & Development**, v. 20,

n. 11, 1917–1929, 2016.

O′DRISCOLL, Á.; LEAHY, J. and CURTIN, T. The influence of metal selection on catalyst activity for the liquid phase hydrogenation of furfural to furfuryl alcohol. **Catalysis Today**, v. 279, 194–201, 2017.

OKAZAKI, S.; KURIMATA, M.; IIZUKA, T. and TANABE, K. The effect of phosphoric acid treatment on the catalytic property of niobic acid. **Bulletin of the Chemical Society of Japan**, v. 60, n. 1, 37–41, 1987.

OKAZAKI, S. and KUROSAKI, A. Acidic properties and catalytic activities of niobic acid treated with phosphoric acid. **Catalysis Today**, v. 8, n. 1, 113–122, 1990.

OKAZAKI, S. and WADA, N. Surface properties and catalytic activities of amorphous niobium phosphate and a comparison with those of h3po4-treated niobium oxide. **Catalysis today**, v. 16, n. 3-4, 349–359, 1993.

OLIVEIRA, H.A.; FRANCESCHINI, D.F. and PASSOS, F.B. Cobalt catalyst characterization for methane decomposition and carbon nanotube growth. **Journal of the Brazilian Chemical Society**, v. 25, 2339–2349, 2014.

ORDOMSKY, V.V.; SCHOUTEN, J.; VAN DER SCHAAF, J. and NIJHUIS, T. Biphasic single-reactor process for dehydration of xylose and hydrogenation of produced furfural. **Applied Catalysis A: General**, v. 451, 6–13, 2013a.

ORDOMSKY, V.V.; SCHOUTEN, J.; VAN DER SCHAAF, J. and NIJHUIS, T. Multilevel rotating foam biphasic reactor for combination of processes in biomass transformation. **Chemical Engineering Journal**, v. 231, 12–17, 2013b.

PANAGIOTOPOULOU, P.; MARTIN, N. and VLACHOS, D.G. Effect of hydrogen donor on liquid phase catalytic transfer hydrogenation of furfural over a ru/ruo2/c catalyst.

Journal of Molecular Catalysis A: Chemical, v. 392, 223–228, 2014.

PARDO CUERVO, O.H.; ROMANELLI, G.P.; CUBILLOS, J.A.; ROJAS, H.A. and MARTíNEZ, J.J. Selective catalytic dehydration of xylose to furfural and fructose and glucose to 5-hydroximethylfurfural (hmf) using preyssler heteropolyacid. **ChemistrySelect**, v. 5, n. 14, 4186–4193, 2020.

PARIKH, J.; SRIVASTAVA, S. and JADEJA, G.C. Selective hydrogenation of furfural to tetrahydrofurfuryl alcohol using supported nickel–cobalt catalysts. **Industrial & Engineering Chemistry Research**, v. 58, n. 35, 16138–16152, 2019.

PÂRVULESCU, V.; RUWET, M.; GRANGE, P. and PÂRVULESCU, V. Preparation, characterisation and catalytic behaviour of cobalt–niobia catalysts. **Journal of Molecular Catalysis A: Chemical**, v. 135, n. 1, 75–88, 1998.

PAULINO, P.N.; PEREZ, R.F.; FIGUEIREDO, N.G. and FRAGA, M.A. Tandem dehydration–transfer hydrogenation reactions of xylose to furfuryl alcohol over zeolite catalysts. **Green Chemistry**, v. 19, n. 16, 3759–3763, 2017.

PAWAR, H.S. Sulfonic acid anchored heterogeneous acid-catalyst dicat-3 for conversion of xylose into furfural in biphasic solvent system. **ChemistrySelect**, v. 5, n. 2, 916–923, 2020.

PENDYALA, V.R.R.; GNANAMANI, M.K.; JACOBS, G.; MA, W.; SHAFER, W.D. and DAVIS, B.H. Fischer–tropsch synthesis: effect of ammonia impurities in syngas feed over a cobalt/alumina catalyst. **Applied Catalysis A: General**, v. 468, 38–43, 2013.

PEREIRA, P.; VOORWALD, H.; CIOFFI, M.; DA SILVA, M.; REGO, A.; FERRARIA, A. and DE PINHO, M.N. Sugarcane bagasse cellulose fibres and their hydrous niobium phosphate composites: synthesis and characterization by xps, xrd and sem. **Cellulose**, v. 21, n. 1, 641–652, 2014.

PEREZ, R.F.; ALBUQUERQUE, E.M.; BORGES, L.E.; HARDACRE, C. and FRAGA, M.A. Aqueous-phase tandem catalytic conversion of xylose to furfuryl alcohol over [al]-sba-15 molecular sieves. **Catalysis Science & Technology**, v. 9, n. 19, 5350–5358, 2019.

PEREZ, R.F.; CANHACI, S.J.; BORGES, L.E. and FRAGA, M.A. One-step conversion of xylose to furfuryl alcohol on sulfated zirconia-supported pt catalyst—balance between acid and metal sites. **Catalysis Today**, v. 289, 273–279, 2017.

PEREZ, R.F. and FRAGA, M.A. Hemicellulose-derived chemicals: one-step production of furfuryl alcohol from xylose. **Green Chemistry**, v. 16, n. 8, 3942–3950, 2014.

PETERS JR, F.N. Method for the reduction of furfural and furan derivatives. United states patent office n. 2,082,025, The Quaker Oats Company, June 1937.

PHOLJAROEN, B.; LI, N.; WANG, Z.; WANG, A. and ZHANG, T. Dehydration of xylose to furfural over niobium phosphate catalyst in biphasic solvent system. **Journal of energy chemistry**, v. 22, n. 6, 826–832, 2013.

PINO, N.; SITTHISA, S.; TAN, Q.; SOUZA, T.; LÓPEZ, D. and RESASCO, D.E. Structure, activity, and selectivity of bimetallic pd-fe/sio2 and pd-fe/γ-al2o3 catalysts for the conversion of furfural. **Journal of Catalysis**, v. 350, 30–40, 2017.

PISKUN, A.; DE HAAN, J.; WILBERS, E.; VAN DE BOVENKAMP, H.; TANG, Z. and HEERES, H. Hydrogenation of levulinic acid to γ-valerolactone in water using millimeter sized supported ru catalysts in a packed bed reactor. **Acs Sustainable Chemistry & Engineering**, v. 4, n. 6, 2939–2950, 2016.

RAMIREZ-BARRIA, C.; ISAACS, M.; WILSON, K.; GUERRERO-RUIZ, A. and RODRíGUEZ-RAMOS, I. Optimization of ruthenium based catalysts for the aqueous phase hydrogenation of furfural to furfuryl alcohol. **Applied Catalysis A: General**, v. 563, 177–184, 2018.

RASMUSSEN, H. and SøRENSEN, H. As meyer formation of degradation compounds from lignocellulosic biomass in the biorefinery: sugar reaction mechanisms carbohydr. **Res**, v. 385, 45–57, 2014.

RINALDI, R.; WOODWARD, R.T.; FERRINI, P. and RIVERA, H.J. Lignin-first biorefining of lignocellulose: The impact of process severity on the uniformity of lignin oil composition. **Journal of the Brazilian Chemical Society**, v. 30, n. 3, 479–491, 2019.

ROCHA, A.S.; COSTA, G.C.; DE ARAUJO, L.R.R.; MISAEL, W.A.; OLIVEIRA, R.R. and ROCHA, A.B. Insights into the phosphate species on niobia treated with h3po4. **Catalysis Letters**, v. 150, n. 5, 1496–1504, 2020.

ROTOLE, J.A. and SHERWOOD, P.M. Aluminum phosphate by xps. **Surface Science Spectra**, v. 5, n. 1, 60–66, 1998.

SALNIKOVA, K.E.; MATVEEVA, V.G.; LARICHEV, Y.V.; BYKOV, A.V.; DEMIDENKO, G.N.; SHKILEVA, I.P. and SULMAN, M.G. The liquid phase catalytic hydrogenation of furfural to furfuryl alcohol. **Catalysis Today**, v. 329, 142–148, 2019.

SANKAR, G.; VASUDEVAN, S. and RAO, C. Strong metal-support interaction in nickel/niobium pentoxide and nickel/titania catalysts. **The Journal of Physical Chemistry**, v. 92, n. 7, 1878–1882, 1988.

SHARMA, R.V.; DAS, U.; SAMMYNAIKEN, R. and DALAI, A.K. Liquid phase chemoselective catalytic hydrogenation of furfural to furfuryl alcohol. **Applied Catalysis A: General**, v. 454, 127–136, 2013.

SIMON, D.; PERRIN, C. and BAILLIF, P. Electron spectrometry study (esca) of niobium and its oxides. application to the oxidation at high temperature and low oxygen pressure. **CR Hebd. Acad. Sci., Ser. C**, v. 283, n. 6, 241–244, 1976.

SOARES, R.; FRYDMAN, A. and SCHMAL, M. Effect of preparation method on 5% co/nb2o5 in fischer-tropsch syntesis (fts). **Catalysis today**, v. 16, n. 3-4, 361–370, 1993.

SONG, D. and LI, J. Effect of catalyst pore size on the catalytic performance of silica supported cobalt fischer–tropsch catalysts. **Journal of Molecular Catalysis A: Chemical**, v. 247, n. 1-2, 206–212, 2006.

SUPPINO, R. S. **Hidrogenação de Compostos Aromáticos em Fase Líquida com Catalisadores à Base de Metais do Grupo VIII Suportados em Alumina via Impregnação Úmida**. 2014. Thesis (Doctorate). Universidade Estadual de Campinas, Campinas.

SWADESH, S. Catlytic production of furfuryl alcohol and catalyst therefor. United states patent office n. 2,754,304, The Quaker Oats Company, July 1956.

SWANSON, H. and TATGE, E. 01-087-0713 ic-dd pdf-2 2003: From icsd using powd-12.[]. **Natl. Bur, Stand.(US), Circ**, v. 539, n. 359, I1, 1953.

TAN, B.J.; KLABUNDE, K.J. and SHERWOOD, P.M. Xps studies of solvated metal atom dispersed (smad) catalysts. evidence for layered cobalt-manganese particles on alumina and silica. **Journal of the American Chemical Society**, v. 113, n. 3, 855–861, 1991.

TANG, Z.C.; YU, D.H.; SUN, P.; LI, H. and HUANG, H. Phosphoric acid modified nb 2 o 5: a selective and reusable catalyst for dehydration of sorbitol to isosorbide. **Bulletin of the Korean Chemical Society**, v. 31, n. 12, 3679–3683, 2010.

TERMVIDCHAKORN, C.; ITTHIBENCHAPONG, V.; SONGTAWEE, S.; CHAMNANKID, B.; NAMUANGRUK, S.; FAUNGNAWAKIJ, K.; CHARINPANITKUL, T.; KHUNCHIT, R.; HANSUPALUK, N.; SANO, N. *et al.* Dehydration of d-xylose to furfural using acid-functionalized mwcnts catalysts. **Advances in Natural Sciences: Nanoscience and Nanotechnology**, v. 8, n. 3, 035006, 2017.

THOMMES, M.; KANEKO, K.; NEIMARK, A.V.; OLIVIER, J.P.; RODRIGUEZ-REINOSO, F.; ROUQUEROL, J. and SING, K.S. Physisorption of gases, with special reference to the evaluation of surface area and pore size distribution (iupac technical report). **Pure and applied chemistry**, v. 87, n. 9-10, 1051–1069, 2015.

TRAN, S.B.T.; CHOI, H.; OH, S. and PARK, J.Y. Defective nb2o5-supported pt catalysts for co oxidation: Promoting catalytic activity via oxygen vacancy engineering. **Journal of catalysis**, v. 375, 124–134, 2019.

USSIRI, D.A. and LAL, R. Miscanthus agronomy and bioenergy feedstock potential on minesoils. **Biofuels**, v. 5, n. 6, 741–770, 2014.

VAN ZANDVOORT, I.; WANG, Y.; RASRENDRA, C.B.; VAN ECK, E.R.; BRUIJNINCX, P.C.; HEERES, H.J. and WECKHUYSEN, B.M. Formation, molecular structure, and morphology of humins in biomass conversion: influence of feedstock and processing conditions. **ChemSusChem**, v. 6, n. 9, 1745–1758, 2013.

VEMIC, M. **Leaching and recovery of Mo, Ni and Co from metals recycling plants mineral sludges**. 2015. Thesis (Doctorate). University Paris-Est, Paris, France.

VIEIRA, J.L.; ALMEIDA-TRAPP, M.; MITHÖFER, A.; PLASS, W. and GALLO, J.M.R. Rationalizing the conversion of glucose and xylose catalyzed by a combination of lewis and brønsted acids. **Catalysis Today**, v. 344, 92–101, 2020.

WANG, Y.; LU, Y.; CAO, Q. and FANG, W. A magnetic coru-coox nanocomposite efficiently hydrogenates furfural to furfuryl alcohol at ambient h2 pressure in water. **Chemical Communications**, v. 56, n. 26, 3765–3768, 2020.

WANG, Y.; PRINSEN, P.; TRIANTAFYLLIDIS, K.S.; KARAKOULIA, S.A.; YEPEZ, A.; LEN, C. and LUQUE, R. Batch versus continuous flow performance of supported mono-and bimetallic nickel catalysts for catalytic transfer hydrogenation of furfural in isopropanol. **ChemCatChem**, v. 10, n. 16, 3459–3468, 2018.

WANG, Y.; ZHAO, D.; RODRíGUEZ-PADRÓN, D. and LEN, C. Recent advances in catalytic hydrogenation of furfural. **Catalysts**, v. 9, n. 10, 796, 2019.

WEINGARTEN, R.; TOMPSETT, G.A.; CONNER JR, W.C. and HUBER, G.W. Design of solid acid catalysts for aqueous-phase dehydration of carbohydrates: The role of lewis and brønsted acid sites. **Journal of Catalysis**, v. 279, n. 1, 174–182, 2011.

WENG, Y.; QIU, S.; MA, L.; LIU, Q.; DING, M.; ZHANG, Q.; ZHANG, Q. and WANG, T. Jet-fuel range hydrocarbons from biomass-derived sorbitol over ni-hzsm-5/sba-15 catalyst. **Catalysts**, v. 5, n. 4, 2147–2160, 2015.

WETTSTEIN, S.G.; ALONSO, D.M.; GÜRBÜZ, E.I. and DUMESIC, J.A. A roadmap for conversion of lignocellulosic biomass to chemicals and fuels. **Current Opinion in Chemical Engineering**, v. 1, n. 3, 218–224, 2012.

WOJCIESZAK, R.; JASIK, A.; MONTEVERDI, S.; ZIOLEK, M. and BETTAHAR, M. Nickel niobia interaction in non-classical ni/nb2o5 catalysts. **Journal of Molecular Catalysis A: Chemical**, v. 256, n. 1-2, 225–233, 2006.

WU, J.; GAO, G.; LI, J.; SUN, P.; LONG, X. and LI, F. Efficient and versatile cuni alloy nanocatalysts for the highly selective hydrogenation of furfural. **Applied Catalysis B: Environmental**, v. 203, 227–236, 2017.

WU, Z.L.; WANG, J.; WANG, S.; ZHANG, Y.X.; BAI, G.Y.; RICARDEZ-SANDOVAL, L.; WANG, G.C. and ZHAO, B. Controllable chemoselective hydrogenation of furfural by pdag/c bimetallic catalysts under ambient operating conditions: an interesting ag switch. **Green Chemistry**, v. 22, n. 4, 1432–1442, 2020.

XIANG, W.; HAN, X.; ASTORSDOTTER, J. and FARRAUTO, R. Catalysts promoted with niobium oxide for air pollution abatement. **catalysts**, v. 7, n. 5, 144, 2017.

XU, L.; NIE, R.; XU, H.; CHEN, X.; LI, Y. and LU, X. One-pot tandem dehydration–hydrogenation of xylose with formic acid over co catalysts. **Industrial & Engineering Chemistry Research**, v. 59, n. 7, 2754–2760, 2020.

YAN, K.; WU, G.; LAFLEUR, T. and JARVIS, C. Production, properties and catalytic hydrogenation of furfural to fuel additives and value-added chemicals. **Renewable and sustainable energy reviews**, v. 38, 663–676, 2014.

YANG, J.; MA, J.; YUAN, Q.; ZHANG, P. and GUAN, Y. Selective hydrogenation of furfural on ru/al-mil-53: a comparative study on the effect of aromatic and aliphatic organic linkers. **RSC advances**, v. 6, n. 95, 92299–92304, 2016.

YOU, S.J.; KIM, Y.T. and PARK, E.D. Liquid-phase dehydration of d-xylose over silica–alumina catalysts with different alumina contents. **Reaction Kinetics, Mechanisms and Catalysis**, v. 111, n. 2, 521–534, 2014.

YOU, S.J.; PARK, E.D. and PARK, M.J. Dehydration of d-xylose over sio 2-al 2 o 3 catalyst: Perspective on the pathways for condensed products. **Korean Journal of Chemical Engineering**, v. 33, n. 3, 806–811, 2016.

YU, W.; XIONG, K.; JI, N.; POROSOFF, M.D. and CHEN, J.G. Theoretical and experimental studies of the adsorption geometry and reaction pathways of furfural over feni bimetallic model surfaces and supported catalysts. **Journal of catalysis**, v. 317, 253–262, 2014.

ZEITSCH, K.J. **The chemistry and technology of furfural and its many by-products**. Elsevier, 2000.

ZHANG, T.; LI, W.; XU, Z.; LIU, Q.; MA, Q.; JAMEEL, H.; CHANG, H.M. and MA, L. Catalytic conversion of xylose and corn stalk into furfural over carbon solid acid catalyst in γ-valerolactone. **Bioresource technology**, v. 209, 108–114, 2016.

ZHANG, Z.; SONG, J.; JIANG, Z.; MENG, Q.; ZHANG, P. and HAN, B. Direct synthesis of ultrasmall ruthenium nanoparticles on porous supports using natural sources for highly efficient and selective furfural hydrogenation. **ChemCatChem**, v. 9, n. 13, 2448–2452, 2017.

ZHOU, P. and ZHANG, Z. One-pot catalytic conversion of carbohydrates into furfural and 5-hydroxymethylfurfural. **Catalysis Science & Technology**, v. 6, n. 11, 3694–3712, 2016.

ZHU, L.W.; WANG, J.G.; ZHAO, P.P.; FENG, S.; SUN, X.Y.; WANG, L.H.; CUI, H.Y. and YI, W.M. Preparation of the nb-p/sba-15 catalyst and its performance in the dehydration of fructose to 5-hydroxymethylfurfural. **Journal of Fuel Chemistry and Technology**, v. 45, n. 6, 651–659, 2017a.

ZHU, Y.; LI, W.; LU, Y.; ZHANG, T.; JAMEEL, H.; CHANG, H.M. and MA, L. Production of furfural from xylose and corn stover catalyzed by a novel porous carbon solid acid in γ-valerolactone. **RSC advances**, v. 7, n. 48, 29916–29924, 2017b.

Chapter 7

Appendix

Figure 7.1: SEM analysis for CoNB10 catalyst.

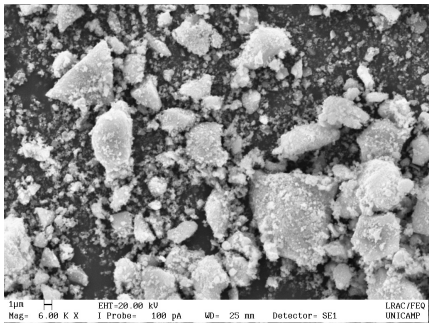

Figure 7.2: SEM analysis for NiNB10 catalyst.

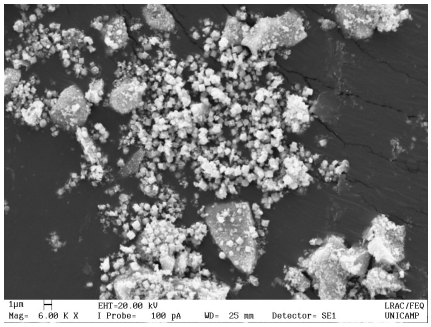

Figure 7.3: SEM analysis for RuNB05 catalyst.

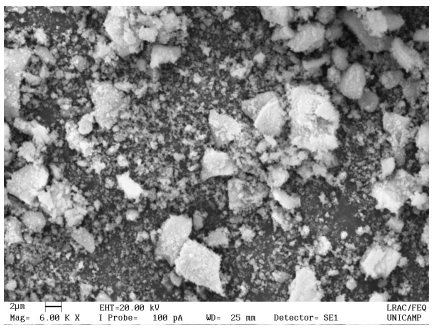

Figure 7.4: SEM analysis for CoNBAc10 catalyst.

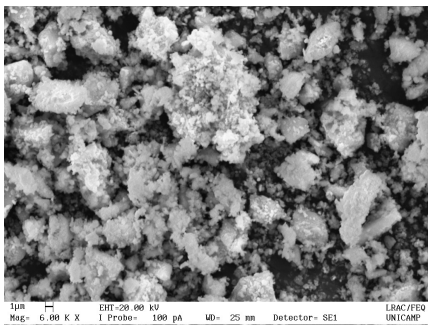

Figure 7.5: SEM analysis for NiNBAc10 catalyst.

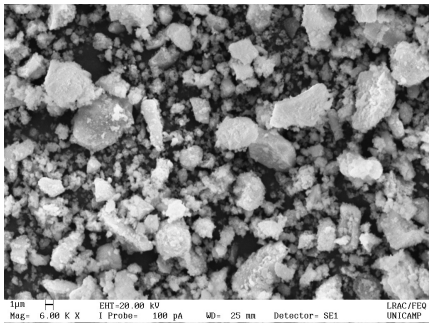

Figure 7.6: SEM analysis for RuNBAc05 catalyst.

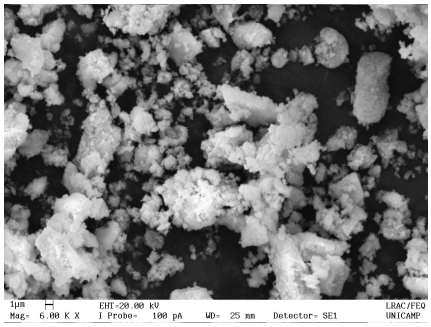

Figure 7.7: SEM - NB400 after reaction.

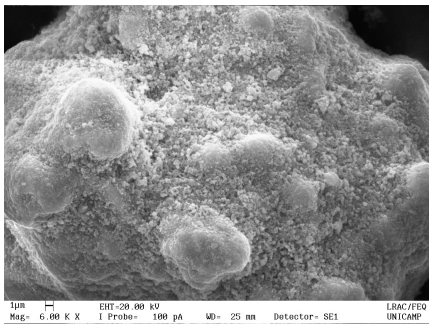

Figure 7.8: SEM - NBAc400 after reaction.

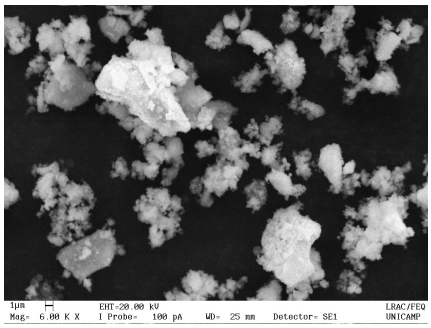

Figure 7.9: SEM - CoNB10 after reaction.

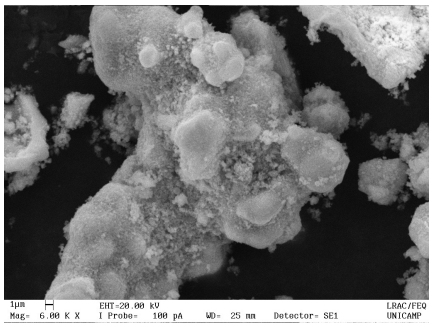

Figure 7.10: SEM - CoNBAc10 after reaction.

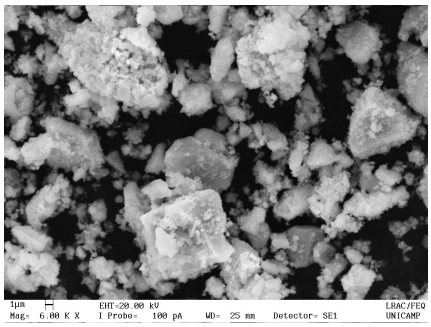

Figure 7.11: SEM - NiNB10 after reaction.

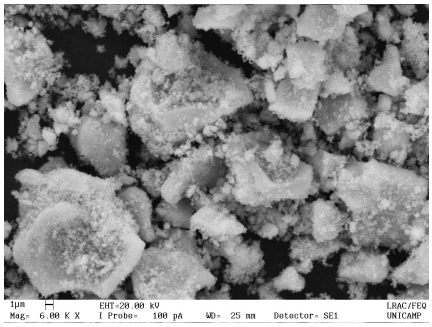

Figure 7.12: SEM - NiNBAc10 after reaction.

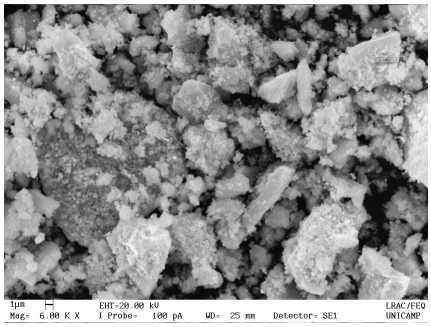

Figure 7.13: SEM - RuNB05 after reaction.

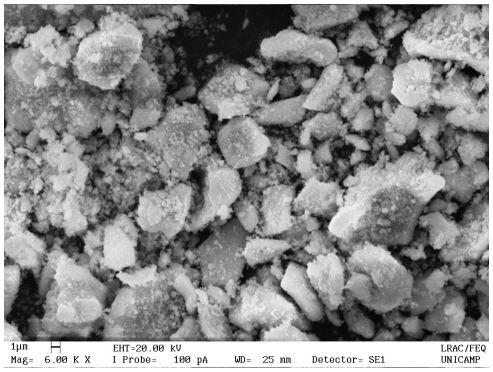

Figure 7.14: SEM - RuNBAc05 after reaction.

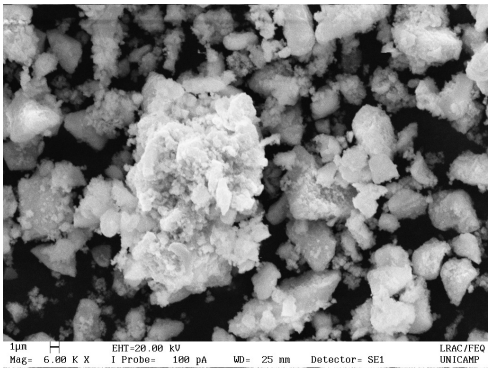

Figure 7.15: HPLC pattern analysis - XYL.

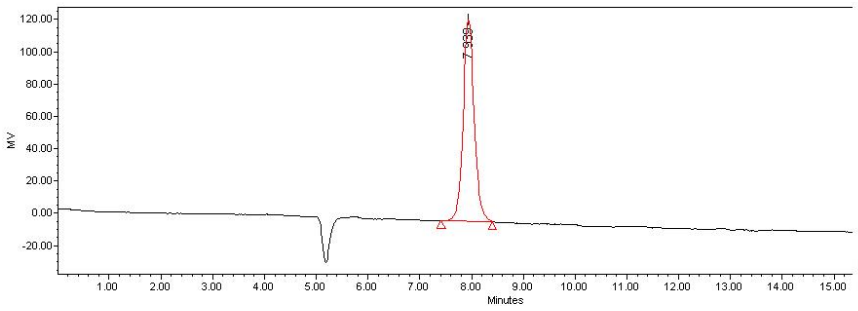

Figure 7.16: HPLC pattern analysis - XOL.

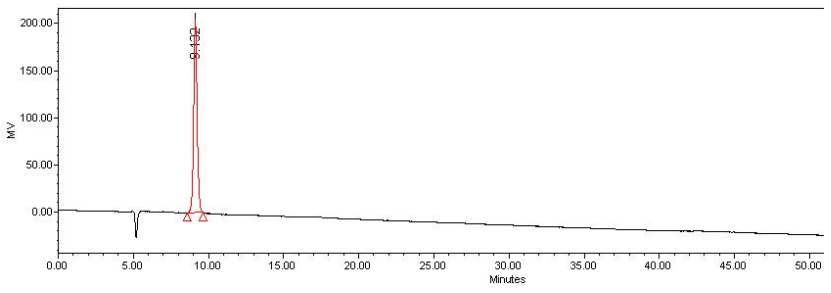

Figure 7.17: HPLC pattern analysis - FA.

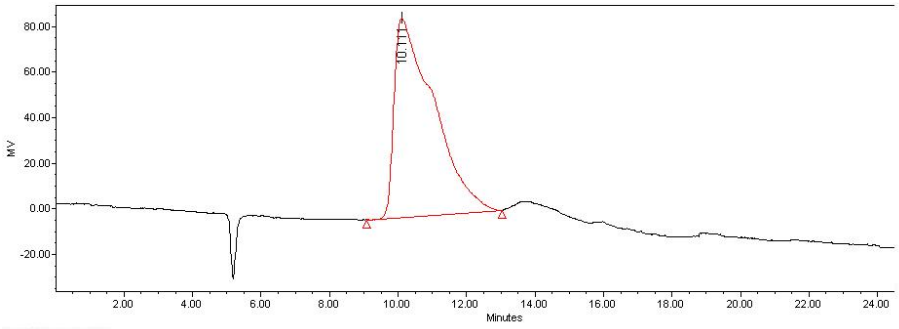

Figure 7.18: HPLC pattern analysis - THFA.

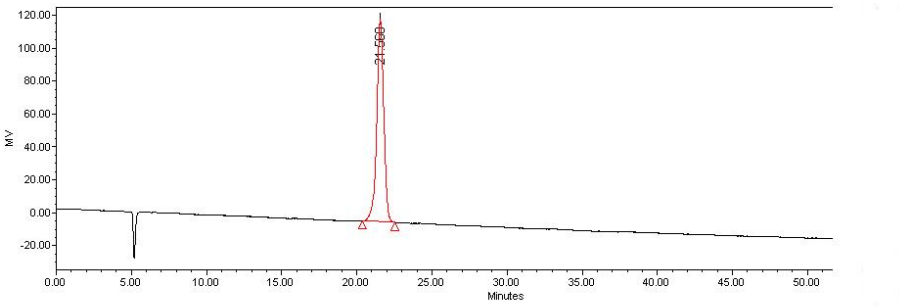

Figure 7.19: HPLC pattern analysis - LA.

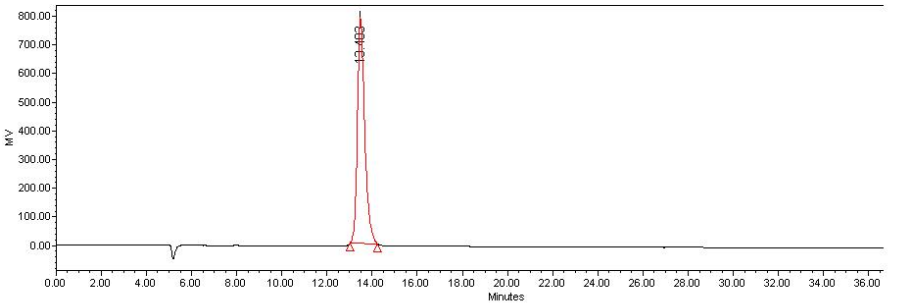

Figure 7.20: HPLC pattern analysis - GVL.

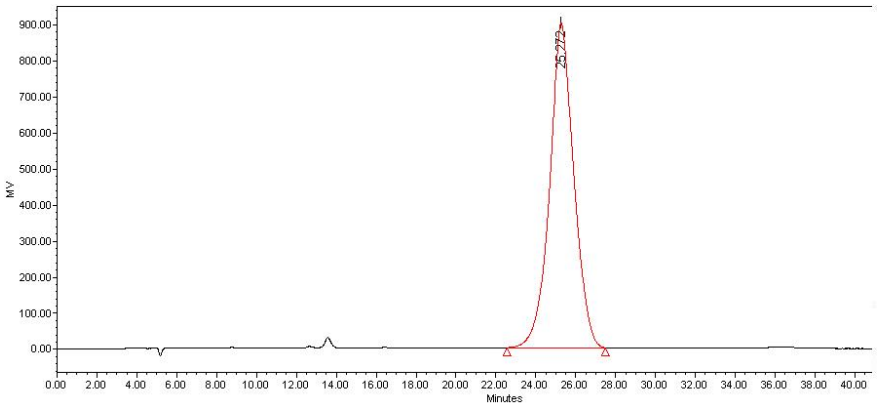

Figure 7.21: HPLC pattern analysis - CPO.

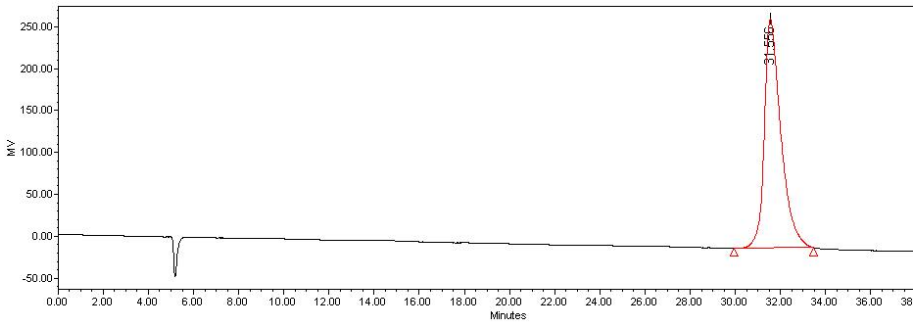

Figure 7.22: HPLC pattern analysis - FUR.